8-2017

Novel Half-Metallic and Spin-Gapless Heusler Compounds

Yunlong Jin
University of Nebraska-Lincoln, yjin4@unl.edu

NOVEL HALF-METALLIC AND SPIN-GAPLESS HEUSLER COMPOUNDS

by

Yunlong Jin

A DISSERTATION

Presented to the Faculty of

The Graduate College of the University of Nebraska

In Partial Fulfillment of Requirements

For the Degree of Doctor of Philosophy

Major: Physics and Astronomy

Under the Supervision of Professor David J. Sellmyer

Lincoln, Nebraska

August, 2017

NOVEL HALF-METALLIC AND SPIN-GAPLESS HEUSLER COMPOUNDS

Yunlong Jin, Ph.D.

University of Nebraska, 2017

Adviser: David J. Sellmyer

This thesis is devoted to experimental studies of Heusler compounds CoFeCrAl, CoFeCrX (X = Si, Ge) and Mn_2PtSn. These Heusler alloys present an interesting class of ferromagnetic materials for spintronic applications since they are predicted to be spin gapless semiconductors and have half-metallic properties with 100 % spin polarization at the Fermi level. In this thesis, the structural, magnetic, spin-polarization and electron- transport properties of the fabricated alloys were studied. CoFeCrAl thin films deposited on MgO exhibit nearly perfect epitaxy and a high degree of $L2_1$ Heusler order. All considered types of chemical disorder destroy the spin-gapless semiconductivity of Y-ordered CoFeCrAl, but B2 disorder and A2-type Cr-Fe disorder conserve the half-metallicity of the alloy. The transport spin polarization at the Fermi level is higher than 68%. Epitaxial thin films of inverse tetragonal Mn_2PtSn were synthesized and show lattice constants a = 0.449 nm, and b = 0.615 nm. Magnetization measurements revealed an in-plane anisotropy energy of 10 Merg/cm^3. CoFeCrSi and CoFeCrGe Heusler alloys crystallize in cubic $L2_1$ structures with a small site disorder. The CoFeCrSi alloy exhibited a high Curie temperature (T_C = 790 K). Cubic CoFeCrGe decomposed into other compounds near 402 ^{o}C (675 K). A new tetragonal $Co_{53.4}Fe_{30.4}Cr_{8.6}Ge_{7.6}$ phase with lattice parameters a = 0.760 nm, c = 0.284 nm was studied with a series of tilted electron- diffraction measurements in this work. The (Co, Fe)-rich phase was found to embedded in the matrix of a Cr-rich phase. The results show promise for the implementation of CoFeCrX (X = Al, Si, Ge) and Mn_2PtSn in future spintronics devices.

DEDICATION

To my father, Yucai Jin and my mother, Xiuling Wang.

To my wife, Yewei Zhang, for support and understanding.

ACKNOWLEDGMENTS

I have been in Lincoln since August 2012 and the time goes very fast. I am very grateful to many people who have helped me during my Ph.D. study.

First and foremost, I want to sincerely thank my advisor, Professor David J. Sellmyer, for his support, patience, and encouragement during my graduate studies. It is not often that one finds an advisor and colleague that always finds the time for listening to the little problems and roadblocks that unavoidably crop up in the course of performing research. His advice was essential to the completion of my dissertation and projects. He has taught me innumerable lessons and insights on the workings of academic research in general. I learned a lot in every discussion with him.

My thanks also go to the members of my major committee, Professors Ralph Skomski, Jeffrey Shield and Sy-Hwang Liou for help and support during my graduate studies. I got a lot of help from Professor Skomski on my projects and discussions with him during weekly group meetings. Discussions with Professor Liou were always very easy because he is very kind and knowledgeable. I also appreciated that he shared his coffee beans and machine, which served my daily coffee. Professor Jeffrey Shield is appreciated for his positive attitude and incisive thought.

The friendship of Tao Li, Yi Yang, Jie Yang, Xiaolu Yin is much appreciated and has led to many interesting and good-spirited discussions. I also appreciated the friendship of Randi Meyer, Prof. Kees Uiterwaal, Xiaohui Liu, Xuegang Chen, Jingfeng Song, Zhiyong Xiao, Kishan Sinha, Yiyun Zhang, Christopher White II, Niran Tamrakar, Beth Cordell, Joyce Ross, Mark Meyer, Li Zhang, Meiyu Wang, Yifan Li, and so many friends in the International Students Fellowship. Their help made my life here very exciting. Dr. Rulong Zhou helped me to settle down and rent an apartment. The first two weeks in Lincoln I had lunch and dinner at his home every day.

I am also grateful to my colleagues Parashu Kharel. Dr. Kharel brought me into the Heusler field and taught me a lot of knowledge about this field. By watching his altitude to science and working with him, I learned how to do research. Pavel Lukashev, Shah Valloppilly, Xingzhong

Li, Bhaskar Das, Balamurugan Balasubramanian, Yi Liu, Lanping Yue, Steve Michalski, Jiong Hua, Wenyong Zhang, Tom George, Zhiguang Sun, Renu Choudhary, Rohit Pathaka, Arti Kashyap, Gejian Zhao and Tingyong Chen for helping considerably with realizing my project and contents of dissertation.

Last, but not least, I would like to thank my wife Yewei Zhang for her understanding and love during the past few years. Her support and encouragement were in the end what made this dissertation possible. My parents, Yucai and Xiuling, receive my deepest gratitude and love for their dedication and the many years of support.

TABLE OF CONTENTS

List of Figures

List of tables

Chapter 1. Introduction

This chapter introduces basic concepts relevant to Heusler compounds such as structure, chemical ordering, half-metallic (HM) and spin-gapless semiconductor (SGS) band gap, spintronics and potential device application. Section 1.1 describes basics of magnetic Heusler compounds. Section 1.2-1.3 introduce different types of Heusler compounds, chemical disordering, and magnetic properties. Section 1.4-1.5 discusses the basic concepts of half-metallic Heusler and spin-gapless semiconductors. Section 1.6-1.8 cover the transport properties such as temperature dependence of longitudinal resistivity, ordinary and anomalous Hall-effects, and field dependence of magnetoresistivity. Section 1.9 introduce the concept of spin polarization and during section 1.10, the concept of spintronics and potential device application of magnetic Heusler films are discussed.

1.1 Basics of Heusler Compounds.

Heusler compounds were discovered in 1903 by Friedrich Heusler.[1] The first Heusler compounds studied were CuMnSb, Cu_2MnAl, and Cu_2MnSn.[1, 2] At that time, the original attention to Heusler compounds was due to three 'nonmagnetic' elements (Cu, Mn, Al) yielding a ferromagnetic compound. Mn is known to be an antiferromagnet now, but antiferromagnetism was unknown until Néel's work in the 1940s. Today's renewed interest is largely linked to spin electronics. Up to now, Heusler compounds have been found more than 1000 members as an outstanding class of materials exhibiting various property types such as half-metals, spin-gapless semiconducting, high-temperature ferri- and ferromagnets, antiferromagnets, multiferroics, shape-memory compounds, Weyl or Dirac semimetals and tunable topological insulators.[3] These properties have potential

application in the fields of spintronics, energy technologies, and magneto-caloric applications. For example, the Co-based Heusler compound, Co_2MnSi shows high spin-polarization of 93 % at room temperature experimentally.[4] Besides, the highest tunnel magnetoresistance (TMR) ratio record of 1995 % at a low temperature of 4.2 K and 354 % at room temperature were obtained when the Co_2MnSi Heusler compound was used in tunnel-junction devices.[5] Moreover, Mn-based Heusler compounds also attract much interest in the context of an inverse tetragonal structure, which has a high magnetocrystalline anisotropy value and is very promising in rare-earth-free permanent magnets.[6] Antiparallel coupling of magnetic moments on Mn atoms leads to the ferrimagnetic order, or antiferromagnetic order, which exhibits interesting properties such as non-collinear magnetism, topological Hall-effect, and skyrmions.[3]

There is no absolute definition of Heusler compounds. But generally, Heusler compounds consist of Half-Heusler, Full Heusler, Quaternary Heusler, Inverse Heusler and Tetragonal Heusler compounds, as illustrated in FIG. 1.1. The Half-Heusler has the composition 1:1:1 and $C1_b$ structure, formed by three interpenetrating FCC-lattices such as in CuMnSb, NiMnSb, and YbPtBi.[7, 8] In 1983, de Groot recognized that NiMnSb exhibits a peculiar band structure that is semiconducting in the minority-spin, but metallic in the majority spin channel.[9] This was named “half-metallic ferromagnetism” and was predicted to have 100 % spin polarization at the Fermi level. The Full Heusler compounds have the composition 2:1:1, i.e. X_2YZ and $L2_1$ structure, formed by four interpenetrating FCC-lattices as in Cu_2MnAl, Co_2MnSi, and Cu_2MnSn.[2, 10] Depending on the numbers of valence electrons and the Slater-Pauling rule, X_2YZ type of ternary Heusler may exhibit ferromagnetic, ferrimagnetic, antiferromagnetic or nonmagnetic

properties.[11] becasue the diversity of combination of X, Y, Z elements, ternary Heusler may behave as semiconductors, topological insulators, Weyl or Dirac semimetals, half-metals, spin-gapless semiconductors or normal metals. For example, Fe_2TiSi and Fe_2VAl are nonmagnetic semiconductors although it has magnetic Fe atoms occupied the 2 X sites.[12] Co_2CrAl and Co_2MnSi were ferromagnetic half-metals with high magnetoresistance as a signature for high spin polarization at room temperature.[13] It is found that Co and Mn are an excellent combination to achieve a high spin-polarization. Co_2TiGe is a ferromagnetic Weyl semimetal with Curie temperature calculated to be more than 630 K.[14] Mn_2CoAl with $L2_1$ structure is a spin-gapless semiconductor with one spin channel insulating and the other spin channel has zero bands gap.[15]

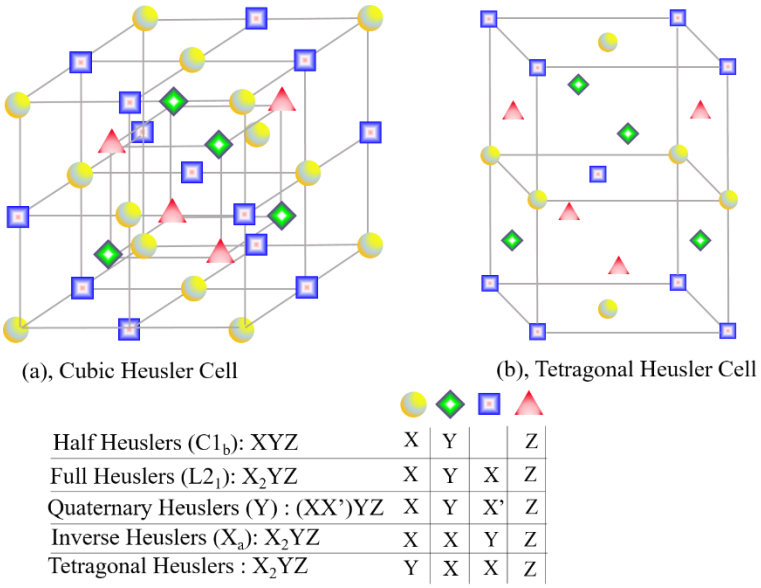

FIG. 1. 1 Schematic illustration of the various structures of Heusler compounds.

Another Heusler family is the LiMgPdSn-type quaternary Heusler compounds, also known as LiMgPdSb-type Heusler compounds. These Y-ordered quaternary compounds have the chemical formula (XX')YZ where X, X' and Y are transition metal

atoms. The valence of X' is lower than the valence of X atoms, and the valence of the Y element is lower than the valence of both X and X'. The sequence of the atoms along the FCC cube's diagonal is X-Y-X'-Z which is energetically the most stable. A few LiMgPdSn-type half-metallic and spin-gapless semiconducting compounds have been studied, for example, CoFeMnSi, FeVTiSi.[16] The fourth type of Heusler compounds is Inverse Full Heusler compounds. These compounds have also the chemical formula X_2YZ but in their case, the valence of the X transition metal atom is lower than the valence of the Y transition metal atom. And the Inverse Heusler compounds crystallize in the X_a structure, where the sequence of the atoms is X-X-Y-Z and the prototype is Hg_2TiCu.[17] The fifth type of Heusler compounds is Tetragonal Inverse Heusler, as shown in FIG. 1.1 (b). The compounds have the chemical formula X_2YZ, but the X is usually Mn atoms and Y, Z represents the transition metals and the main group metals, such as Mn_2RhSn, Mn_2RhGa.[6]

1.2 Chemical Disordering in Heusler Compounds.

Heusler are potentially promising materials in real devices to inject spins into semiconductors. The number of known ternaries and quarternary Heusler compounds with various multifunctionality for magnetoelectronics applications is increasing. In addition, the control of disorder and defects in these Heusler compounds plays an important role in synthesis process and affects the potential applications.

As mentioned in the above section 1.1, the Full Heusler compounds have the composition 2:1:1, i.e. X_2YZ, formed by four interpenetrating FCC-lattices such as

Cu_2MnAl, Co_2MnSi and Cu_2MnSn.[1,2] Depending on the synthesis process and the similarities between X, Y and Z atoms, Full Heusler compounds X_2YZ may have $L2_1$, B2, and/or A2 structures. FIG. 1.2 shows a schematic illustration of a unit cell of different types of chemical disordering. The full ordered structure of X_2YZ is $L2_1$ with a space group of Fm-3m (225) and prototype Cu_2MnAl, as shown in FIG 1.2 (a). Each Y or Z atom has eight X atoms as first neighbors in an octahedral symmetry position, while each X has four Y and four Z atoms as first neighbors and thus the symmetry of the crystal is reduced to the tetrahedral one. The X atoms occupying the two different sublattices are chemically equivalent as the environment of the one sublattice is the same as the environment of the second one but rotated by 90◦. The occupancy of two FCC sublattices by X atoms distinguishes the full-Heusler compounds with the $L2_1$ structure from the Half Heusler compounds with the $C1_b$ structure, like e.g. CoMnSb, where only one sublattice is occupied by Co atoms and the other one is empty. The B2 type structure is partially disordered with half of the Y and Z atoms interchange their positions (FIG 1.2 (b)). DO_3 type disorder is an exchange between the X and Y sites (FIG. 1.2 (c)). The A2 type structure is fully disordered with X, Y, and Z atoms randomly distributed at all available lattice sites (FIG. 1.2 (d)).

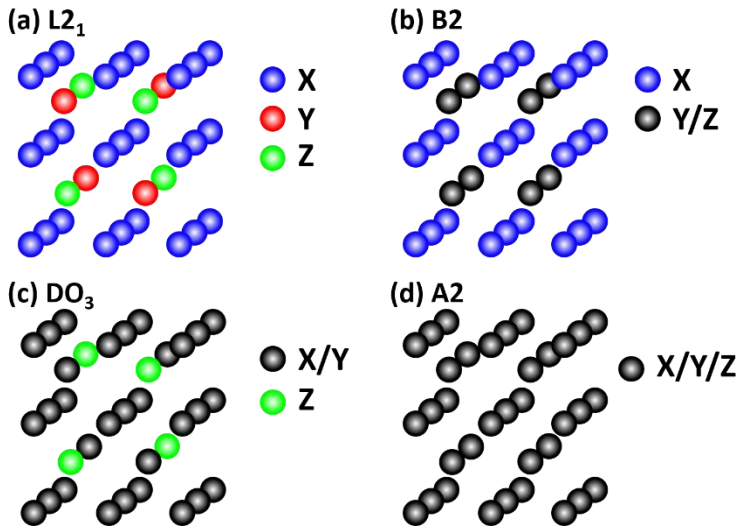

FIG. 1. 2 Schematic illustration of atom exchange of different types of chemical disordering in the unit cell.

At the stoichiometric composition, the disorder can exist in the form of partial interchange of atoms in different sublattices. A single disordering parameter α is used to describe the effects of certain types of preferential disorder on the structure amplitudes of compounds of the type X_2YZ. For compounds ordered in $L2_1$ structure, α is defined as the fraction of either Y or Z atoms being not on their correct sites. Partial occupation of Y and Z atoms on each other sublattices leads to $L2_1$/B2 type disorder. The B2-type structure can be obtained by allowing half of the Y and Z atoms to interchange their positions. The ratio of the $L2_1$/B2 depends on the heat treatments. Due to smaller interatomic distances in B2-type structure, an antiferromagnetic ordering becomes energetically favorable.[18]

Atomic ordering in Heusler compounds was evaluated by the Webster scheme of x-ray diffraction (XRD) analysis.[19-21] The general idea is that these ordered/disordered structures can be identified using the relations between atomic orderings and superlattice

diffraction lines. Y-Z disordering (FIG. 1.2 (b)) extinguishes odd superlattice diffraction lines which are defined by the index relation of *h*, *k*, and *l* = odd numbers, e.g., (111). Furthermore, even superlattices diffraction lines, i.e. (h+k+l) / 2 = 2n+1, e.g., (200) vanish under X-YZ disordering (FIG. 1.2 (d)). On the other hand, fundamental diffraction lines, i.e. (h+k+l) / 2 = 2n, e.g., (220) are independent of the ordering structures. Then there is an extention of the Webster model, the developed physical formalism for the degree of $L2_1$ ordering including correction from the degree of B2 ordering. The respective degrees of B2 order (A2 disorder) and $L2_1$ order (B2 disorder) can be calculated from the long-range order parameters:

$$S_{B2}^2 = I_{200} \cdot I_{400}^f / I_{400} \cdot I_{200}^f \quad [1.1]$$

$$(S_{L21}(3 - S_{B2})/2)^2 = I_{111} \cdot I_{220}^f / I_{220} \cdot I_{111}^f \quad [1.2]$$

where I_{hkl} and I_{hkl}^f are the experimental diffraction intensity for the (hkl) plane and its reference intensity calculated for fully ordered compounds.[22]

1.3 Magnetic Properties

Heusler compounds possess very interesting and diverse magnetic phenomena such as ferromagnetism, ferrimagnetism, itinerant and localized magnetism, antiferromagnetism, helimagnetism, Pauli paramagnetism or heavy-fermionic behavior.

Most of the Heusler compounds have ferromagnetic order and saturate in weak applied magnetic fields due to the Heusler compounds crystallizing in cubic structures with low magnetocrystalline anisotropy. For example, in X_2MnZ compounds, the magnetic moment is carried by Mn atoms with a value of saturation magnetization close

to 4 μ_B /f.u..[10] These compounds have localized magnetic properties, which depends on atomic disorder and changes in the electron concentration. It has been shown that the *sp* electron concentration is primarily important in establishing magnetic properties, influencing both the magnetic moment formation and the type of the magnetic order.

Although the majority of Heusler compounds are ferromagnetic, there are some with antiferromagnetic order, in particular, those compounds containing 3d elements in which the magnetic moment is only carried by Mn atoms at the Y site. Experimentally, the antiferromagnetic order has been measured in Half Heusler ($C1_b$) and Full Heusler compounds ($L2_1$, B2 and A2). Antiferromagnetism is more favorable in full Heusler compounds which have the B2-type crystal structure due to smaller interatomic Mn-Mn distances. For example, X_2MnZ (X = Ni, Pd; Z = Al, In).[23]

Ferrimagnetic ordering in Heusler compounds is due to the antiferromagnetic coupling of X and Y atoms, which is very rare in Heusler compounds compared to ferromagnetic or antiferromagnetic ordering. For example, Mn_2VAl and Mn_2VGa compounds were measured to be ferrimagnets.[24]

1.4 Half-Metallic Heuslers

Half-metallic ferromagnets (HMF) was initially proposed by de Groot *et al*. in the early 1980s.[9] In a half-metallic material, the two spin bands show a completely different behavior. The majority spin band shows typical metallic behavior, and the minority spin band exhibits semiconducting behavior with a gap at the Fermi level. This is shown schematically in FIG. 1.3 (a). The band gap is the essential ingredient in half-metals, and it is reported three categories can be distinguished on the basis of the nature of the band

gap: half-metals with (1) covalent band gaps, (2) charge-transfer band gaps, and (3) *d* - *d* band gaps.[25] This distinction is important because the origin of the half-metallicity is different in each category. Covalent band gaps are strongly related with the crystal structure. A well-known example is NiMnSb.[9] It crystallizes in the Heusler $C1_b$ structure, which is closely related with the zincblende structure: One of the empty positions is occupied by the third element (Ni). Both Mn and Sb must occupy sites with tetrahedral coordination. The band structure, interactions, and bonding for the semiconducting spin direction are equivalent to those in the group III–V semiconductors such as GaAs. The metallic spin direction shows conduction in very wide bands with an effective mass approximately equal to the free-electron mass. Charge-transfer band gaps are found in strongly magnetic compounds, where the *d* bands of the transition metal are empty for the minority spin direction and the itinerant *s*, *p* electrons of the transition metal have been localized on the anions. Materials with a *d*-*d* band gap show rather narrow bands, so that gaps occur between crystal-field split bands. The exchange splitting can be such that the Fermi level is positioned in a gap for one spin direction only.

In HMFs, the existence of the gap leads to 100% spin polarization at the Fermi level and thus a fully spin-polarized current should be feasible in these compounds, maximizing the efficiency of magnetoelectronic devices. For example, Bowen *et al*. have observed such a current in trilayers made up of half-metallic $La_{0.7}Sr_{0.3}MnO_3$ as electrodes and SrO_3 as a barrier.[26] Other known half-metallic materials except for the semi- and full-Heusler compounds are some oxides CrO_2 and Fe_3O_4.[27] Although thin films of CrO_2 and $La_{0.7}Sr_{0.3}MnO_3$ have been verified to present practically 100% spin polarization at the Fermi level at low temperatures,[27, 28] the Heusler compounds remain attractive for

technical applications like spin-injection devices, spin filters, tunnel junctions, or GMR devices due to their relatively high Curie temperature compared to these compounds.

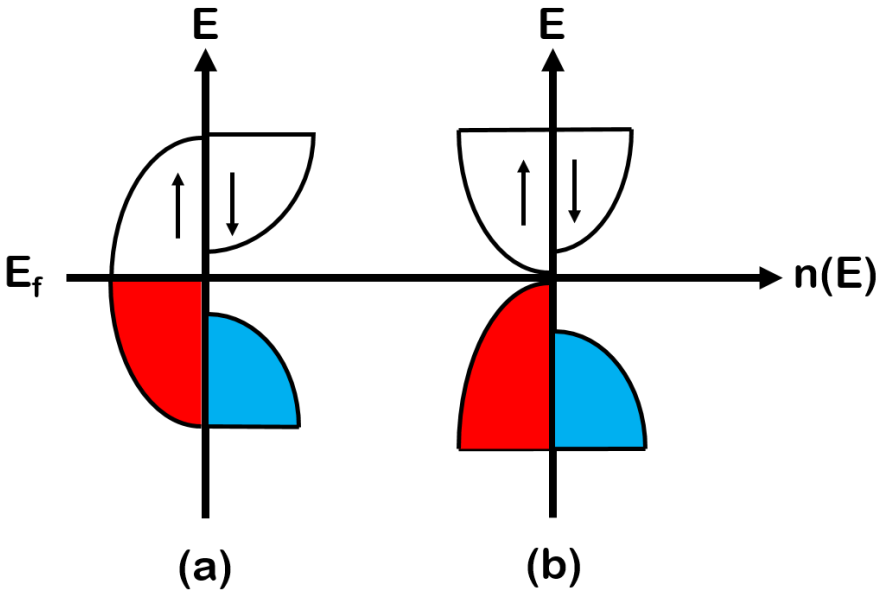

FIG. 1. 3 The schematic density of states n(E) as a function of energy E for a half-metallic ferromagnet (a), a spin-gapless semiconductor (b). The occupied states are indicated by filled areas. The arrows indicate the majority (↑) and minority (↓) states.

The most-well known half-metallic Half-Heusler compound is NiMnSb, i.e., the minority band is semiconducting with a gap at the Fermi level (E_F), leading to 100% spin polarization at E_F.[9] The loss of half-metallicity in the NiMnSb thin films is due to the segregation of Sb and Mn atoms to the surface, which is far from perfect.[29] Later on, Full Heusler compounds such as Co_2MnX (X = Si, Ge),[30] Co_2FeX (X = Ga, Ge, Al, Si, Sn),[31] Mn_2CoX (X = Al, Ga, In, Si, Ge, Sn, Sb),[32] were calculated to be half-metallic with 100% spin polarization at E_F. Full Heusler compounds became very popular for potential applications. Several groups managed to grow Co_2MnGe and Co_2MnSi thin films. But highest spin polarization (P) value of Co_2MnSi at room temperature is 93% via

Ultraviolet Photoemission Spectroscopy (UPS),[4] which is less than the predicted 100%. It has been shown that disorder, defects and vacancies can lead to loss of the half-metallic character.[29, 33] However, a magnetic tunnel junction device was still built based on Co_2MnSi. Record value of TMR ratio around 1995% at low temperature and 354% at room temperature were obtained.[34, 35] Similar experiments have been undertaken by Inomata and collaborators using $Co_2Cr_{0.6}Fe_{0.4}Al$ as the magnetic electrode.[36] Development of TMR for Heusler compounds is presented in FIG. 1.4.

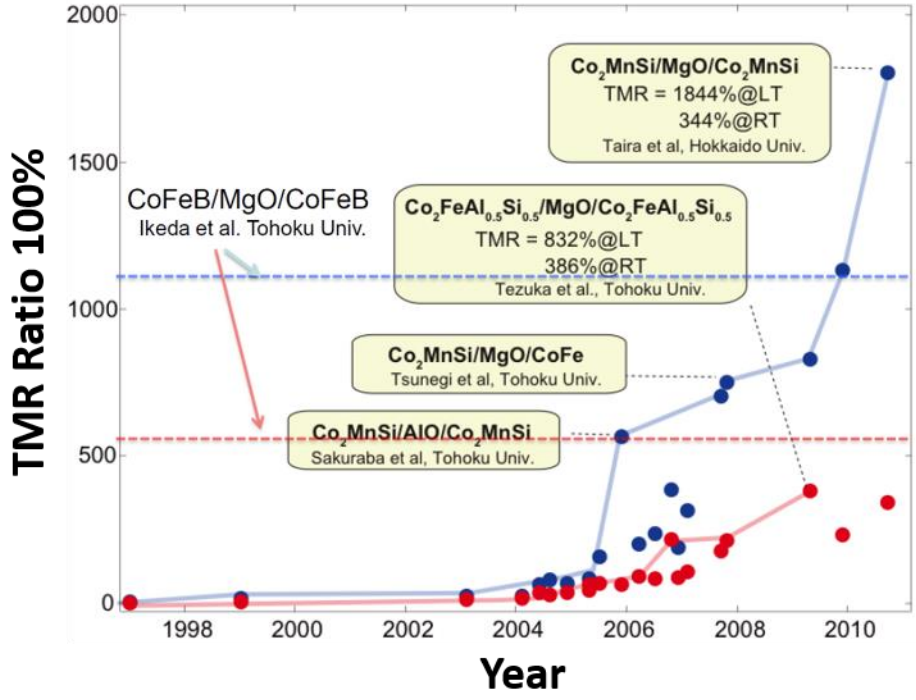

FIG. 1. 4 Development of TMR for Heusler compounds is presented.[5, 37, 38]

1.5 Spin-Gapless Semiconductor (SGS)

Magnetic semiconductors are compounds combining both the semiconducting behavior with the magnetic properties. Such compounds can offer novel functionalities to spintronic and magnetoelectronic devices, e.g., they can act as spin-filter materials. Such

materials can find application in magnetic tunnel junctions (MTJ). Then the probability for electrons tunneling through the spin-filter barrier is different for the two spin directions and the flow of a spin-polarized current can be achieved.[39] A special class is the so-called spin-gapless semiconductors. These materials combine the properties of half-metals and magnetic semiconductors, and they are actually magnetic semiconductors where there is an almost vanishing energy gap at the Fermi level in the majority-spin direction and a normal energy gap in the other spin-direction, as shown in Fig. 1. (b).[40] Spin-gapless semiconductors also offer novel functionalities due to their unique properties: (i) the mobility of carriers is considerably larger than in usual semiconductors, (ii) excited carriers include both electrons and holes which can be 100% spin-polarized simultaneously, and (iii) a vanishing amount of energy is enough to excite majority spin electrons from the valence to the conduction band.

Although gapless-semiconductors are well known in the literature,[40] it was not until 2008, that Wang proposed that the Co-doping of $PbPdO_2$, a gapless semiconductor, with transition metal atoms would lead to a spin-gapless semiconductor.[41, 42] Experimental confirmation was offered via study of polycrystalline films of Mn and Co doped $PbPdO_2$.[43] Among Heusler compounds several have been identified to be spin-gapless semiconductors, as summarized in Table 1.1. The main attention was given to Mn_2CoAl, an Inverse Full- Heusler compound, due to its successful growth in the form of films. In 2008 Liu and collaborators synthesized Mn_2CoAl using an arc-melting technique and found that it adopted the lattice structure of Inverse Full-Heusler with a lattice constant of 5.8388 Å and a total spin magnetic moment of 1.95 μ_B per formula unit.[32] The breakthrough took place in 2013 when Ouardi *et al*. identified the spin-gapless

behavior of Mn_2CoAl and have confirmed it experimentally in bulk-like polycrystalline films.[15] They found an experimental lattice constant of 5.798 Å, a Curie temperature of 720 K and a total spin magnetic per formula unit of 2 μ_B at a temperature of 5 K. Following this research, Jamer and collaborators have grown thin films of 70 nm thickness on GaAs,[44] but these films were found to deviate from the spin-gapless semiconducting behavior. On the contrary, films grown on a thermally oxidized Si substrate were found to be spin-gapless semiconductors with a Curie temperature of 550 K.[45] *Ab-initio* calculations of Skaftouros *et al*. identified among the inverse Heusler compounds another four potential SGS materials: Ti_2CoSi, Ti_2MnAl, Ti_2VAs and Cr_2ZnSi, with the latter three being also fully-compensated ferrimagnets, and V_3Al for which one V sublattice is not magnetic and the other two form a conventional antiferromagnet.[46] CoFeMnSi and CoFeMnGe have also been identified to be SGSs and experimentally realized by Bainsla *et al*.[47] Perfectly ordered CoFeCrAl, which has been predicted to be a spin-gapless semiconductor, crystallizes in the cubic Heusler-type Y structure (prototype LiMgPdSn).[48] Galanakis and collaborators have also shown that defects keep the half-metallic character of Mn2CoAl but destroy the spin-gapless semiconducting character.[33]

Table 1.1: Summary of Heusler compounds with potential SGS properties.[16, 48-52]

Compound	Valence electron number	Magnetic moment (μ_B)/f.u.		Magnetic ordering temp. (K)	Lattice parameter a (Å)	Crystal Structure type	
		Th.	Exp.		Th.	Exp.	
Mn_2CoAl	26	2	2	720 (Exp.)	5.73	5.798	XA
CoFeMnSi	28	4	3.7	620 (Exp.)	5.60	5.658	Y
CoFeCrAl	26	2	2.1	540 (Exp.)	5.70	5.75	Y
Ti_2CoSi	21	3	N/A	400 (Th.)	6.03	N/A	XA
Ti_2MnAl	18	0	N/A	960 (Th.)	6.24	N/A	XA
Cr_2ZnSi	28	0	N/A	1040 (Th.)	5.85	N/A	XA
Ti_2VAs	18	0	N/A	800 (Th.)	6.23	N/A	XA
CoMnCrSi	26	2	N/A	Predicted high (Th.)	5.63	N/A	Y

1.6 Temperature Dependence of Electrical Resistivity

Collisions of electrons in a metal cause the resistivity. Impurity scattering and electron-phonon scattering are the two most common processes in metals. Defects change the periodic lattice of ions, leads to electron scattering and gives a temperature-independent contribution to the resistivity. The electron-phonon scattering process is the interactions of thermal fluctuations of the crystal lattice with conduction electrons. The lattice vibrations (phonons) are characterized by a characteristic temperature known as the Debye temperature, θ_D. Electron-phonon scattering is directly proportional to the temperature T. Below θ_D, electron-phonon scattering scales as T^3, and at the lowest temperatures, the electron-phonon scattering scales as a T^5 dependence known as the Bloch Law.[53, 54] However, in a ferromagnets, the temperature dependence of the resistivity can be affected by another scattering called magnon scattering. Magnons are quantized spin waves analogous to lattice vibration (phonons) and magnon scattering leads to a quadratic temperature dependence of the resistivity. The resistivity with combined scattering of residual (ρ_R), magnonic (ρ_M), and phononic (ρ_P) contribution, $\rho(T) = \rho_R + \rho_M(T) + \rho_P(T)$. [55] The residual resistivity ρ_R is temperature independent and caused by defects of the ideal crystal lattice. An upturn in the resistivity ρ at low temperatures (typically < 40 K) has been observed in half-metallic ferromagnets, which is attributed to weak localization and it is commonly observed in disordered metallic systems.[56]

1.7. The Hall-effect

1.7.1. Ordinary Hall-effect

The Hall-effect (or the ordinary Hall-effect) phenomena was found by Edward Hall in the 1870s.[57] This effect was observed in both semiconductors and metals. The Hall-effect is defined by the voltage difference across the electrical conductor, transverse to the longitudinal electric current in the conductor with the magnetic field is normal to the current, as shown in FIG. 1.5.

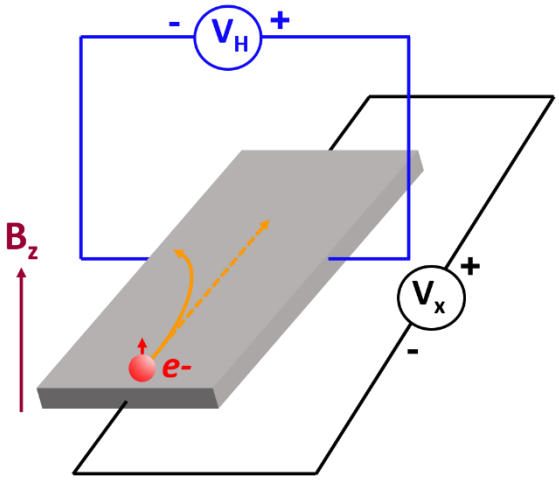

FIG. 1. 5 Hall-effect measurement setup for electrons. Initially, the electrons follow the curved arrow, due to the magnetic force. At some distance from the current-introducing contacts, electrons pile up on the left side and deplete from the right side, which creates an electric field in the direction of the assigned V_H. V_H is negative for some semiconductors where "holes" appear to flow.

The Hall-effect is due to the nature of the current, which consists of the movement of charge carriers, typically electrons, holes, ions or all three. When a perpendicular magnetic field is applied, the carriers experience the Lorentz force and the

carriers accumulate on one side of the material. This finally leaves equal and opposite charges on the both sides. For example, in a simple metal where there is only one type of charge carrier (electrons) the Hall voltage V_H can be derived using the Lorentz force. In the steady-state condition, charges are not moving in the y-axis direction because the magnetic force on each electron in the y-axis direction is canceled by a y-axis electrical force due to the buildup of charges. The v_x term is the drift velocity of the current which is assumed at this point to be holes by convention. The $v_x B_z$ term is negative in the y-axis direction by the right-hand rule.[53, 58, 59]

$$\boldsymbol{F} = q[\boldsymbol{E} + (\boldsymbol{v} \times \boldsymbol{B})] \quad [1.3]$$

$$0 = E_y - v_x B_z \quad [1.4]$$

The Hall voltage is described by

$$V_H = \frac{I_x B_z}{nte} \quad [1.5]$$

The Hall coefficient is

$$R_H = \frac{E_y}{j_x B_z} = \frac{V_H t}{IB} = -\frac{1}{ne} \quad [1.6]$$

As a result, the Hall-effect is very useful as a means to measure either the carrier density or the magnetic field.

When a semiconductor with both electrons and holes is measured in a magnetic field, the charge carriers of the semiconductor experience a force in a direction perpendicular to both the magnetic field and the current. Hall coefficient in semiconductor is

$$R_H = \frac{p\mu_h^2 - n\mu_e^2}{e(p\mu_h + n\mu_e)^2} \quad [1.7]$$

where n is the electron concentration, p is the hole concentration, μ_e the electron mobility, μ_h the hole mobility and e the elementary charge.

1.7.2. Anomalous Hall-effect (AHE)

Experimental observations found that the dependence of the Hall resistivity ρ_{xy} on applied perpendicular field $\mathbf{H}_z$ is qualitatively different in ferromagnetic and nonmagnetic conductors. ρ_{xy} increases linearly with $\mathbf{H}_z$ for nonmagnetic conductors, whereas ρ_{xy} increases steeply in weak $\mathbf{H}_z$ but saturates at a large value. For example, in Fe, Co, and Ni, the saturation value is roughly proportional to the magnetization $\mathbf{M}_z$ and has weak anisotropy associated with the crystal anisotropy. An empirical relation between ρ_{xy}, $\mathbf{H}z$ and $\mathbf{M}_z$ is $\rho_{xy} = R_0 H_z + R_s M_z$.[58] The second term represents the Hall-effect contribution due to the spontaneous magnetization. This is Anomalous Hall-effect. R_0 depends mainly on the density of carriers, however, R_s was found to depend subtly on a variety of material specific parameters and, in particular, on the longitudinal resistivity ρ_{xx}.

In 1954, it was found when an external electric field is applied to a solid, electrons acquire an additional contribution to their group velocity. This anomalous velocity was perpendicular to the electric field and therefore contributed to the Hall-effects.[59] For ferromagnetic conductors, the sum of the anomalous velocity over all occupied band states depends only on the band structure and is largely independent of scattering and referred to as the *intrinsic* contribution to the AHE. In other words, inter-band coherence induced by an external electric field gives rise to an E velocity contribution perpendicular to the field direction. These currents do not sum to zero in ferromagnets. Electrons have an anomalous velocity perpendicular to the electric field

related to their Berry's phase curvature. Later on, Smit argued the main source of the AHE currents was asymmetric (*skew*) scattering from impurities caused by the spin-orbit interaction.[60] This picture predicted that $\rho_{xy} \sim \rho_{xx}$. Asymmetric scattering due to the effective spin-orbit coupling of the electron or the impurity. In contrast, Berger argued that the main source of the AHE current was the *side jump* experienced by quasi-particles upon scattering from spin-orbit coupled impurities.[61] This theory predicted that $\rho_{xy} \sim \rho_{xx}^2$. The electron velocity is deflected in opposite directions by the opposite electric fields experienced upon approaching and leaving an impurity. The time-integrated velocity deflection is the *side jump*.[61] The three main mechanisms considered in this early history are shown schematically in FIG. 1.6. Thus, if all mechanisms are operative the total AHE conductivity is given by the following equation,

$$\sigma_{xy}^{AH} = \sigma_{xy}^{AH-int} + \sigma_{xy}^{AH-skew} + \sigma_{xy}^{AH-sj} \qquad [1.8]$$

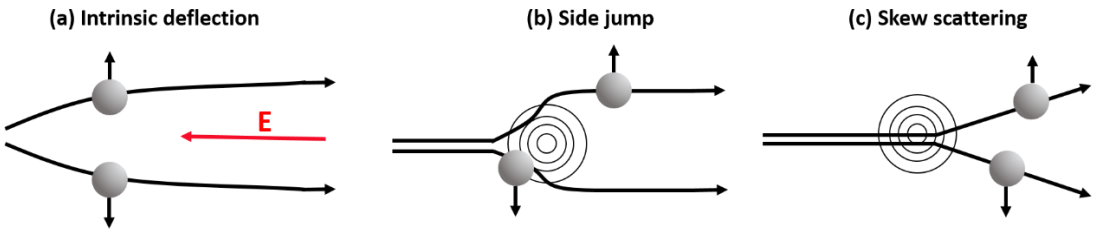

FIG. 1. 6 Illustration of the three main mechanisms that can give rise to an AHE. In any real material, all of these mechanisms act to influence electron motion.[62]

1.8 Magnetoresistance

Magnetoresistance is a change of the electrical resistance of a material in an applied external magnetic field. There are a variety of effects that can be called

magnetoresistances such as geometrical magnetoresistance, Shubnikov-de Haas oscillations, the common positive magnetoresistance in metals, negative magnetoresistance in ferromagnets, anisotropic magnetoresistance (AMR), giant magnetoresistance (GMR), tunnel magnetoresistance (TMR), and extraordinary magnetoresistance (EMR).[53] The first magnetoresistive effect with a 5% electrical resistance ratio was discovered in 1851. AMR was discovered in 1857 and used in early hard disk designs.[63] Later on, GMR was discovered in 1988 in ferromagnetic/nonmagnetic/ ferromagnetic multilayered systems due to interlayer exchange coupling.[64] Grünberg and Fert discovered the antiferromagnetic coupling effect in Fe/Cr/Fe multilayered system, as shown in FIG. 1.7 and were awarded the Nobel prize in Physics in 2007. The effect in a GMR multilayer is explained in FIG. 1.8.[65, 66] For the parallel-aligned case, one spin channel experiences small or no spin scattering through both ferromagnetic layers. This leads to a low-resistance state. In the anti-parallel aligned case, both spin channels experience spin scattering in one of the ferromagnetic layers leading to a high-resistance state. Electric current can be passed through magnetic superlattices in two ways. In the current-in-plane (CIP) geometry, the current flows along the layers, and the electrodes are located on one side of the structure. In the current perpendicular-to-plane (CPP) conFiguration, the current is passed perpendicular to the layers, and the electrodes are located on different sides of the superlattices. The CPP geometry results in more than twice higher GMR but is more difficult to realize in practice than the CIP conFiguration. However, CPP-GMR is the current focus of much research interest due to its applicability to current generation MRAM.[67]

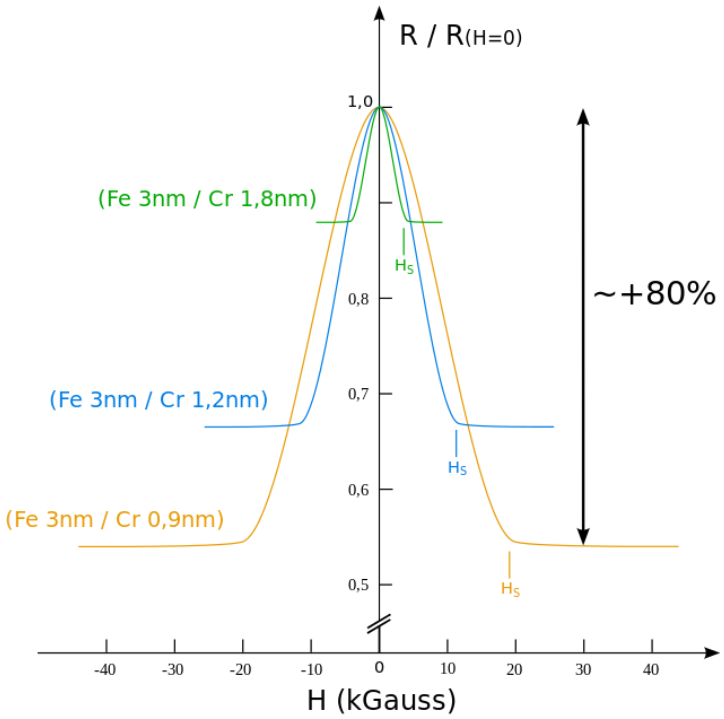

FIG. 1.7 The founding results of Fert and Grünberg: change in the resistance of Fe/Cr/Fe superlattices at 4.2 K in external magnetic field H. The current and magnetic field were parallel to the [110] axis. The arrow to the right shows maximum resistance change. H_s is the saturation field.[64]

If the non-magnetic spacer is replaced by an insulating spacer such as MgO or Al_2O_3, then tunneling magnetoresistance (TMR) can occur. In 1975, Julliere reported for the first time an MR ratio of 14% between parallel and anti-parallel states at 4.2K.[68] Then in the 1990s, room temperature TMR ratio of 18% was reported by Miyazaki.[69] Up to now, there has been much greater interest in using crystalline MgO barriers. Theoretical calculation predicted TMR ratios of over 1000% for MgO barriers.[70] Experimentally, the highest value of TMR ratio of 600% at room temperature have been achieved for

CoFeB/MgO/CoFeB multilayer films.[71] Compared to GMR, TMR is fundamentally different. TMR depends on the conduction states which could tunnel into across the barrier, as shown schematically in FIG. 1.9.[72] For the parallel orientation there are a large number of majority conduction states and majority valance states resulting in a large electron flow and thus low resistance. For the anti-parallel orientation, there are the fewer majority and minority states resulting in a high resistance. This makes TMR dependent upon the number of available states for each spin direction at the Fermi level, i.e. the spin polarization, equation [1.9].[64]

$$TMR = \frac{2P_1P_2}{1-P_1P_2} \qquad [1.9]$$

Note that P_1 and P_2 are the spin polarizations of ferromagnetic layers in the junction. It means that for Heusler compounds studied in this work, the achievable TMR should be extremely high due to large values of spin polarization from these materials.

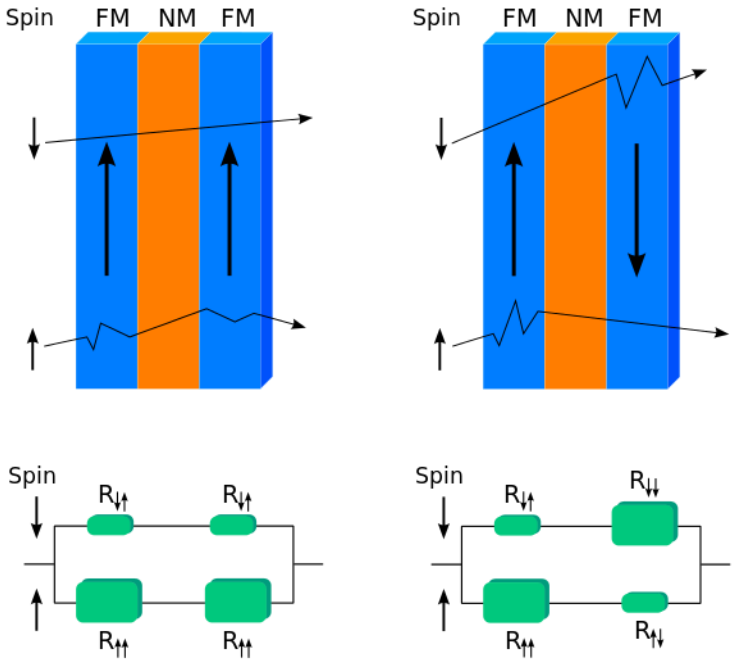

FIG. 1. 8 A schematic representation of GMR using a simple resistor network model. In the left picture, the spin-up channel is the majority spin channel in both the ferromagnetic layers, experiencing a low resistance (R↑) throughout the structure. In the right-hand picture, the spin-up channel is the majority spin channel (R↑) in the first magnetic layer but the minority-spin channel (R↓) in the second magnetic layer and vice versa for the spin-down channel. Neither spin channel is of low resistance throughout the structure and the overall resistance state of the structure is high. GMR occurs when the relative orientation of the magnetic layers is switched, usually by the application of a magnetic field.[66]

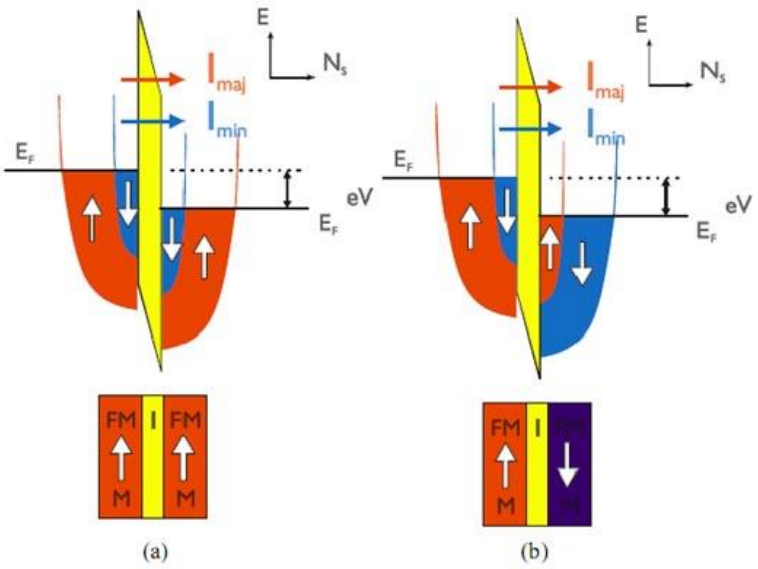

FIG. 1. 9 Schematic illustration of the TMR effect. In a magnetic tunneling junction, the density of states of both plates determines whether a large current (a) or small current (b) tunnels through.[68, 72]

1.9 Spin Polarization

Highly spin-polarized ferromagnetic materials as spin-polarized current sources are strongly desired for spintronics devices such as magnetic tunnel junctions (MTJs), spin injectors to semiconductors and spin-torque oscillators.[73-75] A minority of Heusler compounds are calculated to be half-metals and particularly promising as the ferromagnetic electrodes of magneto-resistive devices since they have high Curie temperatures and high spin polarization. The spin polarization (P) is defined as

$$P = \frac{N\uparrow - N\downarrow}{N\uparrow + N\downarrow} \qquad [1.10]$$

where $N\uparrow$ and $N\downarrow$ are the spin-up and spin-down density of states (DOS) at the Fermi level (E_F). The values of P can be experimentally estimated by superconducting

tunneling spectroscopy (STS),[76] Julliere's model for MTJ,[68] or point contact Andreev reflection (PCAR) (transport spin polarization weighted by v or v^2).[27] Spin resolved x-ray photoelectron spectroscopy also has been reported to measure spin states at surfaces and with large spin polarization P value of 93% of Co_2MnSi at room temperature.[4] The first STS measurement of P was carried out on Fe, Co and Ni. The obtained P values for Fe, Co and Ni are 44%, 34% and 11%, respectively.[76] Besides, the spin polarizations of electrode materials of MTJs were estimated by the Julliere model.[68] For example, due to the MgO barrier in Fe/MgO/Fe, a P value of Fe is estimated to be greater than 80% compared to a bulk P value of 40%.[77] Compared to the above mentioned two methods, point contact Andreev reflection (PCAR) is a relatively easier method to estimate the spin polarization of bulk and thin film materials promptly for screening promising materials.[74] The transport spin polarization measurement by PCAR utilizes the Andreev reflection that occurs at a point contact between a normal conductor and a superconductor. The Andreev reflection occurs at a point contact between a normal conductor and a superconductor. Electrons can flow from normal conductors to semiconductors by forming Cooper pairs of spin-up and spin-down electrons when the energy of the incident electrons is smaller than the superconducting band gap. if the normal conductor doesn't have polarization of spins (P = 0), the same number of spin-up and spin-down electrons are present at E_F, so they can form Cooper pairs and thus the conductance is enhanced to double within the superconducting gap. Andreev reflection is effect that holes are reflected to the normal conductor in order to conserve the momentum in the system. On the contrary, the Andreev reflection is suppressed due to the different DOS of spin-up and spin-down in ferromagnetic materials. If the ferromagnetic materials are perfectly

spin-polarized, i.e. P = 100%, there is no electron to form a Cooper pair and the conductance in the superconducting gap is completely suppressed. The final spin polarization of measured materials is deduced by fitting the conductance curve to the modified BTK model under the assumption of the electron scattering because of the surface oxidation.[78]

1.10 Spintronics and Devices

Spintronics is an emerging field based on electron charges and spins.[79, 80] Today's information technology needs larger capacity data storage and faster data processing. Since the possibility of reaching the physical limits in both ferromagnet-based memories and conventional semiconductor-based electronic processors is known, an interdisciplinary field between magnetism and electronics is required. Spintronics, based on spin-polarized electron transport, is believed to meet the requirements for future technologies. Studies of spintronics started in 1988 after the discovery of giant magnetoresistance (GMR),[64] which was implemented into hard disk drives (HDD), allowing for a drastic increase in the areal density due to the increased sensitivity of the GMR read heads. In spintronic devices, efficient generation of a spin-polarized current is an essential issue. The most common method is spin injection from a ferromagnetic material, e.g., conventional ferromagnetic metals (Fe, Co, Ni, and Gd), half-metallic ferromagnets (HMF)[9] and dilute magnetic semiconductors (DMS).[81] Conventional ferromagnets typically possess a spin polarization of <50% and hence cannot inject electrons with a large degree of spin polarization into the non-magnetic material.[82] The injected spin polarization could be increased by employing an HMF or a DMS, both of which might have 100% spin polarization in theory. In a DMS, Curie temperatures are

typically below 80 K.[81] In order to satisfy the above requirements, HMFs have been rigorously investigated to exploit 100% spin polarization induced by spontaneous magnetization.[83] However, to date, there have been no experimental reports demonstrating half-metallicity at room temperature, crucial for device applications. Among the many theoretically proposed HMFs, Heusler compounds hold the greatest potential to realize half-metallicity at room temperature due to their high Curie temperatures (above room temperature), lattice constant matching with major substrates (such as III–V semiconductors and MgO), and generally large gap (δ) at E_F.[84] The addition of the spin degree of freedom to the conventional electronic devices based on semiconductors has several advantages like non-volatility, increased data processing speed, decreased electric power consumption and increased integration densities.[79]

1.10.1 Magnetic Tunnel Junctions (MTJs)

If two conducting electrodes are separated by a thin dielectric layer as a tunnel layer and the thickness ranges from a few angstroms to a few nanometers, electrons can tunnel through the tunnel barrier and result in electrical conduction. The evanescent transmission of electrons through the tunnel barrier leads to the exponential dependence of the tunneling current with the barrier thickness. In a typical MTJ device, the two electrodes are ferromagnetic materials such as CoFe, and/or CoFeB. Recently, Heusler compounds were applied in MTJ. In a ferromagnetic material, the electrons have two spin states, i.e. either spin-up or spin-down. In a tunneling process in which electron spin is conserved, the tunneling conductance depends on whether the magnetizations M_1 and M_2 of the two electrodes are parallel or antiparallel. The difference in the electronic density

of states (DOS) at the Fermi level E_F between spin-up $N\uparrow(E_F)$ and spin-down $N\downarrow(E_F)$ electrons decided the tunneling magnetoresistance (TMR) ratio. Because the electron spin is conserved, i.e. electrons preserve their spin orientation during the tunneling process, electrons can only tunnel into the subband of the same spin orientation. FIG. 1.10 is a schematic illustration of electron tunneling of two spin states.[72] The tunneling conductance is proportional to the product of the Fermi level DOS values of the two electrodes with same spin orientation. A change of magnetization from parallel to antiparallel of the two ferromagnetic materials lead to an exchange between the two spin subbands of one of the ferromagnetic material for the tunneling process. Consequently, a corresponding change in resistance will be measured. The definition of TMR ratio is given by Eqn. [1.9].

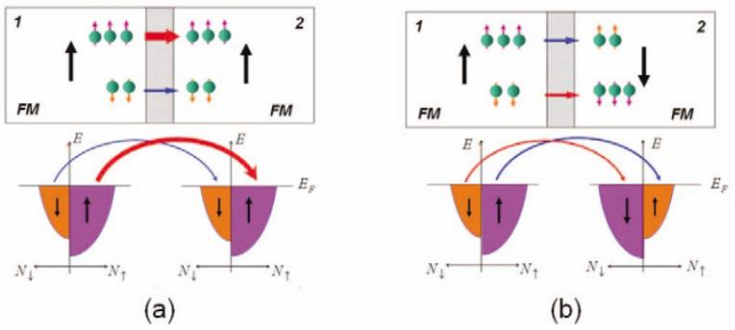

FIG. 1. 10 Schematic of the TMR effect in an MTJ. During tunneling, electron spin orientation is preserved, i.e. an electron can only tunnel to the spin subband of the same spin orientation, and the conductance is proportional to the product of the Fermi level DOS values of the two electrodes of the same spin orientation. A change from the parallel conFiguration (a) to the antiparallel conFiguration (b) of the magnetizations of the two

electrodes results in an exchange of the spin subband for electrode 2, causing a corresponding change in the conductance.[72]

Early MTJs utilized amorphous AlO_x tunnel barrier and exhibited significant TMR ratios at room temperature. Then, a series of theoretical calculations predicted extremely high TMR ratios for MTJs using MgO barrier and experimental results confirmed that. For example, observed TMR ratio of 604% at 300 K in pseudo-spin-valve MTJ Ta/$Co_{20}Fe_{60}B_{20}$/MgO/$Co_{20}Fe_{60}B_{20}$/Ta annealed at 525 °C and the highest TMR ratio observed at 5 K was 1144% for this MTJ in 2008.[71] Some Heusler compounds were tentatively applied in MTJ replacing CoFeB such as Co_2MnSi and Co_2(Cr, Fe)Al and have already obtained large TMR of 1995% at 4.2K and 354% at 300K in Co_2MnSi.[34]

1.10.2 Hard Disk Drives (HDDs)

One application of MTJs is in hard disk drive (HDD) read heads.[85] Disk read/write heads are the small parts of a disk drive that move above the disk platter and transform the platter's magnetic field into electrical current (read the disk) or, vice versa, transform electrical current into a magnetic field (write the disk). The separate read head uses the magnetoresistive (MR) effect. These MR heads are able to read very small magnetic features reliably, but cannot be used to create the strong field used for writing. The read heads of HDD product are made of TiO_x-based MTJs in early times. The detailed structure of an MTJ read head in an HDD is illustrated in FIG. 1.11.[86] It has one free layer to sense magnetic flux from the magnetic disk medium in a rotation of its magnetization in response to the flux. The other magnetic electrode is known as the reference layer. Its magnetization orientation is ‘fixed’ normal to the disk surface by

being next to a pinned layer and an antiferromagnetic layer with a metallic barrier between them. The magnetic moment orientation of the pinned layer is constrained by an effective surface magnetic field, known as an exchange bias field, which arises from the interface with the antiferromagnetic layer. The purpose of the pinned layer is to compensate the stray field from the reference layer. Hence, the magnetic moment of the pinned layer is always opposite to that of the reference layer. This is done by introducing a strong antiparallel coupling between them by choosing a particular metallic interlayer of adequate thickness.

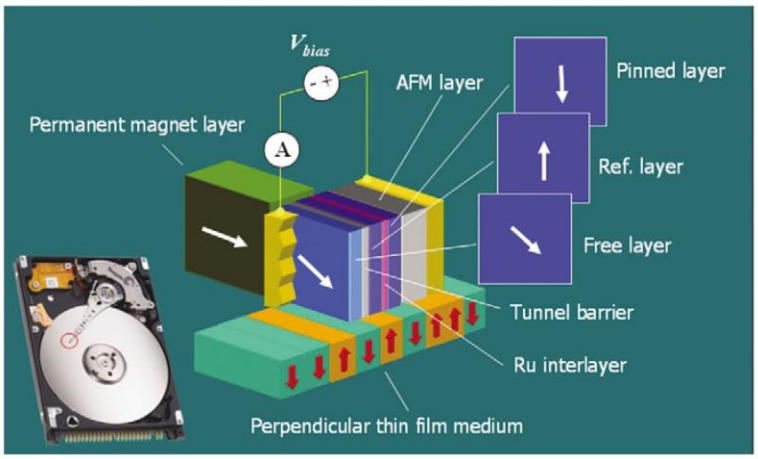

FIG. 1. 11 MTJ read head in an HDD. One magnetic electrode is a free layer, and its magnetization rotates freely in response to the medium signal field. The magnetic moment of the other electrode is 'fixed' through the interlayer magnetic coupling and functions as a reference to the free layer magnetization orientation.[72, 86]

Nowadays, almost 80% of information and data is currently stored magnetically onto hard disk drives (HDDs), whose areal density has increased rapidly. HDD media is typically CoPtCr.[87] The current magnetic media has a perpendicular magnetic anisotropy (PMA), providing much greater stability than the early media of in-plane magnetic

anisotropy. The stability of the recording depends on the grain size of the media. The main methods to lower the noise from the magnetic media is to lower the grain size. The energy stored in one grain is defined as K_uV, where K_u is anisotropy constant and V is grain volume. For example, in order to store data for 10 years, thermal stability K_uV/k_BT, therefore, needs to exceed 60, where k_B is Boltzmann constant and T is temperature. Since the current film-growth techniques can make the grain size to be around 5 nm, a main contribution is to search for higher K_u magnetic media which could be applied in HDDs, although heat-assisted magnetic recording technique may be a solution. Recently, theoretical calculations have predicted tetragonal Heusler compounds may have a rather high magnetic anisotropy constant. Additionally, experiments also found that the substrates induced distortion can also introduce very high K_u.[67]

1.10.3 Magnetic Random Access Memory (MRAM)

As well as exploring different methods to increase the storage capacity of HDDs there is great interest in technologies which could replace them. One of the major ongoing device studies is in magnetic random access memory (MRAM). MRAM is a non-volatile random-access memory technology.[72, 88] Data in MRAM is not stored by magnetic storage elements. The elements are formed from two ferromagnetic layers, each of which can be a magnetized, separated by a thin insulating layer such as MgO. One layer is a permanent magnet set to a particular polarity, i.e. pin layer. The magnetization of the other layer can be switched to match that of an external field to store memory. This configuration is known as a magnetic tunnel junction and is the simplest structure for an MRAM bit. The simplest method of reading is accomplished by measuring the electrical resistance of the cell. For example, by powering an associated transistor that switches

current from a supply line through the cell to ground, the electrical resistance of the cell changes due to the relative orientation of the magnetization in the two layers due to the tunnel magnetoresistance. By measuring the resulting current, the resistance inside any particular cell can be determined, and from this the magnetization polarity of the writable plate. Typically, if the two layers have the same magnetization alignment (low resistance state) this is recorded to be "1", otherwise, antiparallel magnetization is recorded to be "0", as shown in FIG. 1.12. This is the same with TMR mechanism. Half-metallic magnetic Heusler compounds may be expected to be applied in this device due to a high spin-polarization values.

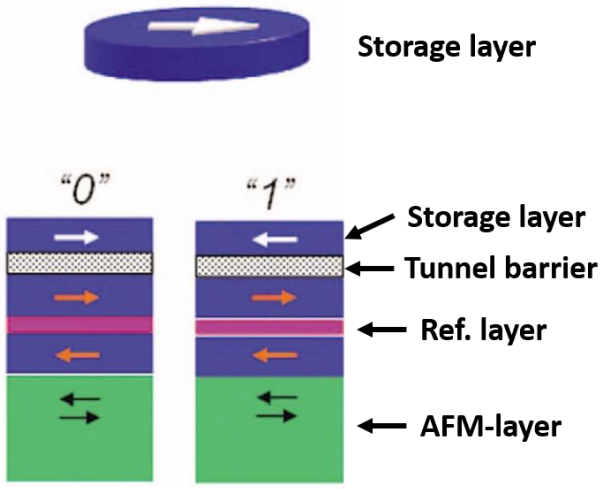

FIG. 1. 12 Schematic illustration of a memory element design with a single storage layer.[72]

A newer technique, spin-transfer torque (STT) or spin-transfer switching, uses spin-aligned ("polarized") electrons to directly torque the domains.[89] Specifically, if the electrons flowing into a layer have to change their spin, this will develop a torque that will be transferred to the nearby layer. This lowers the amount of current needed to write the cells, making it about the same as the read process. There are concerns that the "classic" type of MRAM cell will have difficulty at high densities due to the amount of current needed during writes, a problem that STT avoids. For this reason, the STT proponents expect the technique to be used for devices of 65 nm and smaller. The downside is the need to maintain the spin coherence. Overall, the STT requires much less write current than conventional or toggle MRAM.

1.11 Bibliography

1. F. Heusler, "Über magnetische Manganlegierungen", Verhandlungen der Deutschen Physikalischen Gesellschaft. **12**, 219 (1903).

2. M. Bouchard, "Electron metallography and magnetic properties Cu-Mn-Al heusler compounds", Imperial College London, (1970).

3. C. Felser, L. Wollmann, S. Chadov, G. H. Fecher and S. S. P. Parkin, in *Heusler Compounds: Properties, Growth, Applications*, edited by C. Felser and A. Hirohata (Springer International Publishing, Cham, 2016), pp. 37-48.

4. M. Jourdan, J. Minár, J. Braun, A. Kronenberg, S. Chadov, B. Balke, A. Gloskovskii, M. Kolbe, H. J. Elmers, G. Schönhense, H. Ebert, C. Felser and M. Kläui, "Direct observation of half-metallicity in the Heusler compound Co_2MnSi", Nature Communications **5**, (2014).

5. H. Liu, Y. Honda, T. Taira, K. Matsuda, M. Arita, T. Uemura and M. Yamamoto, "Giant tunneling magnetoresistance in epitaxial Co_2MnSi/MgO/Co_2MnSi magnetic tunnel junctions by half-metallicity of Co_2MnSi and coherent tunneling", Applied Physics Letters **101**, 132418 (2012).

6. J. Winterlik, S. Chadov, A. Gupta, V. Alijani, T. Gasi, K. Filsinger, B. Balke, G. H. Fecher, C. A. Jenkins, F. Casper, J. Kübler, G.-D. Liu, L. Gao, S. S. P. Parkin and C. Felser, "Design scheme of new tetragonal heusler compounds for spin-transfer torque applications and its experimental realization", Advanced Materials **24**, 6283-6287 (2012).

7. T. O. Keizo Endo, and Ren'iti Kimura, "Antiferromagnetism of CuMnSb", Journal of the Physical Society of Japan **25**, 907-908 (1968).

8. E. D. Mun, S. L. Bud'ko, C. Martin, H. Kim, M. A. Tanatar, J. H. Park, T. Murphy, G. M. Schmiedeshoff, N. Dilley, R. Prozorov and P. C. Canfield, "Magnetic-field-tuned quantum criticality of the heavy-fermion system YbPtBi", Physical Review B **87**, 075120 (2013).

9. R. A. de Groot, F. M. Mueller, P. G. v. Engen and K. H. J. Buschow, "New class of materials: Half-metallic ferromagnets", Physical Review Letters **50**, 2024-2027 (1983).

10. L. Ritchie, G. Xiao, Y. Ji, T. Y. Chen, C. L. Chien, M. Zhang, J. Chen, Z. Liu, G. Wu and X. X. Zhang, "Magnetic, structural, and transport properties of the Heusler compounds Co_2MnSi and NiMnSb", Physical Review B **68**, 104430 (2003).

11. I. Galanakis and P. H. Dederichs, "Half-metallic compounds : fundamentals and applications". (Springer, Berlin, 2005).

12. M. Meinert, M. P. Geisler, J. Schmalhorst, U. Heinzmann, E. Arenholz, W. Hetaba, M. Stöger-Pollach, A. Hütten and G. Reiss, "Experimental realization of a semiconducting full-Heusler compound: Fe_2TiSi", Physical Review B **90**, 085127 (2014).

13. X.-Q. Chen, R. Podloucky and P. Rogl, "Ab initio prediction of half-metallic properties for the ferromagnetic Heusler compounds Co_2MSi (M=Ti,V,Cr)", Journal of Applied Physics **100**, 113901 (2006).

14. G. H. F. Joachim Barth, Benjamin Balke and Claudia Felser, "Anomalous transport properties of the half-metallic ferromagnets Co_2TiSi, Co_2TiGe and Co_2TiSn", Philosophical Transactions of the Royal Society A **369**, 3588-3601 (2011).

15. S. Ouardi, G. H. Fecher, C. Felser and J. Kübler, "Realization of spin-gapless semiconductors: The heusler compound Mn_2CoAl", Physical Review Letters **110**, 100401 (2013).

16. S. Skaftouros, K. Özdoğan, E. Şaşıoğlu and I. Galanakis, "Search for spin-gapless semiconductors: The case of inverse Heusler compounds", Applied Physics Letters **102**, 022402 (2013).

17. S. Skaftouros, K. Özdoğan, E. Şaşıoğlu and I. Galanakis, "Generalized Slater-Pauling rule for the inverse Heusler compounds", Physical Review B **87**, 024420 (2013).

18. C. Felser, L. Wollmann, S. Chadov, G. H. Fecher and S. S. P. Parkin, "Basics and prospective of magnetic Heusler compounds", APL Materials **3**, 041518 (2015).

19. D. S. Webster and M. J. R. Hoch, "Rotational phase transitions in molecular solids", Journal of Physics and Chemistry of Solids **32**, 2663-2672 (1971).

20. K. R. A. Z. P.J. Webster, . Landolt-Börnstein, "Compounds and Compounds of d-Elements with Main Group

Elements." New Series, Group III ed. (Springer, Berlin, 1988).

21. K. R. A. Ziebeck and P. J. Webster, "A neutron diffraction and magnetization study of Heusler compounds containing Co and Zr, Hf, V or Nb", Journal of Physics and Chemistry of Solids **35**, 1-7 (1974).

22. Y. Takamura, R. Nakane and S. Sugahara, "Analysis of $L2_1$-ordering in full-Heusler Co_2FeSi compound thin films formed by rapid thermal annealing", Journal of Applied Physics **105**, 07B109 (2009).

23. K. Le Dang, P. Veillet and I. A. Campbell, "Hyperfine fields and magnetic interactions in Heusler compounds", Journal of Physics F: Metal Physics **8**, 1811 (1978).

24. C. Jiang, M. Venkatesan and J. M. D. Coey, "Transport and magnetic properties of Mn_2VAl: Search for half-metallicity", Solid State Communications **118**, 513-516 (2001).

25. C. M. Fang, G. A. d. Wijs and R. A. d. Groot, "Spin-polarization in half-metals (invited)", Journal of Applied Physics **91**, 8340-8344 (2002).

26. M. Bowen, A. Barthélémy, M. Bibes, E. Jacquet, J. P. Contour, A. Fert, D. Wortmann and S. Blügel, "Half-metallicity proven using fully spin-polarized tunnelling", Journal of Physics: Condensed Matter **17**, 407 (2005).

27. R. J. Soulen, J. M. Byers, M. S. Osofsky, B. Nadgorny, T. Ambrose, S. F. Cheng, P. R. Broussard, C. T. Tanaka, J. Nowak, J. S. Moodera, A. Barry and J. M. D. Coey, "Measuring the spin polarization of a metal with a superconducting point contact", Science **282**, 85-88 (1998).

28. H. Kato, T. Okuda, Y. Okimoto, Y. Tomioka, K. Oikawa, T. Kamiyama and Y. Tokura, "Structural and electronic properties of the ordered double perovskites A_2MReO_6 (A = Sr, Ca; M = Mg, Sc, Cr, Mn, Fe, Co, Ni, Zn)", Physical Review B **69**, 184412 (2004).

29. D. Ristoiu, J. P. Nozières, C. N. Borca, B. Borca and P. A. Dowben, "Manganese surface segregation in NiMnSb", Applied Physics Letters **76**, 2349-2351 (2000).

30. S. Fujii, S. Sugimura, Ishida and S. Asano, "Hyperfine fields and electronic structures of the Heusler compounds Co_2MnX (X = Al, Ga, Si, Ge, Sn)", Journal of Physics: Condensed Matter **2**, 8583 (1990).

31. B. Balke, S. Wurmehl, G. H. Fecher, C. Felser, M. C. M. Alves, F. Bernardi and J. Morais, "Structural characterization of the Co_2FeZ (Z=Al, Si, Ga, and Ge) Heusler

compounds by x-ray diffraction and extended x-ray absorption fine structure spectroscopy", Applied Physics Letters **90**, 172501 (2007).

32. G. D. Liu, X. F. Dai, H. Y. Liu, J. L. Chen, Y. X. Li, G. Xiao and G. H. Wu, "Mn_2CoZ (Z=Al,Ga,In,Si,Ge,Sn,Sb) compounds: structural, electronic, and magnetic properties", Physical Review B **77**, 014424 (2008).

33. I. Galanakis, K. Özdoğan, E. Şaşıoğlu and S. Blügel, "Conditions for spin-gapless semiconducting behavior in Mn_2CoAl inverse Heusler compound", Journal of Applied Physics **115**, 093908 (2014).

34. L. HongXi, H. Yusuke, M. Kenichi, A. Masashi, U. Tetsuya and Y. Masafumi, "Highly spin-polarized tunneling in epitaxial magnetic tunnel junctions with a Co_2MnSi electrode and a MgO barrier with improved interfacial structural properties", Japanese Journal of Applied Physics **51**, 093004 (2012).

35. S. Kämmerer, A. Thomas, A. Hütten and G. Reiss, "Co_2MnSi Heusler compound as magnetic electrodes in magnetic tunnel junctions", Applied Physics Letters **85**, 79-81 (2004).

36. S. Yuya, N. Jun, O. Mikihiko, K. Hitoshi, A. Yasuo, S. Akimasa and M. Terunobu, "Fabrication of Co_2MnAl heusler compound epitaxial film using cr buffer layer", Japanese Journal of Applied Physics **44**, 6535 (2005).

37. T. Nobuki, I. Naomichi, S. Satoshi and I. Koichiro, "Giant tunnel magnetoresistance at room temperature for junctions using Full-Heusler $Co_2FeAl_{0.5}Si_{0.5}$ electrodes", Japanese Journal of Applied Physics **46**, L454 (2007).

38. H. Ohno, "A window on the future of spintronics", Nature Materials **9**, 952-954 (2010).

39. M. Guo-Xing, M. Markus and S. M. Jagadeesh, "Tunneling path toward spintronics", Reports on Progress in Physics **74**, 036501 (2011).

40. I. M. Tsidilkovski, "Electron spectrum of gapless semiconductors", Springer Series in Solid-State Sciences **116**, (1996).

41. X. L. Wang, "Proposal for a new class of materials: Spin-gapless semiconductors", Physical Review Letters **100**, 156404 (2008).

42. X. Wang, G. Peleckis, C. Zhang, H. Kimura and S. Dou, "Colossal electroresistance and giant magnetoresistance in doped $PbPdO_2$ thin films", Advanced Materials **21**, 2196-2199 (2009).

43. D. H. Kim, J. Hwang, E. Lee, K. J. Lee, S. M. Choo, M. H. Jung, J. Baik, H. J. Shin, B. Kim, K. Kim, B. I. Min and J.-S. Kang, "Valence states and electronic structures of Co and Mn substituted spin-gapless semiconductor $PbPdO_2$", Applied Physics Letters **104**, 022411 (2014).

44. M. E. Jamer, B. A. Assaf, T. Devakul and D. Heiman, "Magnetic and transport properties of Mn_2CoAl oriented films", Applied Physics Letters **103**, 142403 (2013).

45. G. Z. Xu, Y. Du, X. M. Zhang, H. G. Zhang, E. K. Liu, W. H. Wang and G. H. Wu, "Magneto-transport properties of oriented Mn_2CoAl films sputtered on thermally oxidized Si substrates", Applied Physics Letters **104**, 242408 (2014).

46. S. Skaftouros, K. Ozdogan, E. Sasioglu and I. Galanakis, "Search for spin-gapless semiconductors: The case of inverse Heusler compounds", Applied Physics Letters **102**, 4 (2013).

47. L. Bainsla, K. G. Suresh, A. K. Nigam, M. Manivel Raja, B. S. D. C. S. Varaprasad, Y. K. Takahashi and K. Hono, "High spin polarization in CoFeMnGe

equiatomic quaternary Heusler compound", Journal of Applied Physics **116**, 203902 (2014).

48. K. Özdoğan, E. Şaşıoğlu and I. Galanakis, "Slater-Pauling behavior in LiMgPdSn-type multifunctional quaternary Heusler materials: Half-metallicity, spin-gapless and magnetic semiconductors", Journal of Applied Physics **113**, 193903 (2013).

49. G. Z. Xu, E. K. Liu, Y. Du, G. J. Li, G. D. Liu, W. H. Wang and G. H. Wu, "A new spin-gapless semiconductors family: Quaternary Heusler compounds", EPL (Europhysics Letters) **102**, 17007 (2013).

50. P. Kharel, W. Zhang, R. Skomski, S. Valloppilly, Y. Huh, R. Fuglsby, S. Gilbert and D. J. Sellmyer, "Magnetism, electron transport and effect of disorder in CoFeCrAl", Journal of Physics D: Applied Physics **48**, 245002 (2015).

51. L. Bainsla, A. I. Mallick, M. M. Raja, A. K. Nigam, B. S. D. C. S. Varaprasad, Y. K. Takahashi, A. Alam, K. G. Suresh and K. Hono, "Spin-gapless semiconducting behavior in equiatomic quaternary CoFeMnSi Heusler compound", Physical Review B **91**, 104408 (2015).

52. L. Bainsla, A. I. Mallick, A. A. Coelho, A. K. Nigam, B. S. D. C. S. Varaprasad, Y. K. Takahashi, A. Alam, K. G. Suresh and K. Hono, "High spin polarization and spin splitting in equiatomic quaternary CoFeCrAl Heusler compound", Journal of Magnetism and Magnetic Materials **394**, 82-86 (2015).

53. C. Kittel, "Introduction to solid state physics" 6TH ed. (John Wiley & Sons, Inc., , 1986).

54. D. A. Goodings, "Electrical resistivity of ferromagnetic metals at low temperatures", Physical Review **132**, 542-558 (1963).

55. D. Bombor, C. G. F. Blum, O. Volkonskiy, S. Rodan, S. Wurmehl, C. Hess and B. Büchner, "Half-metallic ferromagnetism with unexpectedly small spin splitting in the heusler compound Co_2FeSi", Physical Review Letters **110**, 066601 (2013).

56. P. A. Lee and T. V. Ramakrishnan, "Disordered electronic systems", Reviews of Modern Physics **57**, 287-337 (1985).

57. E. H. Hall, "On a new action of the magnet on electric currents", American Journal of Mathematics **2**, 287-292 (1879).

58. E. M. Pugh, "Hall-effect and the magnetic properties of some ferromagnetic materials", Physical Review **36**, 1503-1511 (1930).

59. R. Karplus and J. M. Luttinger, "Hall-effect in ferromagnetics", Physical Review **95**, 1154-1160 (1954).

60. J. Smit, "The spontaneous Hall-effect in ferromagnetics II", Physica **24**, 39-51 (1958).

61. L. Berger, "Side-jump mechanism for the Hall-effect of ferromagnets", Physical Review B **2**, 4559-4566 (1970).

62. N. Nagaosa, J. Sinova, S. Onoda, A. H. MacDonald and N. P. Ong, "Anomalous Hall-effect", Reviews of Modern Physics **82**, 1539-1592 (2010).

63. W. Thomson, "On the electro-dynamic qualities of metals: Effects of magnetization on the electric conductivity of nickel and of iron", Proceedings of the Royal Society of London A **8**, 546-550 (1857).

64. M. N. Baibich, J. M. Broto, A. Fert, F. N. Van Dau, F. Petroff, P. Etienne, G. Creuzet, A. Friederich and J. Chazelas, "Giant magnetoresistance of (001)Fe/(001)Cr magnetic superlattices", Physical Review Letters **61**, 2472-2475 (1988).

65. N. F. Mott, "Electrons in transition metals", Advances in Physics **13**, 325-422 (1964).

66. M. T. Sarah, "The discovery, development and future of GMR: The Nobel Prize 2007", Journal of Physics D: Applied Physics **41**, 093001 (2008).

67. Y. Sakuraba and K. Takanashi, in *Heusler Compounds: Properties, Growth, Applications*, edited by C. Felser and A. Hirohata (Springer International Publishing, Cham, 2016), pp. 389-400.

68. M. Julliere, "Tunneling between ferromagnetic films", Phys. Lett. A **54**, 225-226 (1975).

69. T. Miyazaki and N. Tezuka, "Giant magnetic tunneling effect in Fe/Al_2O_3/Fe junction", Journal of Magnetism and Magnetic Materials **139**, L231-L234 (1995).

70. Y. T. Evgeny, N. M. Oleg and R. L. Patrick, "Spin-dependent tunnelling in magnetic tunnel junctions", Journal of Physics: Condensed Matter **15**, R109 (2003).

71. S. Ikeda, J. Hayakawa, Y. Ashizawa, Y. M. Lee, K. Miura, H. Hasegawa, M. Tsunoda, F. Matsukura and H. Ohno, "Tunnel magnetoresistance of 604% at 300K by suppression of Ta diffusion in CoFeB / MgO / CoFeB pseudo-spin-valves annealed at high temperature", Applied Physics Letters **93**, 082508 (2008).

72. J.-G. Zhu and C. Park, "Magnetic tunnel junctions", Materials Today **9**, 36-45 (2006).

73. Y. Sakuraba, M. Hattori, M. Oogane, Y. Ando, H. Kato, A. Sakuma, T. Miyazaki and H. Kubota, "Giant tunneling magnetoresistance in Co_2MnSi / Al – O / Co_2MnSi magnetic tunnel junctions", Applied Physics Letters **88**, 192508 (2006).

74. Y. K. Takahashi and K. Hono, in *Heusler Compounds: Properties, Growth, Applications*, edited by C. Felser and A. Hirohata (Springer International Publishing, Cham, 2016), pp. 295-318.

75. K. Kenji, F. Yuichi, Y. Shinya, S. Kentarou, M. Masanobu and H. Kohei, "Greatly enhanced generation efficiency of pure spin currents in Ge using Heusler compound Co_2FeSi electrodes", Applied Physics Express **7**, 033002 (2014).

76. R. Meservey, P. M. Tedrow and P. Fulde, "Magnetic field splitting of the quasiparticle states in superconducting aluminum films", Physical Review Letters **25**, 1270-1272 (1970).

77. W. H. Butler, X. G. Zhang, T. C. Schulthess and J. M. MacLaren, "Spin-dependent tunneling conductance of Fe/MgO/Fe sandwiches", Physical Review B **63**, 054416 (2001).

78. G. J. Strijkers, Y. Ji, F. Y. Yang, C. L. Chien and J. M. Byers, "Andreev reflections at metal/superconductor point contacts: Measurement and analysis", Physical Review B **63**, 104510 (2001).

79. S. A. Wolf, D. D. Awschalom, R. A. Buhrman, J. M. Daughton, S. von Molnár, M. L. Roukes, A. Y. Chtchelkanova and D. M. Treger, "Spintronics: A spin-based electronics vision for the future", Science **294**, 1488-1495 (2001).

80. A. Hirohata, J. Sagar, L. R. Fleet and S. S. P. Parkin, in *Heusler Compounds: Properties, Growth, Applications*, edited by C. Felser and A. Hirohata (Springer International Publishing, Cham, 2016), pp. 219-248.

81. R. Fiederling, M. Keim, G. Reuscher, W. Ossau, G. Schmidt, A. Waag and L. W. Molenkamp, "Injection and detection of a spin-polarized current in a light-emitting diode", Nature **402**, 787-790 (1999).

82. G. Schmidt, D. Ferrand, L. W. Molenkamp, A. T. Filip and B. J. van Wees, "Fundamental obstacle for electrical spin injection from a ferromagnetic metal into a diffusive semiconductor", Physical Review B **62**, R4790-R4793 (2000).

83. P. H. D. I. Galanakis, "Half-Metallic Compounds". (Springer, Berlin, 2005).

84. M. K. A. Hirohata, N. Tezuka, K. Inomata, J.S. Claydon, Y.B. Xu, G. van der Laan, Curr. and Opin., "", Solid State Material Society **10**, 93–107 (2006).

85. M. K. Ho, C. H. Tsang, R. E. Fontana, S. S. Parkin, K. J. Carey, P. Tao, S. MacDonald, P. C. Arnett and J. O. Moore, "Study of magnetic tunnel junction read sensors", IEEE Transactions on Magnetics **37**, 1691-1694 (2001).

86. J.-G. Zhu, "New heights for hard disk drives", Materials Today **6**, 22-31 (2003).

87. M. Andreas, T. Kentaro, T. M. David, A. Manfred, S. Yoshiaki, I. Yoshihiro, S. Shouheng and E. F. Eric, "Magnetic recording: advancing into the future", Journal of Physics D: Applied Physics **35**, R157 (2002).

88. N. D. R. Brad N. Engel, Jason Janesky, Jon M. Slaughter, Renu Dave, Mark DeHerrera, Mark Durlam, "The science and technology of magnetoresistive tunneling memory", IEEE Transactions on Nanotechnology **1**, 32-37 (2002).

89. D. C. Ralph and M. D. Stiles, "Spin transfer torques", Journal of Magnetism and Magnetic Materials **320**, 1190-1216 (2008).

Table of Contents

Chapter 2. Sample Fabrication and Characterization

This Chapter describes sample fabrication (both bulk and thin-film samples), and structural, magnetic and transport properties measurement procedures. Both the experimental tools and analysis methods are described. The Section 2.1 describes the arc-melting and melt-spinning methods to make bulk Heusler compounds and the AJA magnetron sputtering systems used for epitaxial thin-film fabrication. The following Section 2.2 describes the use of x-ray diffraction (XRD) and electron microscopy (SEM and TEM) for structural characterization. The third Section describes the magnetometers and magnetometry measurements used. Section 2.4 covers the electron-transport and Hall -effect measurements and analysis. The final Section 2.4 describes the use of point contact Andreev-reflection (PCAR) methods to detect the spin polarization of materials.

2.1 Sample Fabrication

2.1.1 Arc Melting

Arc melting is used for melting metals– typically to form compounds. Heating is via an electric arc struck between a tungsten electrode and metals placed in a depression (crucible) in the copper hearth. In inert-gas arc melting, the chamber is evacuated and then back filled with argon gas. Hence, melting is performed in an argon atmosphere. A standard Tungsten Inert Gas (TIG) welding unit is used as a power source. Heat generated by the electric arc struck between the electrode and the metals serves to melt

the metals placed in the crucible to form an compound. Repeated melting is performed to improve the homogeneity of the compound. Evacuation of the chamber avoids oxidation of the melt (Ar being an inert gas does not react with molten metal). The metals can be heated to a temperature in excess of 2000 ºC. A batch of four compounds can be made in a single evacuation, as there are four crucibles in the hearth. About 10 g of metal can be melted in the crucibles. There are three main parts to the system: a power source, chiller, and vacuum unit. The vacuum unit with a rotary pump can attain a vacuum of 10^{-2} torr. The cold circulation water from the chiller cools both the copper hearth and the electrodes. After elemental metals (or master compound) are melted and solidified, it can be 'turned over' by a 'tweezer mechanism' without breaking the vacuum (and then re-melted). The melting, solidification, turning over of the sample, the re-melting process is typically repeated three times to attain a better compositional homogeneity. The schematic illustration of a typical arc melting machine is shown in FIG. 2.1.

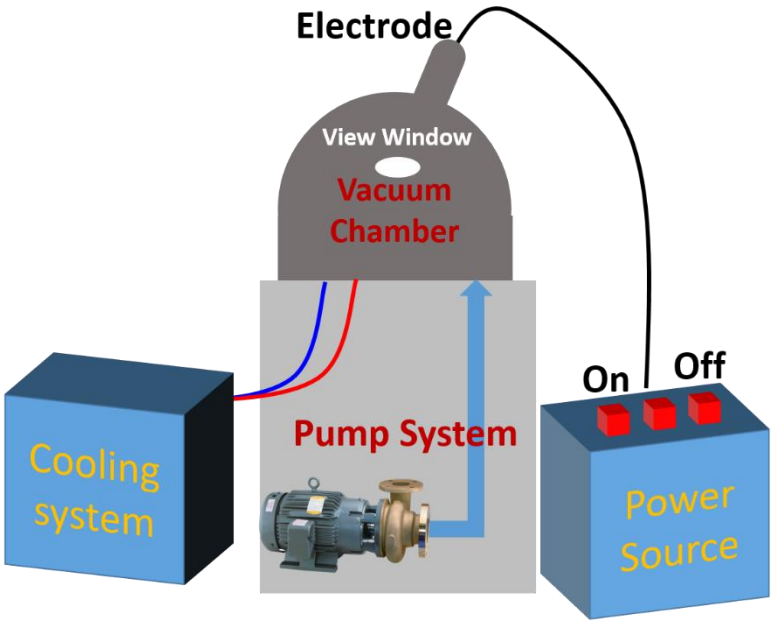

FIG. 2. 1 The schematic illustration of a typical arc melting machine

2.1.2 Melt Spinning

Melt spinning is a technique used for rapid cooling of liquids. A wheel is cooled internally, usually by water or liquid nitrogen, and rotated. A thin stream of liquid is then forced onto the wheel and cooled, causing rapid solidification. This technique is used to develop materials that require extremely high cooling rates in order to form, such as metallic glasses or to capture metastable phases, which could not be obtained by common annealing process.[1-4] The vacuum unit with a combination of rotary pump and diffusion pump can attain a vacuum of 10^{-7} torr. The cooling rates achievable by melt spinning are on the order of 10^4 - 10^7 K/s. A typical melt-spinning system consists of a cooling system, power system, a vacuum chamber with diffusion pump, induction heating with vacuum casting device, spinning wheel with a maximum 50 meter /sec. spinning speed and air quenching system, as shown in FIG. 2.2.

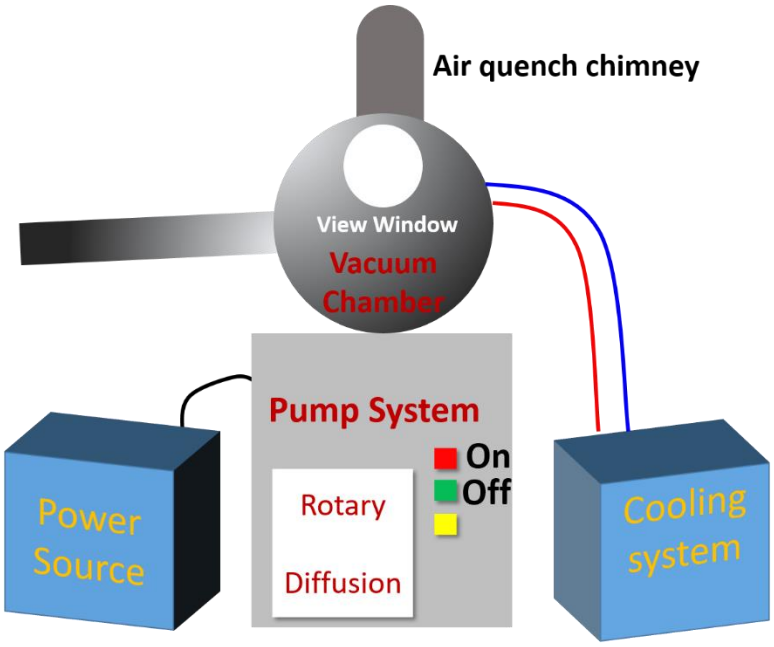

FIG. 2.2 Schematic melt-spinning system.

Melt spinning involves impact under pressure, phase-change and large concentration, velocity, and thermal gradients. In the melt-spinning process, the jet is brought so close to the rotating chill-wheel that it interferes with the molten metal flow on the wheel. Consequently, a molten bridge or “puddle” forms between the nozzle face and the spinning wheel (the “planar” gap), and the metal is spun off as a thin ribbon. The schematic illustration of the principle of melt spinning method is presented in FIG. 2.3. The common crucible is boron nitride or quartz, with a slit nozzle or round nozzle. Melting material from crucible is heated to the ideal temperature and injected through a nozzle onto the chilled spinning wheel. The wheel spinning speed is different for various materials and goals. For obtaining amorphous samples, a higher spinning speed is helpful. For obtaining large grain size, lower spinning speed is preferred. For magnetic materials, the magnetic performance is associated with the grain size of samples. Therefore, it is critical to choose the optimal spinning speed of the chill wheel. The width and thickness of the ribbon samples greatly depend on the size of the nozzle. The large size of the nozzle will cause the increase of the width and thickness of the ribbons.[1, 2] The typical parameters used in this work were 1.5 mm nozzle size of quartz tubes, 24 m/s wheel spinning speed, 35% current of the induction process, respectively.

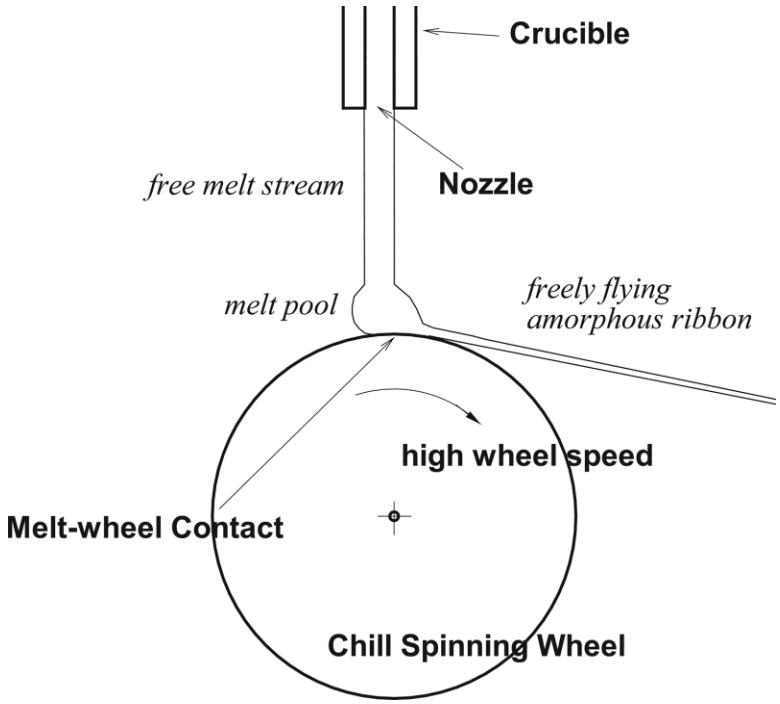

FIG. 2.3 Schematic illustration of the principle of melt spinning.

2.1.3 Magnetron Sputtering

The thin-film fabrication system used in this work is AJA International Magnetron Sputtering System, which has four sputtering guns with two DC and two RF sources. A schematic graph is shown in FIG. 2.4. The sputtering guns are loaded into the bottom in the main chamber and pointed toward to the top center where the substrate is loaded. The tilting angles of these four guns are able to be varied if necessary. The AJA magnetron sputtering system has a main deposition chamber and a sample load-lock.[5] The sample load-lock is to protect the main chamber from frequent exposure to the atmosphere. A combination of turbo pumps and roughing pumps evacuates the chambers. The main chamber can reach a vacuum of 5×10^{-8} Torr. Ar flow-pressure is controllable by the prepared LabVIEW program. The substrate holder height is adjustable along the

central axis of the deposition chamber with the substrate surface facing downward. The rotation of the holder is controllable if necessary at an optimal speed to ensure homogeneous deposition. The system utilizes two tungsten-halogen bulbs to heat the substrate up to about 900 °C. The temperature is controllable and can be tuned to achieve efficient heat ramping. Deposition in the AJA system is operated by a preset LabVIEW program, controlling gas flow-pressure, gun power, substrate temperature, and the position of pneumatic shutters situated over each gun. Typical parameters for substrate height and gun tilt in this work were 30 mm and 5.5 inches.

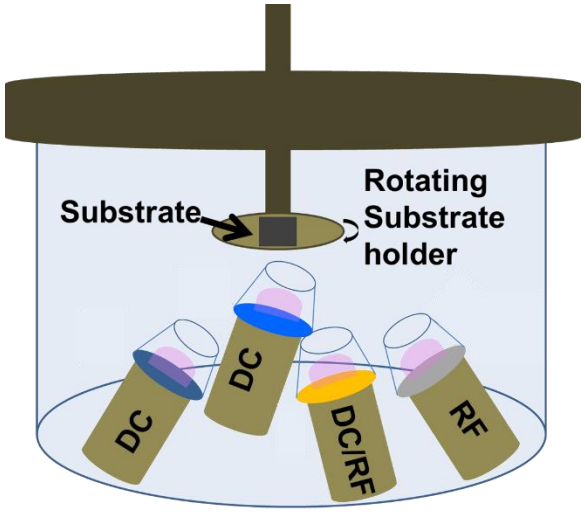

FIG. 2. 4 Schematic graph an AJA sputtering system main chamber.

Sputtering rates were tuned by varying the sputtering power with fixed 2 mTorr Ar flow pressure. Typical deposition powers and corresponding rates of Co, Fe, Cr, Al, Si, Ti, Ge, Mn, Pt, and Sn are shown in Table. 2.1 with the applicable power supply. Deposition rates were calibrated upon any change in power supply for each gun, targets, substrate height, tilting angles of each gun, Ar flow pressure, etc. Rate calibration was determined by depositing a single-layer and measuring the thickness by x-ray reflectivity

(XRR) or atomic force microscopy (AFM). The details of each calibration film depended on the material being calibrated. For example, for Pt calibration of a single-layer film in the range of 10 - 20 nm, XRR showed high-quality total-thicknesses oscillations from the smooth interfaces. FIG 2.5 shows a typical XRR spectra of single calibration film of Pt (10 nm) on SiO_2 substrate. A simulated curve generated by user-input parameters is fitted to the data using a genetic algorithm. The resulting simulation curves are included in the Figure. An *in situ* annealing and/or post-deposition thermal process was required at ambient temperatures in order to achieve the desired phase and film properties. Two tungsten-halogen lamps attached to the substrate holder providing the heat source.

Table. 2.1 Typical deposition powers and corresponding rates of Co, Fe, Cr, Al, Si, Ti, Ge, Mn, Pt, and Sn.

Target	Power Supply	Gun Power (W)	Gun Tilting	Depositing Rate (Å/s)
Co	DC	146	5.5’	0.198
Fe	DC	37.5	5.5’	0.195
Cr	RF	58.2	5.5’	0.198
Al	DC	50	5.5’	0.2738
Si	RF	60	5.5’	0.05
Ti	DC	183	5.5’	0.177
Ge	RF	40	5.5’	0.112
Mn	DC	37.5	5.5’	0.29
Pt	RF	36	5.5’	0.173
Sn	RF	27	5.5’	0.309

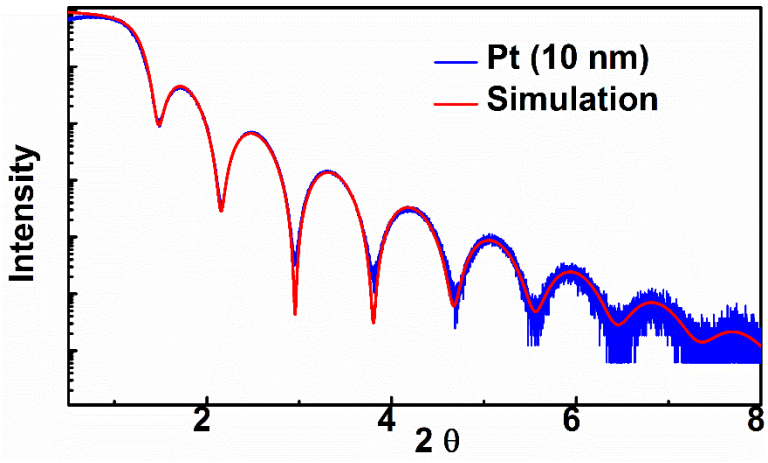

FIG. 2. 5 shows a typical XRR spectra of single calibration film of Pt (10 nm) on SiO_2 substrate.

2.2 Structural Characterization

2.2.1. Transmission-Electron Microscopy (TEM)

Transmission-electron microscopy (TEM) is a microscopy technique in which a beam of electrons is transmitted through a prepared ultra-thin specimen.[6] The TEM operates on the same basic principles as the light microscope but uses electrons instead of light. When an electron beam passes through a thin-section specimen of a material, electrons are scattered. A sophisticated system of electromagnetic lenses focuses the scattered electrons into an image or a diffraction pattern, or a nanoanalytical spectrum, depending on the mode of operation. A magnified and focused image is formed from the interaction of the electrons transmitted through the specimen onto a fluorescent screen, or is detected by a sensor such as a charge-coupled device. TEM imaging is at a significantly higher resolution than light microscopes, which allows examining fine detail, such as a single column of atoms. The very high magnifications follow from complex wave interactions that modulate the intensity of the image, requiring expert analysis of observed images. Briefly, the working principle is that the beam of electrons from the electron gun is focused into a small, thin, coherent beam by the use of the condenser lens. This beam is restricted by the condenser aperture, which excludes high-angle electrons. The beam then strikes the specimen and parts of it are transmitted depending upon the thickness and electron transparency of the specimen. This transmitted portion is focused by the objective lens into an image on phosphor screen or charge coupled device (CCD) camera. The image is then passed down the column through the intermediate and projector lenses, is enlarged along the way. As the electrons pass through the sample, they are scattered by the electrostatic potential set up by the

constituent elements in the specimen. After passing through the specimen they pass through the electromagnetic objective lens which focuses all the electrons scattered from one point of the specimen at one point in the image plane. TEM is capable of observing modulations in chemical identity, crystal orientation, electronic structure, and sample induced electron phase shift as well as the regular absorption based imaging.[7] For example, FIG. 2.6 shows a typical TEM image of Zr_2Co_{11} nanoclusters with an average cluster size of 8.7 nm.[8]

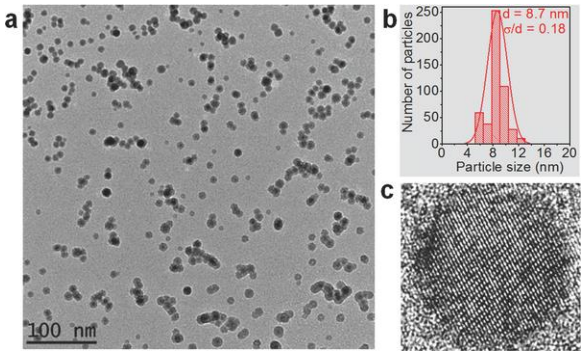

FIG. 2. 6 TEM image of Zr_2Co_{11} nanoclusters with an average cluster size of 8.7 nm.

Specimens have to be thin to use transmitted electrons in the TEM. 'Thin' is a relative term, and for TEM it means electron transparent. For a specimen to be transparent to electrons, it must be thin enough to transmit sufficient electrons such that enough intensity falls on the screen, CCD, or photographic plate to give an interpretable image in a reasonable time. Typically, thinner is better and specimens <100 nm should be used wherever possible. In extreme cases such as doing higher resolution TEM (HRTEM) or electron spectrometry, specimen thicknesses <50 nm (even <10 nm) are essential. In this work, the bulk samples were first polished to a 30-μm-thick thin layer and then further polished by an ion-polishing PIPS/PIPS II machine. Thin-film TEM

samples were even more complicated. Thin-film TEM samples in this work were all prepared for cross-sectional view. Thin films with substrates were first cut into 4 mm × 4 mm square and then bonded together with the thin-film side facing each other. The next step was to polish the cross Section side of this bonded sample to a 30-μm-thick thin layer followed by ion-polishing PIPS/PIPS II machine. The TEM equipment in this dissertation is a FEI Tecnai Osiris (S) TEM with fully digital 200 kV TEM and STEM system including the HAADF detector, X-FEG high-brightness Schottky FEG, Super-X windowless EDX detector, and EELS system.

2.2.2. Selected-Area Electron Diffraction (SAED)

Selected-area electron diffraction (SAED) is a crystallographic experimental technique performed inside a TEM.[6] In a TEM, a specimen is subjected to a beam of high-energy electrons of about 100 - 400 keV, so that the electrons pass through the sample easily. In this case, electrons are treated as a wave. The spacing between atoms in a solid is about a hundred times larger than the wavelength of electrons, and the atoms act as a diffraction grating to the electrons. Due to the diffraction, electrons will be scattered to particular angles. The angles are determined by the crystal structure of the sample. Consequently, the diffraction image shown on the screen of the TEM is called a selected-area diffraction pattern. For the single crystal, the pattern is periodic spots. Each spot corresponds to a satisfied diffraction condition of the sample's crystal structure. If the sample is tilted, the same crystal will stay under illumination, but different diffraction conditions will be activated, and different diffraction spots will appear or disappear. SAED patterns are a projection of the reciprocal lattice, with lattice reflections showing as sharp diffraction spots. By tilting a crystalline sample to low-index zone axes, SAED

patterns can be used to identify crystal structures and measure lattice parameters. Besides, users can choose the different area and areal size for diffraction by choosing different size of apertures. Located below the sample holder on the TEM column is a selected-area aperture, which can be inserted into the beam path. The aperture is a thin strip of metal which contains the different size of holes. The aperture is to block all of the electron beams except for a small part of the beam which passes through the selected hole. In this way, the particular area is selected by the aperture. This is important in polycrystalline specimens with more than one phase. If different phase and different crystals contribute to the SAED patterns, it can be difficult or impossible to analyze. Thus, it is useful to select a single crystal for structural analysis. It may also be useful to select two crystals, in order to examine the crystallographic orientation between them. Generally, SAED is used to identify crystal structures and examine crystal defects, which is similar to X-ray diffraction. The difference is that SAED is for the very small area of several hundred nanometers in size and XRD is macro-analysis. On the other hand, single spots appear only when the beam is diffracted by a single crystal. Polycrystalline materials have crystals with different orientations. SAED for this material gives ring patterns analogous to those from X-ray powder diffraction and can be used to identify texture and discriminate nanocrystalline from amorphous phases.[7] As an example, FIG. 2.7 shows SAED spot patterns of (a) FCC Co phase, and (b) Hf_2Co_7 phase, polycrystalline SAED rings of FePt clusters.[9, 10]

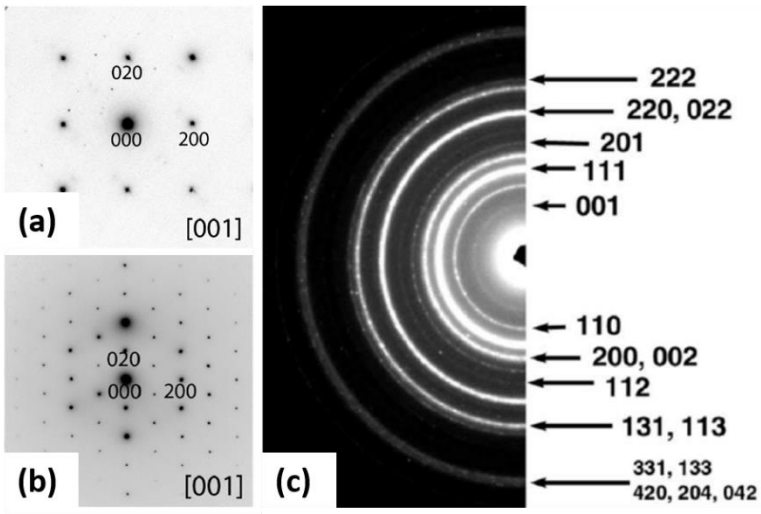

FIG. 2. 7 SAED spot patterns of (a) FCC Co phase, and (b) Hf_2Co_7 phase, polycrystalline SAED rings of FePt clusters.[9, 10]

2.2.3. High-Resolution TEM (HRTEM)

High-Resolution TEM (HRTEM) is an advanced mode of TEM and the ultimate tool in imaging defects.[6] It can show directly a two-dimensional projection of the crystal with defects and other characteristics. However, HRTEM only makes sense if the two-dimensional projection is under some low-index direction, so atoms are exactly on top of each other. For example, [100], [001], [010], and [110]. The basic principle involved in the image formation in both TEM and HRTEM is similar. However, HRTEM provides high-resolution images at atomic scale level. HRTEM uses both the transmitted and the scattered beams to produce an interference image, which is a phase contrast image and can be as small as a column of atoms. In this case, the outgoing modulated electron waves at very low angles interfere with itself during propagation through the objective lens. All electrons emerging from the specimen are combined at a point in the image plane. There are some important features involved in HRTEM. First, the specimen should

be tilted so that a low-index direction is exactly perpendicular to the electron beam. All lattice planes about parallel to the electron beam will be close enough to the Bragg position and will diffract the primary beam. Second, the diffraction pattern is the Fourier Transform of the periodic potential for the electrons in two dimensions. In the objective lens, all diffracted beams and the primary beam are brought together again; their interference provides a back-transformation and leads to an enlarged picture of the periodic potential.[7] One example of HRTEM of [001] axis of Zr_2Co_{11} is shown in FIG. 2.8.[8]

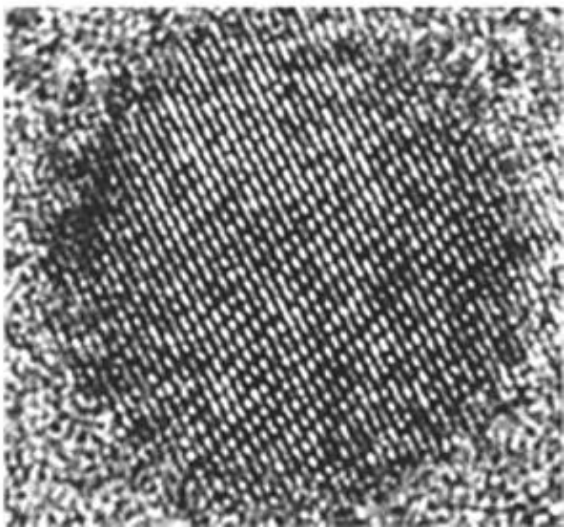

FIG. 2. 8 HRTEM of [001] axis of Zr_2Co_{11}.[8]

2.2.4. Scanning TEM (STEM)

Scanning transmission-electron microscopy (STEM) is a type of TEM. In STEM, the electron beam is focused to a fine spot which is then scanned over the sample in a raster.[6] The rastering of the beam across the sample makes STEM suitable for analytical techniques such as Z-contrast annular dark-field imaging, and spectroscopic mapping by

energy dispersive X-ray (EDX) spectroscopy, or electron energy-loss spectroscopy (EELS). It obtains these signals simultaneously and directly correlates images and spectroscopic data. In EDX, an X-ray spectrometer is used to detect the characteristic X-rays that are emitted by atoms in the sample as they are ionized by an electron in the beam. In STEM, EDX is typically used for compositional analysis and elemental mapping of samples.[7] For example, FIG. 2.9 shows (a) a STEM HAADF image of $HfCo_7$ and elemental mapping of Hf, Co, HfCo, respectively. (b) line scan of a nano $HfCo_7$ particle. It shows clearly that the nanocluster is a $HfCo_7$ phase and the cluster size. By the elemental mapping and line scan, it is also possible to obtain the stoichiometry composition information for the nanocluster.[11]

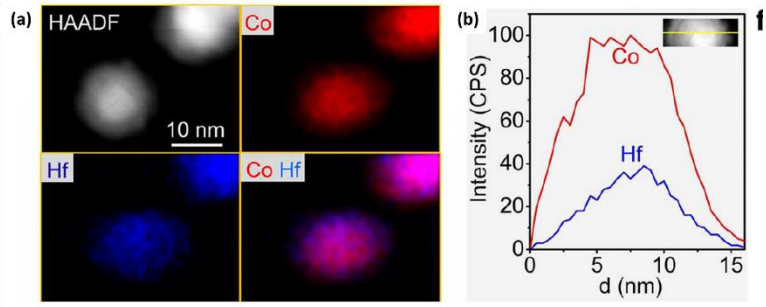

FIG. 2. 9 (a) STEM HAADF image of $HfCo_7$ and elemental mapping of Hf, Co, HfCo, respectively. (b) Line scan of a nano $HfCo_7$ particle.[11]

2.2.5. X-Ray Diffraction (XRD)

X-ray powder diffraction (XRD) is a rapid analytical technique primarily used for phase identification of a crystalline material and can provide information on unit cell dimensions. The analyzed material is finely ground, homogenized, and average bulk composition is determined. The diffraction is based on Bragg diffraction, which occurs

when radiation, with a wavelength comparable to atomic spacings, is scattered in a specular fashion by the atoms of a crystalline system and undergoes constructive interference. For a crystalline solid, the waves are scattered from lattice planes separated by the interplanar distance *d*. When the scattered waves interfere constructively, they remain in phase since the difference between the path lengths of the two waves is equal to an integer multiple of the wavelength. The path difference between two waves undergoing interference is given by $2d\sin\theta$, where θ is the scattering angle, as shown in FIG. 2.10.[5]

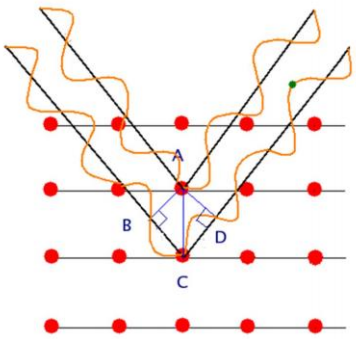

FIG. 2. 10 schematic illustration of Bragg scattering.

The effect of the constructive or destructive interference intensifies because of the cumulative effect of reflection in successive crystallographic planes of the crystalline lattice (as described by Miller notation). This leads to Bragg's law,

$$2d_{hkl}sin(\theta) = n\lambda \qquad [2.1]$$

Where *h, k, l*, are Miller indices, *n* is a positive integer and λ is the wavelength of the incident wave. Note that moving particles, including electrons, protons, and neutrons, have an associated wavelength called *de Broglie* wavelength. A diffraction pattern is

obtained by measuring the intensity of scattered waves as a function of scattering angle. Very strong intensities known as Bragg peaks are obtained in the diffraction pattern at the points where the scattering angles satisfy the Bragg condition. Diffraction peaks are associated with planes of atoms and Miller indices (hkl) are used to identify different planes of atoms. A single-crystal specimen in a diffractometer would produce only one family of peaks in the diffraction pattern. The powder x-ray diffractometers used for structural characterization in this dissertation is PANalytical Empyrean - Linear Detector and Non-ambient Environment. PANalytical Empyrean uses a sealed-tube generator with operating voltage of 40 – 45 kV max. and operating current of 20 – 40 mA max. Copper anodes, i.e. Cu Kα1 have a wavelength of 1.54056 Å. Beam masks have the size of 5, 10 and 15 mm. Programmable divergent slit can be adjusted from 0.5 to 20 mm and it also has fixed from 1/32 to 2°. Antiscatter slits are from 1/16 to 4°.

X-ray reflectivity (XRR) measurements of a thin-film sample reveal the perpendicular distances between diffracting interfaces within the film. Interference between reflections from the film-free and the film substrate interfaces produces intensity variations i.e. Kiessig fringes.[5] The position, θ_m, of the m^{th} order peak of the Kiessig fringes, relates to a film's critical angle, α_c and total thickness, d has the relations as:

$$\theta_m^2 - \alpha_c^2 = m^2 \left(\frac{\lambda}{2d}\right)^2 \qquad [2.2]$$

In a typical XRR pattern, surface and interface roughnesses dampen the intensities. A comparison of XRR scattering and modeling of the system can quantify the roughness of a film's interfaces. XRR measurements were used to calibrate deposition rates by analyzing the period of Kiessig fringes to determine layer thicknesses of

specially designed calibration films. FIG. 2.4 shows an example of typical XRR spectra and simulation. The XRR measurement is performed with a Rigaku SmartLab Diffractometer in this dissertation. This machine has a dedicated arm for detector movement in-plane and perpendicular to the sample surface, thereby on ablng one to probe structure in both directions without tilting the sample. The instrument is equipped with a cross-beam optics device that will allow switching between focussing (BB) and the parallel beam (PB) geometries easily. SmartLab guidance software helps the automated optics and sample alignment and prepares optimum scan conditions. The diffractometer uses Cu Kα radiation (wavelength of about 1.54 Å). SmartLab is configured not only for grazing-incidence in-plane XRD, but also for texture (pole Figures) in this dissertation.

Crystal texture can be quantified with x-ray diffraction by a number of different techniques. One way is to collect spectra with a two-dimensional detector and create pole Figures, from which a sample's texture coefficients can be determined. The pole Figure is the stereographic projection of the poles used to represent the orientation of an object in space. A pole Figure (in the context of texture) is a map of a selected set of crystal plane normals plotted with respect to the sample frame.[12] The rows (not columns) in the orientation matrix define the coordinates of each crystal axis with respect to the sample frame. This definition refers to plane normals because of the standard use of x-ray diffraction to measure pole Figures. Since each plane normal is plotted by itself, there is no information in the resulting plot about directions lying in that plane. Pole Figures represent a projection of the texture information. Each chosen crystal direction is generally specified as a low-index plane normal, e.g. [100], [110]. Crystal symmetry is

generally assumed to apply such that all equivalent plane normals sharing the same Miller indices are shown. For cubic materials, obviously, plane normals and directions are coincident but this is not the case for lower symmetry Bravais lattices. Since unit vectors representing directions with respect to a common origin live on a sphere, it is natural to transform the coordinates to spherical angles such as azimuth (longitude) and declination (co-latitude). This makes it clear that, for each crystallite, its three orientation parameters (e.g. Euler angles) are reduced (projected) to only two parameters. Only the upper hemisphere is plotted, by convention. The resulting diagram is often called a stereogram. If only a few distinct orientations are displayed, multiple poles can be plotted on the same diagram as a discrete pole Figure. When many crystallites are included in the dataset, which has variable orientation, it is impracticable to have more than one pole. Also, it is necessary to bin the data and convert points to densities. For display purposes, contour plots are the easiest way to understand the result. For example, FIG. 2.11 shows the goniometer is set for [100] reflections, then all directions in the sample that are parallel to <100> directions will exhibit diffraction.

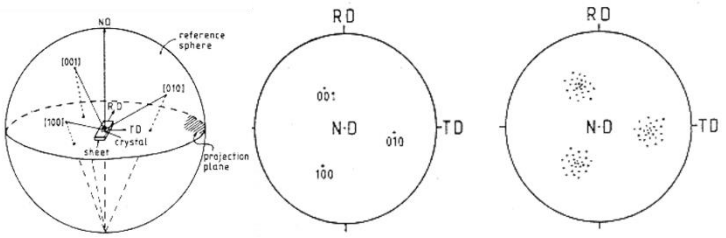

FIG. 2. 11 Example of a cubic crystal pole Figures of [100] reflections.

2.3 Magnetic Characterization

2.3.1. Physical Property Measurement System (PPMS)

The Quantum Design Physical Property Measurement System (PPMS) represents an open-architecture, variable temperature-field system that is optimized to perform a variety of automated measurements. It has many modes for a variety of material properties characterization. In this dissertation, the vibrating-sample magnetometer mode and AC Transport mode are used. I will briefly introduce these two modes.

The magnetic properties of the samples were measured using the vibrating-sample magnetometer (VSM). The VSM is based on Faraday's law which states that an *emf* will be generated in a coil when there is a change in flux linking the coil. The temperature dependence of magnetic properties of the samples was measured using the VSM mode. If a sample of any material is placed in a uniform magnetic field, a dipole moment will be induced. If the sample vibrates with sinusoidal motion a sinusoidal electrical signal can be induced in suitably placed pick-up coils. The signal has the same frequency of vibration and its amplitude will be proportional to the magnetic moment, displacement amplitude, and relative position with respect to the pick-up coils system. This device covers two sample temperature ranges from 2 K to 400 K and from 300 K to 1000 K. For measurements in the low-temperature range the sample is glued to a quartz holder free of paramagnetic impurities. For measurements in the high-temperature range, a ceramic holder with embedded heating wires is used. The sample is fixed on this holder by a piece of copper foil wrapped around sample and holder. Measurements in the low-temperature range are conducted in a He atmosphere at a pressure of approximately 10 mbar. For

measurements in the high temperature range, the pressure is decreased below 10^{-3} mbar in order to avoid oxidation or other reactions with residual gases. For thin-film samples, the film and substrate are cut into a small size 6 mm x 6 mm and attached to a quartz sample holder. For high-temperature measurement, zirc-cement was used to seal the sample onto a special holder which could bear the high temperature. The sample is attached to the end of a sample rod that is driven sinusoidally. The center of oscillation is positioned at the vertical center of a gradiometer pickup coil. The precise position and amplitude of oscillation are controlled by the VSM motor module using an optical linear encoder signal read back from the VSM linear-motor transport. The voltage induced in the pickup coil is amplified and lock-in detected in the VSM detection module. The VSM detection module uses the position encoder signal as a reference for the synchronous detection. This encoder signal is obtained from the VSM motor module, which interprets the raw encoder signals from the VSM linear motor transport. The VSM detection module detects the in-phase and quadrature-phase signals from the encoder and from the amplified voltage from the pickup coil. These signals are averaged and sent to the VSM application running on the PC.[13 5]

The PPMS AC transport mode offers angular-dependent electron-transport measurements, including resistivity and Hall-effect. The AC Transport measurement system (ACT) option is a precision current source and a voltage detector. It works at the current range: 10 mA to 2 A, provides a sensitivity: 1 nV @ 1 kHz and frequency range: 1 Hz to 1 kHz. The PPMS sample-mounting system is straightforward; at the bottom of the sample chamber is a 12-pin connector pre-wired to the system electronics. This connector enable pluging in a removable sample insert or sample “puck” and offers

convenient access to electrical leads for application hardware and electronics. This connector provides the foundation for all of the PPMS measurement inserts. FIG. 2.12 shows the schematic architecture of a PPMS probe and a plane view of the puck for ACT mode. The puck can measure two samples at the same time and the angle between the film plane and the magnetic field could be tilted from 0° to 360°.

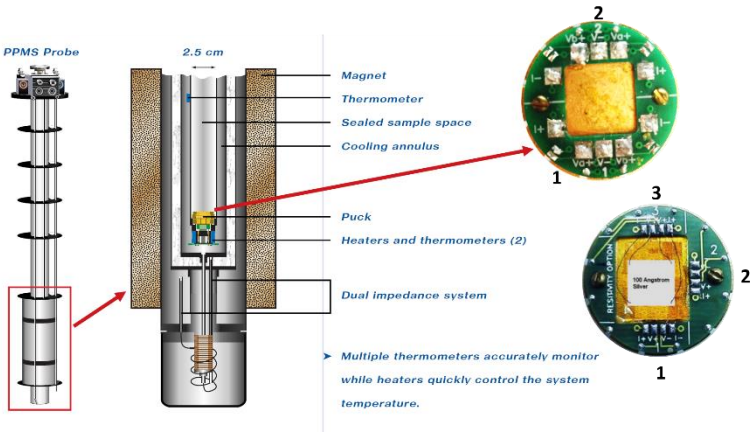

FIG. 2. 12 Architecture of a PPMS probe and a plane view of the puck for ACT mode.

2.3.2 Superconducting Quantum Interference Device Magnetometer (SQUID)

A Superconducting Quantum Interference Device (SQUID) uses the properties of electron-pair wave coherence and Josephson Junctions to detect very small magnetic fields. A ring of superconducting material with one or more weak links is the most important element of a SQUID. FIG. 2.13 shows an example of a weak link at points W and X whose critical current, i_c, is much less than the critical current of the main ring. This produces a very low current density making the momentum of the electron-pairs small. The wavelength of the electron-pairs is thus very long leading to a small difference in phase between any parts of the ring. If a magnetic field, is applied perpendicular to the

plane of the weak links, a phase difference is produced in the electron-pair wave. A small current is also induced to flow around the ring, producing a phase difference across the weak links. Normally the induced current would be of sufficient magnitude to cancel the flux in the hole of the ring but the critical current of the weak-links prevents this. The quantum condition that the phase change around the closed path must equal $n2\pi$ can still be met by large phase differences across the weak-links produced by even a small current. Detecting this circulating current in the weak links enables the use of a SQUID as a magnetometer. The SQUID magnetometer used in this work is the MPMS XL SQUID magnetometer from Quantum Design, which can employ superconducting coils to generate applied fields up to 70 kOe. The system contains the dewar, probe and SQUID assembly, and the electronic control system. The probe system is modular allowing the addition of extra component options such as the reciprocating sample option (RSO). The probe contains a high-precision temperature-control system, allowing measurements between 1.9 K and 400 K with an accuracy of 0.01 K. The dewar consists of an inner liquid-helium reservoir and outer liquid-nitrogen jacket, to reduce excessive liquid-helium boil-off. The liquid helium is used both for maintaining the electromagnet in a superconducting state and for cooling the sample space. Samples are mounted within a plastic straw and connected to one end of a sample rod which is inserted into the dewar/probe. The other end is attached to a stepper motor which is used to position the sample within the center of the SQUID pickup coils. The pickup coils are conFigured as highly balanced second-derivative coils. The coils reject the applied field from the superconducting magnet to a resolution of 0.1 %. Unlike DC measurements where the sample is moved through the coils in discrete steps, the RSO measurements are

performed using a servo motor which rapidly oscillates the sample. A shaft encoder on the servo motor records the position of the sample synchronous with the SQUID signal. The data received is fitted to an ideal dipole moment response. In this dissertation, RSO measurement with Center scans was used.[5, 14]

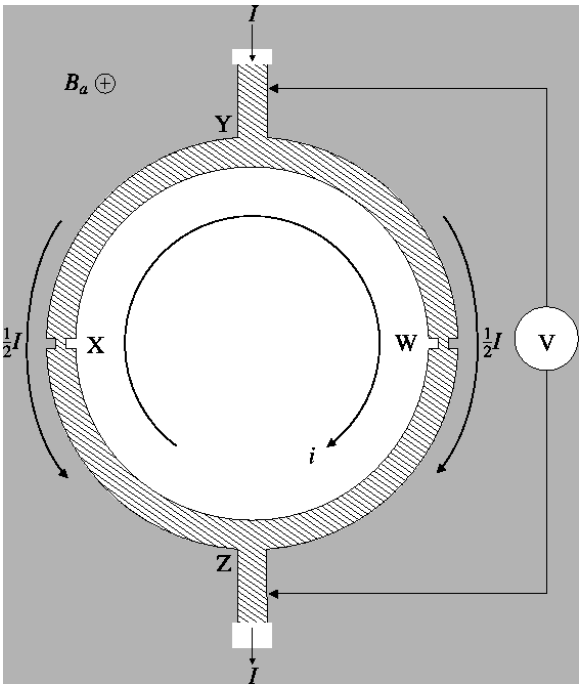

FIG. 2. 13 Superconducting quantum interference device (SQUID) as a simple magnetometer.

2.4 Electron-Transport and Hall-Effect Measurements

The Hall-Effect measurement is a useful technique for determining the accurate carrier density and the mobility of carriers in semiconductors and metals. As mentioned in Section 1.6 and 1.7, collisions of electrons in a metal cause the resistivity. Impurity scattering and electron-phonon scattering are the two most common processes in metals. Defects change the periodic lattice of ions which leads to electron scattering, and gives a

temperature-independent contribution to the resistivity. The history of the Hall-effect begins in 1879 when Edwin H. Hall discovered that a small transverse voltage appeared across a current-carrying thin metal strip in an applied magnetic field.[15] In this dissertation, the longitudinal and Hall resistivity were measured by a standard four-point-probe Hall-effect measurement methods.[16] A schematic view of the resistivity measurement using a narrow sample and by arranging the four-point-contact on a line along the strip axis is displayed in FIG. 2.14. The advantage of the four-probe technique is that it largely eliminates contact resistance.[13]

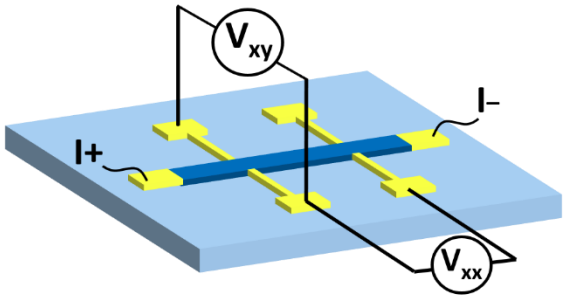

FIG. 2. 14 A schematic view of the resistivity measurement.

By applying a current I^+I^- across the film, the resistance is measured by detecting the longitudinal and transversal voltages V_{xx} and V_{xy} as shown in FIG. 2.14 through separate contacts. For a good electrical contact and homogeneous current distribution across the ends of the thin film, gold contact pads were used. The nano-patterned sample shown in FIG. 2.15 is prepared by AJA magnetron sputtering with two different types of the patterned mask for two steps. The mask I is patterned with a rectangular hole in the center. The size could be adjusted depending on the experimental requirements. In this dissertation, the length is 4400 μm and width is 400 μm. Mask I, which is mounted on the substrate (Si or MgO), is used in the first step for film deposition. The second step

used mask II for gold contact deposition in AJA. Mask II has a different pattern, which is designed for standard Hall-effect measurement. The schematic illustration of the two steps is shown in FIG. 2.15.

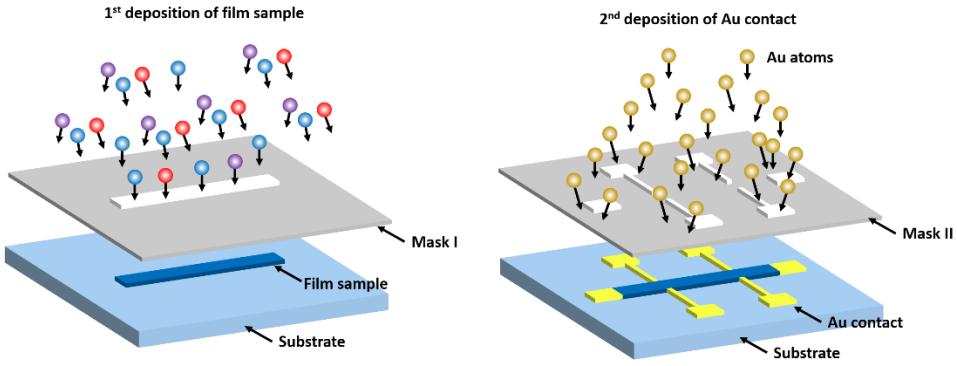

FIG. 2. 15 The schematic illustration of the two steps.

For a thin film with length *l*, width *w*, and thickness *d*, the resistivity ρ of the film is given as:

$$\rho = \frac{dw}{l} R \qquad [2.3]$$

And the MR ratio is calculated by:

$$MR(100\%) = \frac{\rho_H - \rho_0}{\rho_0} * 100\% \qquad [2.4]$$

For temperature dependence of resistivity of the sample, the resistivity is measured with varying temperature from 5 K to 300 K (or 350 K). For resistivity versus magnetic field at a specific temperature, the sample was measured with magnetic field is perpendicular to the film plane and varying from – 7 T to 7 T. The resistivity for various temperature and magnetic field is measured in a Quantum Design, Physical Property Measurement System (PPMS) with AC and/or DC resistivity mode.

2.5 Point Contact Andreev Reflection Measurements

Point Contact Andreev Reflection (PCAR) measurements are one useful method to measure spin polarization of materials especially HM and SGS Heusler compounds. This utilizes the Andreev reflection that occurs at a point contact between a normal conductor and a superconductor.[17] De Jong and Beenakker proposed the principle to measure spin polarization using Andreev reflection in 1995.[18] Subsequnetly, Soulen *et al*. reported the first experimental results of spin polarization measurement using the point contact Andreev reflection method.[19] This measurement should be operated at a low temperature of about 1.8 K so that cryogenic cooling is necessary for measurements. FIG. 2.16 (a) shows a schematic illustration of the density of states (DOS) of a non-magnetic metal (NM) and a superconductor (SC). Electrons can flow from NM to SC by forming Cooper pairs of spin-up and spin-down electrons when the energy of the incident electrons is smaller than the superconducting band gap 2Δ. In the normal conductor with no polarization of spins ($P = 0$), i.e. the number of spin-up and spin-down electrons are the same at E_F. In this case, the Cooper pairs are formed and thus the conductance is enhanced to double within the superconducting gap (FIG. 2.16 (c)). Andreev reflection holes are reflected the normal conductor owing to the momentum conservation in the system.

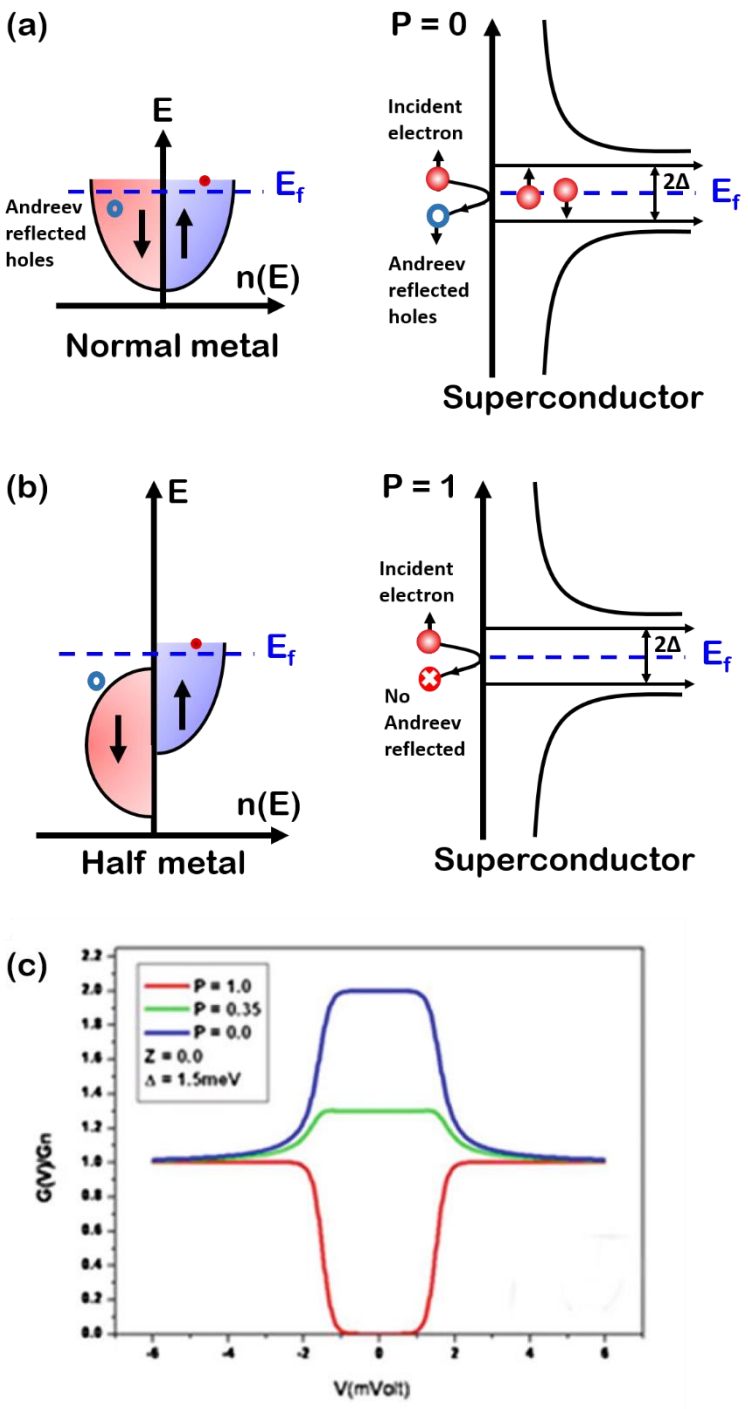

FIG. 2. 16 Schematic images of Andreev reflections with point contact of (a) normal conductor and superconductor and (b) half-metal and superconductor. (c) Calculated conductance curves with different spin polarization.[17]

However, in a half-metallic ferromagnetic magnet, the Andreev reflection is somewhat suppressed due to the different DOS of spin-up and spin-down. For half-metals, the electrons are 100% spin-polarized, i.e. electrons at E_F only have one spin direction, there is no electron to form a Cooper pair (FIG. 2.16 (b)), so the conductance in the superconducting gap is completely suppressed (FIG. 2.16 (c)). Therefore, the conductance curves vary depending on the spin polarization of the material. The spin polarization is deduced by fitting the conductance curve to the modified Blonder-Tinkham-Klapwijk model (BTK) under the assumption that the electron scattering occurs due to the surface oxidation.[20] In a PCAR measurement, the temperature should be lower than the critical temperature of Nb, 9.2 K and electro-polished sharp Nb tips with a point contact of several 10 nm are required, which is shorter than the mean free path of electrons. However, the typical contact resistance was ~20 Ω in real measurement, corresponding to a diameter of about 28 nm, larger than the mean free path of electrons. The conductance is through multiple diffusive contacts and the transport spin polarization measured by PCAR is formulated as

$$P_{PCAR} = \frac{\langle Nv_F^2\rangle\uparrow - \langle Nv_F^2\rangle\downarrow}{\langle Nv_F^2\rangle\uparrow + \langle Nv_F^2\rangle\downarrow}, \qquad [2.5]$$

where N is the DOS and v_F^2 is the Fermi velocity. The real experimental electrical circuit is as shown in FIG. 2.17. The current was measured by the lock-in technique.[17]

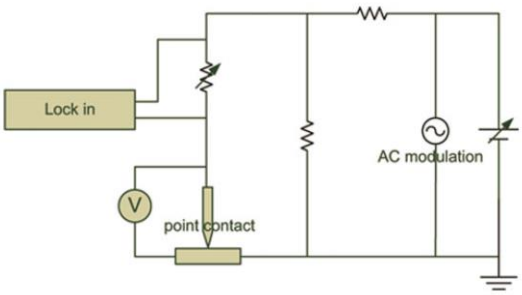

FIG. 2. 17 Schematic illustration of the electric circuit in PCAR measurement.[17]

2.6 Bibliography

1. Y. Jin, W. Y. Zhang, R. Skomski, S. Valloppilly, J. E. Shield and D. J. Sellmyer, "Phase composition and nanostructure of Zr_2Co_{11}-based compounds", Journal of Applied Physics **115**, (2014).

2. Y. Jin, X. Fan, H. Men, X. Liu and B. Shen, "FePCCu nanocrystalline compounds with excellent soft magnetic properties", Sci. China Technol. Sci. **55**, 3419-3424 (2012).

3. I. A, "New amorphous Mg-Ce-Ni compounds with high strength and good ductility", Journal of Applied Physics, 2248-2251 (1988).

4. K. K. Inoue A, Zhang T, *et al.*, "Amorphous $La_{55}A_{125}Ni_{20}$ compound prepared by water quenching", Materials Transaction. JIM, 722-725 (1989).

5. T. A. George, "Magnetic Anisotropy and Exchange in (001) Textured Fept-Based Nanostructures", University of Nebraska Lincoln, (2013).

6. D. B. Williams and C. B. Carter, "Transmission Electron Microscopy: Textbook for Materials Science" 2nd ed. (Springer, New York, 2009).

7. P. B. Hirsch, "Electron microscopy of thin crystals". (Butterworths, London, 1965).

8. B. Balasubramanian, B. Das, R. Skomski, W. Y. Zhang and D. J. Sellmyer, "Novel Nanostructured Rare-Earth-Free Magnetic Materials with High Energy Products", Advanced Materials **25**, 6090-6093 (2013).

9. M. Daniil, P. A. Farber, H. Okumura, G. C. Hadjipanayis and D. Weller, "FePt/BN granular films for high-density recording media", Journal of Magnetism and Magnetic Materials **246**, 297-302 (2002).

10. X. Li, Y. Jin, M. Wang, J. E. Shield, R. Skomski and D. J. Sellmyer, "Electron diffraction study of cobalt-rich Hf-Co", Intermetallics **75**, 54-61 (2016).

11. B. Balasubramanian, P. Mukherjee, R. Skomski, P. Manchanda, B. Das and D. J. Sellmyer, "Magnetic nanostructuring and overcoming Brown's paradox to realize extraordinary high-temperature energy products", Scitific Report **4**, (2014).

12. A. D. Rollett, "Introduction to X-ray Pole Figures", http://pajarito.materials.cmu.edu/rollett/27750/L4-Xray_PFs-22Jan14.pptx., (2014).

13. M. Z. Obaida, "Magnetoresistance and Anomalous Hall-effect of Cu_2MnAl, Co_2MnSi and Co_2MnGe Heusler compound thin films", Ruhr-University Bochum, (2011).

14. J. Bland, "A Mössbauer Spectroscopy and Magnetometry Study of Magnetic Multilayers and Oxides", University of Liverpool, (2002).

15. E. H. Hall, "On a new action of the magnet on electric currents", American Journal of Mathematics **2**, 287-292 (1879).

16. J. Sagar, "Optimisation of Heusler Compound Thin Films for Spintronic Devices", The University of York, (2013).

17. Y. K. Takahashi and K. Hono, in *Heusler Compounds: Properties, Growth, Applications*, edited by C. Felser and A. Hirohata (Springer International Publishing, Cham, 2016), pp. 295-318.

18. M. J. M. de Jong and C. W. J. Beenakker, "Andreev Reflection in Ferromagnet-Superconductor Junctions", Physical Review Letters **74**, 1657-1660 (1995).

19. R. J. Soulen, J. M. Byers, M. S. Osofsky, B. Nadgorny, T. Ambrose, S. F. Cheng, P. R. Broussard, C. T. Tanaka, J. Nowak, J. S. Moodera, A. Barry and J. M. D. Coey,

"Measuring the spin polarization of a metal with a superconducting point contact", Science **282**, 85-88 (1998).

20. G. J. Strijkers, Y. Ji, F. Y. Yang, C. L. Chien and J. M. Byers, "Andreev reflections at metal/superconductor point contacts: Measurement and analysis", Physical Review B **63**, 104510 (2001).

Table of Contents

Chapter 3. Half-Metallicity in Highly $L2_1$-Ordered CoFeCrAl Thin Films

In this chapter, structural, magnetic, and electron-transport properties of Heusler-ordered CoFeCrAl thin films (both polycrystalline and epitaxial films) are investigated. The films, sputtered onto MgO and Si substrates, have thicknesses of about 100 nm. The epitaxial CoFeCrAl films on MgO substrate exhibit virtually perfect single-crystalline epitaxy and a high degree of $L2_1$ chemical order. X-ray diffraction and transmission electron microscopy show that the structure of the films is essentially of the $L2_1$ Heusler type. The films are ferrimagnetic, with a Curie temperature of about 390 K and a net moment of 2 μ_B per formula unit. The room temperature resistivity is 175 μΩcm; the carrier concentration and mobility determined from the low temperature (5 K) measurement are 1.2×10^{18} cm^{-3} and 33 cm^2/Vs, respectively. In contrast to well-investigated Heusler compounds such as $Co_2(Cr_{1-x}Fe_x)Al$, the CoFeCrAl system exhibits two main types of weak residual A2 disorder, namely Co-Cr disorder and Fe-Cr disorder, the latter conserving half-metallicity. Point-contact Andreev reflection yields a lower bound for the spin polarization, 68% at 1.85 K, but our structural and magnetization analyses suggest that the spin polarization at the Fermi level is probably higher than 90%. CoFeCrAl films grown on SiO_2 substrates have a saturation magnetization of 2.5 μ_B/f.u. at 5 K and Curie temperature of about 550 K. The electron-transport measurements on the films revealed a negative temperature coefficient of resistivity, large anomalous Hall conductivity and linear field dependence of magnetoresistance. The carrier concentration and mobility to be 1.3×10^{18} cm^{-3}, 21.46 $cm^2/(V\cdot s)$ at 10 K, respectively, are comparable to the reported bulk value. The compound is, ideally, a spin-gapless semiconductor, but structural disorder destroys the spin-gapless character and drastically alters the transport

behavior. These two types of CoFeCrAl films were grown by magnetron sputtering deposition at 973 K, namely polycrystalline films on Si substrates and epitaxial films on MgO (001) substrates. The resistivity decreases with increasing temperature, with relatively small temperature coefficients of –0.19 μΩcm/K for the polycrystalline films and –0.12 μΩcm/K for the epitaxial films. The residual resistivity of the polycrystalline films deposited on Si is higher than that of the epitaxial film deposited on MgO, indicating that the polycrystalline films behave as so-called dirty metals.

Many of the results presented in this chapter are adapted from the publications:

1. Y. Jin, P. Kharel, S. R. Valloppilly, X.-Z. Li, D. R. Kim, G. J. Zhao, T. Y. Chen, R. Choudhary, A. Kashyap, R. Skomski and D. J. Sellmyer, "Half-metallicity in highly L21-ordered CoFeCrAl thin films". *Applied Physics Letters* 109, 142410 (2016).

2. Y. Jin, R. Skomski, P. Kharel, S. Valloppilly, and D. J. Sellmyer, "Effect of Disorder on the Resistivity of CoFeCrAl Films". *AIP Advances* 7, 055834 (2017).

I performed the synthesis and characterization of the CoFeCrAl Films. R. Skomski and R. Choudhary helped with the theoretical explanations. and P. Kharel and S. R. Valloppilly contributed revising the manuscripts. D. R. Kim, G. J. Zhao and T. Y. Chen performed the PCAR measurements. All co-authors contributed to the final manuscript.

3.1 Introduction

Exotic spin-electronics materials have recently attracted much attention because they are scientifically interesting and technologically important. Examples are half-metallic compounds, graphene-like structures, and—more recently—spin-gapless

semiconductors. The unique band structure of spin-gapless semiconductors (SGS), which exhibit a nonzero Fermi-level gap in one spin channel and a zero gap in the other one, leads to several favorable properties. They combine the advantages of half-metallic magnets[1, 2] and zero-gap semiconductors and[3], are voltage-tunable and generally have high spin polarization at the Fermi level, have the ability to switch between spin-polarized n- and p-type conduction, and have carrier mobilities much higher than those of classical semiconductors[3-10]. Furthermore, some SGS have nearly compensated ferrimagnetic spin structures with small net magnetization, which produce no harmful magnetic stray fields in nanoelectronic devices[11]. Heusler compounds play an important role in the search for half-metals and spin-gapless semiconductors[7, 12-14]. A few of them are realized experimentally[5, 6, 8, 10], and some, such as Co_2MnSi and Co_2(Cr, Fe)Al, have already been implemented in magnetic tunnel junctions, with high tunneling magnetoresistances of 1995% at 4.2 K and 354% at 300 K in Co_2MnSi[15].

CoFeCrAl is a particularly intriguing material for structural and physical reasons. Perfectly ordered CoFeCrAl, which has been predicted to be a spin-gapless semiconductor[7, 13, 16], crystallizes in the cubic Heusler-type Y structure (prototype LiMgPdSn). This structure is a CsCl (B2) derivative and has the composition XX'YZ, where the X and X' atoms occupy one B2 sublattice in an alternating NaCl-type order, whereas the Y and Z atoms do the same for the other B2 sublattice. An impressive spin polarization of 67% has been measured even in partially disordered bulk samples.[17] However, practical devices require high-quality thin films, because some types of disorder destroy half-metallicity by forming additional states in the minority spin gap.[16,

[18] Key requirements are epitaxial film growth, to ensure single-crystallinity rather than polycrystallinity, and a sufficiently high degree of chemical order.

The Y-structured CoFeCrAl is prone to various types of chemical disorder. Co (X) and Fe (X') are expected to interchange very easily,[16] so that X = X' and the material becomes a Heusler-type $L2_1$ compound of composition X_2YZ (prototype Cu_2MnAl). The corresponding structure is that of the well-investigated compound Co_2CrAl, except that half of the Co atoms are randomly replaced by Fe. Another type of B2 chemical disorder is Cr-Al disorder, where Y and Z atoms interchange positions (FIG. 3.1). This disorder is not limited to CoFeCrAl but also affects the related $Co_2Cr_{1-x}Fe_xAl$ system, where it is crucial for the understanding of spin-polarization effects[19, 20]. The $Co_2Cr_{1-x}Fe_xAl$ series includes the end members Co_2CrAl (x = 0) and Co_2FeAl (x = 1), and is, therefore different from CoFeCrAl structurally and electronically, although there are parallels as far as the B2-type Cr-Al disorder is concerned.

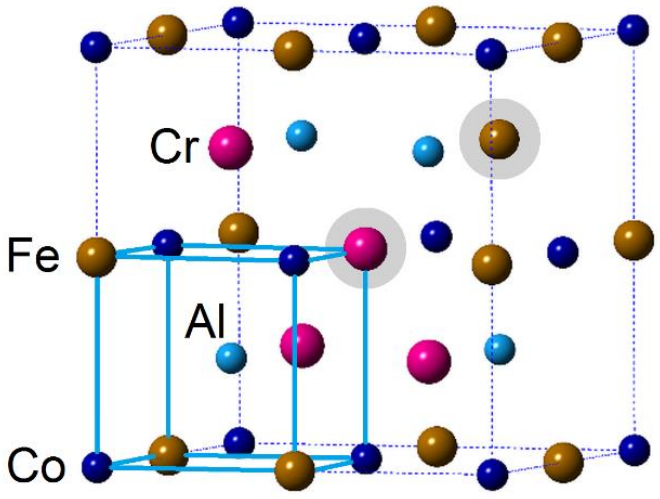

FIG. 3. 1 Structure of and defects in CoFeCrAl. The Figure shows Fe-Cr disorder as one example of the A2 disorder.

The third type is A2 (bcc) disorder, where all atoms (X, X', Y and Z) are randomly distributed in a bcc unit cell. The effect of A2 disorder on spin-electronic properties is devastating. As we will analyze below, B2 type Fe-Co disorder destroys the SGS behavior of Y-ordered CoFeCrAl but conserves half-metallicity. In $Co_2Cr_{1-x}Fe_xAl$, B2-type Cr-Al and Fe-Cr disorders also largely conserve half-metallicity.[19-22] CoFeCrAl is qualitatively different from $Co_2Cr_{1-x}Fe_xAl$ because, in the former, both Co-Cr and Fe-Cr disorders are of the more severe A2 type. The question, therefore, arises about the harmfulness of the two A2 disorder contributions.

Experimentally, CoFeCrAl compounds prepared by arc-melting or rapid quenching and subsequent annealing[10, 17] exhibit substantial degrees of B2 (CsCl) and A2 (bcc) disorder. Using the 2 × 2 × 2 unit cell of the $L2_1$ and Y structures, which contains 8 formula units, the most dominant A2 x-ray diffraction (XRD) peaks are (220), (400), and (422). B2 order leads to a pronounced (200) peak, whereas $L2_1$ and Y orders create a characteristic (111) peak. The (111) peak is normally barely visible[10], indicating incomplete Heusler ordering.

Pronounced chemical disorder leads to dirty-metal behavior, characterized by resistivities of the order of 200 μΩcm and observed, for example, in Ti-Al, Nb_3Sn, and Ni-Cr-Al.[23-27] Spin-gapless semiconductivity and dirty-metal mechanism are difficult to distinguish experimentally, because high resistivities are also expected for SGS and because both dirty metals (i.e. highly disordered metals) and SGS can exhibit negative temperature coefficients of the resistivity (TCR), as contrasted to the positive TCR of ordinary metals. Ideal SGS have the infinite residual resistivity at zero temperature ('freeze-out regime'), due to the absence of carriers at the Fermi level, but thermal

excitations are very effective in creating carriers because the gap width is zero. This causes a negative TCR. Weak chemical disorder in SGS is likely to create some carriers even at zero temperature so that the residual resistivity is finite but large.[10] The high residual resistivity of dirty metals and their negative TCR have very different origins. They are linked to the electrons' mean free path becoming comparable to the interatomic distance so that the electrons are no longer described by well-defined *k*-vectors.[27]

The unusual magnetoresistance (MR) effect, linear in a magnetic field and positive,[28] varies greatly among spin-gapless semiconductors and is only partially understood. MR values of 150% are observed in Co-doped $PbPdO_2$,[4, 29] but much smaller values of 9% and 0.6% have been reported for bulk and thin film Mn_2CoAl, respectively,[5, 6, 8] and the magnetoresistance of bulk CoFeCrAl is about 1.5%.[17] The difference reflects the electronic structure of the materials: a magnetic field changes the direction of the Co spins in the doped $PbPdO_2$, which is a very effective magnetoresistive mechanism, whereas the MR in the Heusler requires an electron transfer from the minority spin channel to the majority spin channel, which is energetically rather unfavorable.

While both SGS and dirty metals have similar resistivities and TCRs, and the magnetoresistance is not very telling, the two classes of materials can be distinguished by considering the residual resistivity as a function of the chemical disorder. FIG. 3.2 outlines the idea. If one has samples with different degrees of chemical order, for example, due to different processing parameters or substrate, then a distinction between SGS and dirty metals may be possible. In the SGS regime, the residual resistivity decreases with increasing disorder, because the disorder creates carriers. In dirty metals,

the residual resistivity *increases* with the disorder, because the disorder is the very origin of the resistivity.

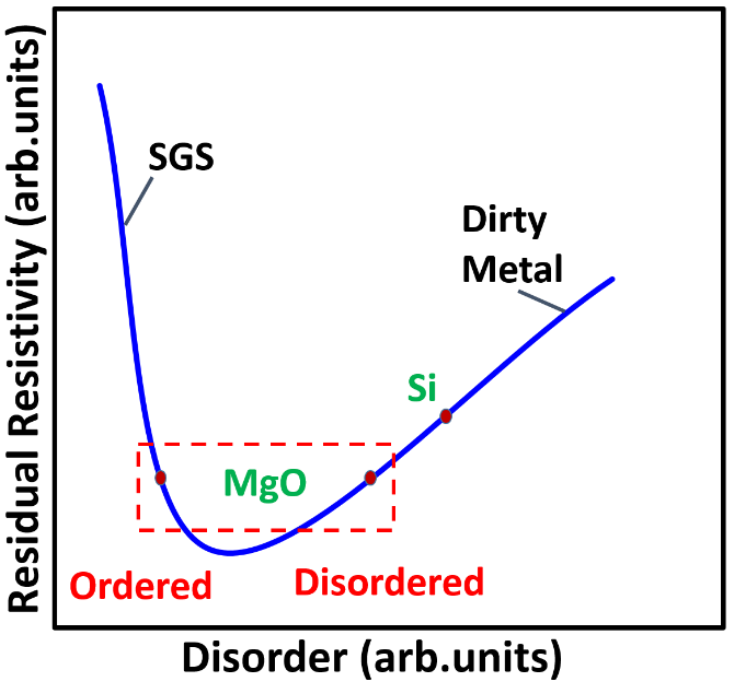

FIG. 3. 2 Residual resistivity as a function of disorder (schematic). "MgO" and "Si" refer to CoFeCrAl films on MgO and Si substrates, respectively.

Here we consider thin films of CoFeCrAl, a material that has been predicted to be an SGS in its fully ordered Y structure.[13, 16] In this chapter, the degree of order can be controlled by the choice of substrate: films deposited on MgO are much better ordered than films on Si.

3.2 Experimental Details

A magnetron sputtering system with a base pressure of about 3×10^{-8} Torr was used to deposit CoFeCrAl thin films onto atomically flat C-cut MgO (001) and Si substrates. The samples were co-deposited from Co, Fe, Cr and Al targets under optimized deposition conditions. A stoichiometry very close to CoFeCrAl is achieved at 973 K and DC powers of 40 W and 42 W for Al and Fe targets, and RF powers of 69 W and 33 W for Cr and Co targets, respectively. Ar pressure is 2×10^{-3} Torr. Lower deposition temperatures yield polycrystalline CoFeCrAl films on MgO, whereas temperatures above 600 K do not affect the film growth on Si. The crystal structure and the epitaxy of the films were investigated by in-plane and out-of-plane XRD diffraction, by pole-Figure experiments using a Rigaku SmartLab Diffractometer with Cu Kα radiation (wavelength 1.54 Å), by electron diffraction using the FEI Nova NanoSEM450 Scanning Electron Microscope (SEM), and using an FEI Tecnai Osiris (Scanning) Transmission Electron Microscope (TEM). The elemental compositions of the films were determined using the energy-dispersive x-ray spectroscopy (EDX) in the SEM and TEM. The typical thickness of the films, as determined by the Bruker Dimension Icon® Atomic Force Microscope and TEM, is 100 nm. The magnetic and electron transport properties were measured using a Quantum Design SQUID magnetometer (MPMS) and a physical property measurement system (PPMS). The degree of transport spin-polarization was determined by point-contact Andreev reflection (PCAR).

3.3 Structural Properties

FIG. 3.3 shows the out-of-plane XRD patterns of CoFeCrAl films onto (a) Si, (b) MgO (001) substrates. First, the films grown on Si are polycrystalline but textured, with a preferential (220) orientation. This orientation is inferred from the strong (220) peak and the absence of (200) and (400) peaks in FIG. 3.3 (b). Second, the films grown on the MgO substrate exhibit an epitaxial growth of the (001) type, as evidenced by the exclusive presence of only the (002) and (004) peaks in FIG. 3.3 (b), indicating that the films are grown with a high degree of orientation with respect to the cube axes of MgO.

Due to the epitaxial character of the films, the degree of Heusler (L21 or Y) order cannot be judged from FIG. 3.3. This question is important because CoFeCrAl is likely to exhibit various degrees of A2 (bcc), B2 (CsCl), and $L2_1$ (normal cubic Heusler) disorder.[10, 16, 17] These types of disorder affect and potentially destroy SGS behavior and, in the case of A2 disorder, even half-metallicity.[4] To establish Heusler order, it is necessary to trace XRD peaks such as the (111) peak, and this peak has indeed been found after milling the films.

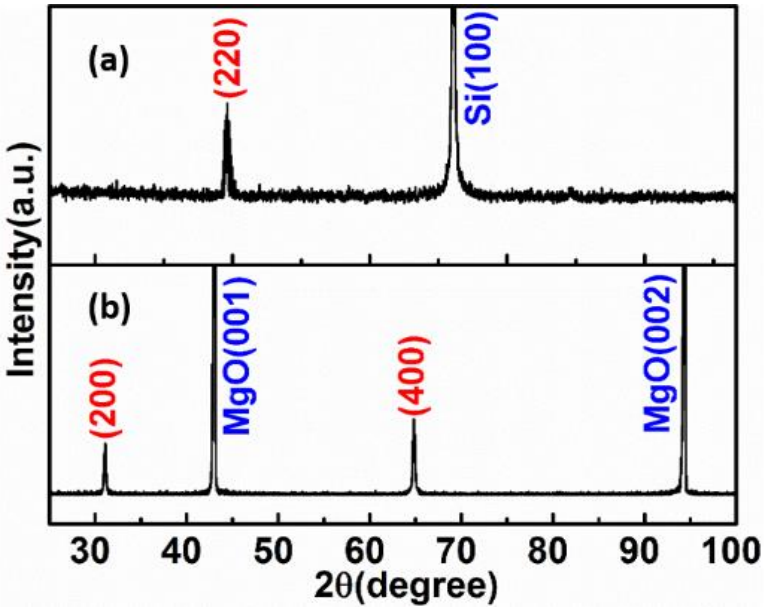

FIG. 3. 3 Out-of-plane XRD patterns of CoFeCrAl on (a) on Si and (b) on MgO (001).

FIG. 3.4 shows intensity profiles extracted for (111), (002), (004) and (220) peaks with an appropriate tilt of the sample (χ degrees), with respect to the surface normal. The order parameters for the CoFeCrAl film were evaluated using the extended Webster model[21]. The respective degrees of Cr-Al B2 order (A2 disorder) and $L2_1$ order (B2 disorder) can be calculated from the long-range order parameters

$$S_{B2}^2 = I_{200} \cdot I_{400}^f / I_{400} \cdot I_{200}^f \qquad [3.1]$$

$$(S_{L21}(3 - S_{B2})/2)^2 = I_{111} \cdot I_{220}^f / I_{220} \cdot I_{111}^f, \qquad [3.2]$$

where I_{hkl} and I_{hkl}^f are the experimental diffraction intensity for the (hkl) plane and its reference intensity calculated for fully ordered compounds. In our samples, S_{L21} and S_{B2} are both equal to 88% with an uncertainty of about 5%. This indicates a high degree of Heusler-type chemical order, in addition to the nearly perfect crystalline orientation. The

Fe-Co B2 order parameter, which enables the distinction between $L2_1$ and Y structures, could not be determined due to almost identical scattering contrast for Fe and Co for X-rays, but the system probably exhibits a large degree of Fe-Co solid-solution disorder.

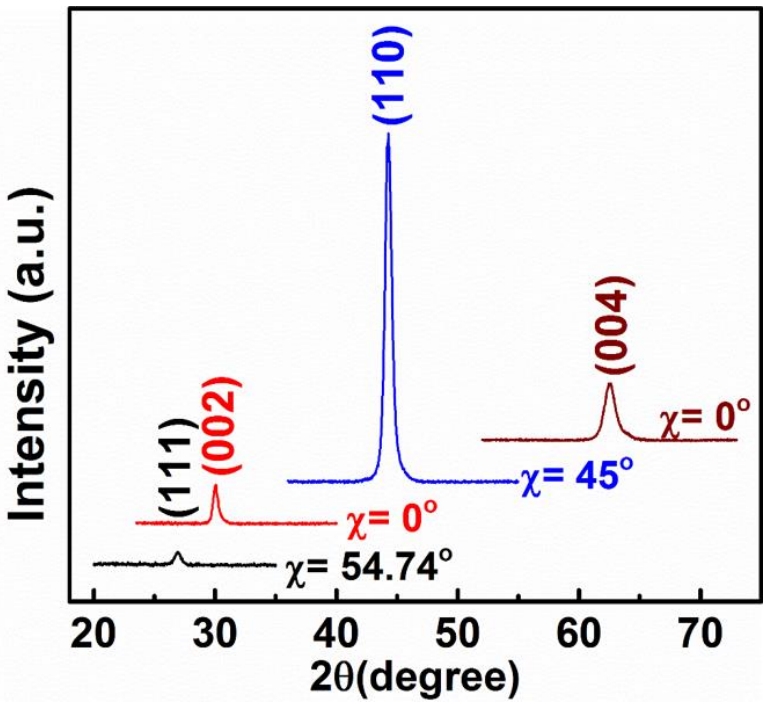

FIG. 3. 4 Intensity profiles extracted for (111), (002), (004) and (220) peaks extracted with a beam of about 0.5 mm and the area detector. The sample was tilted with respect to the surface normal // (001) by 54.74° for the (111) plane and by 45° for the (220) plane.

FIG. 3.5 show the pole-Figure plots for the [111] and [220] planes relative to the (100) plane of MgO, respectively. These plots confirm the high degree of epitaxial crystallinity of the film deposited on MgO and establish the orientation relationship between the crystallographic axes in the film plane. The pole-plot intensities have

maxima at two angles, namely 0° and at 45°, and both exhibit 4-fold symmetry, providing clear evidence that the CoFeCrAl films grown on MgO are single-crystalline with the cubic crystal structure. Moreover, the azimuthal angles mean that MgO [100] and CoFeCrAl [220] are parallel and that CoFeCrAl [100] is rotated by 45° away from MgO [100]. This situation is similar to the epitaxial growth of Fe film on MgO, where the rotation of the over layer unit cell by 45° favors epitaxial growth.[23] The lattice parameter of CoFeCrAl, about 5.74 Å, is 1.36 times that of MgO (4.21 Å) and close to the "ideal" ratio $\sqrt{2}$ = 1.41. The experimental ratio indicates that the lattice spacing d_{110} (MgO) corresponds to a_{100} (CoFeCrAl), with a small in-plane strain of about 3.6%.

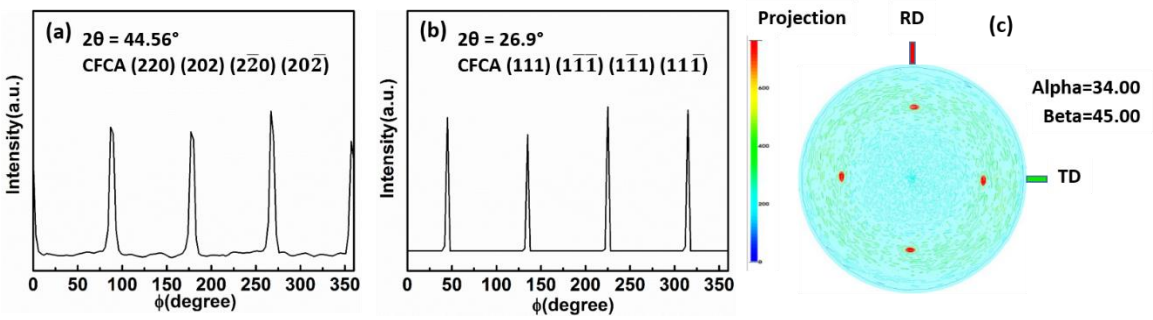

FIG. 3. 5 Pole-Figure plots of CoFeCrAl deposited on MgO (001): (a) ϕ scan for (220) diffraction (2θ = 44.56°) and (b) ϕ scan for (111) diffraction (2θ = 26.9°), and (c) The [110] pole-Figure shows the epitaxy and four-fold in-plane symmetry of the films.

FIG. 3.6 shows the selected area electron diffraction (SAED) pattern of a specimen prepared from the CoFeCrAl film on MgO substrate. The SAED is along the MgO [100] zone axis, which corresponds to the CoFeCrAl [110] direction, and the

diffraction spots from MgO and CoFeCrAl are marked with red and white colors, respectively. The presence of the (111) superlattice diffraction spot in the SAED pattern confirms the presence of a Heusler superstructure. FIG. 3.6 (b) shows a high-resolution TEM image of the interface between the CoFeCrAl film and MgO substrate. The image confirms the epitaxial growth of the CoFeCrAl film on the MgO, with a small lattice mismatch. The lattice constant a = 5.74 Å determined from the lattice fringe spacing of the high-resolution TEM image of FIG. 3.6 (c) agrees with the analysis of the XRD pattern. As shown in the STEM image with elemental mapping of FIG. 3.6 (c) and 3.6 (d), the film growth is uniform and the films are about 100 nm thick.

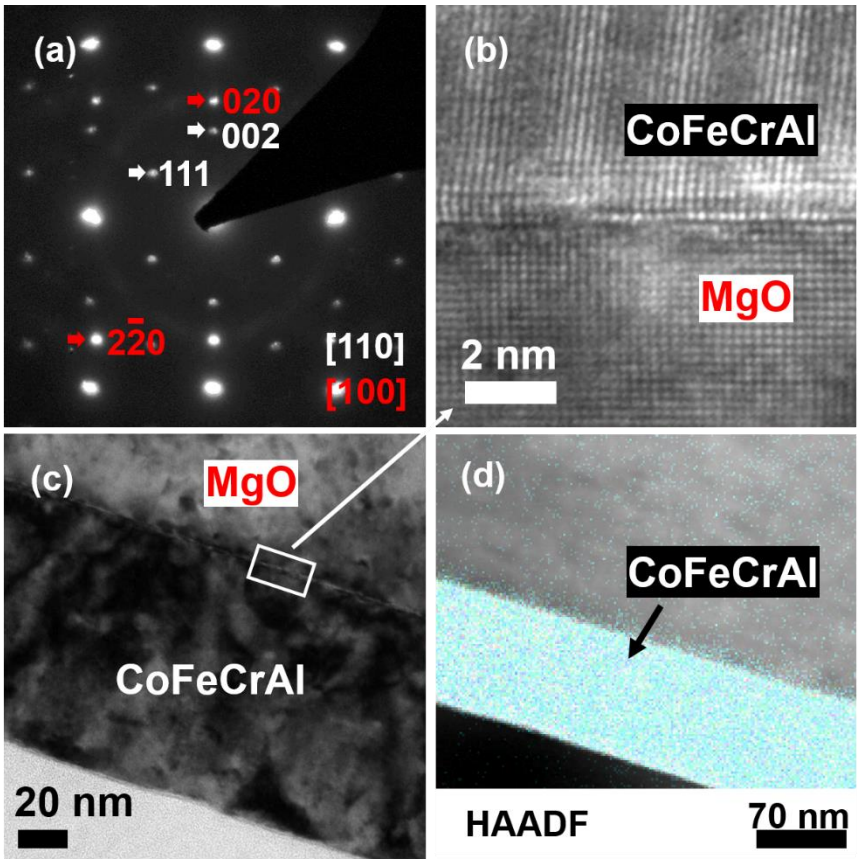

FIG. 3. 6 Structure of CoFeCrAl on MgO: (a) SAED pattern, (b) high-resolution TEM image of the interface between film and substrate, (c) STEM image, and (d) high-angle

annular dark-field (HAADF) and element-mapping images. Red and white colors indicate MgO and CoFeCrAl, respectively.

Our structural analysis shows that the CoFeCrAl grows epitaxially on MgO, with a common *c*-axis perpendicular to the plane and an angle of 45º between the *a*-axes of CoFeCrAl and MgO. The atomic structure is essential of the Heusler type, very likely $L2_1$, with some degree of B2-type Cr-Al and A2 disorder. Alternatively, we can interpret the structure as a Y-ordered compound with substantial B2-type Fe-Co disorder, some B2-type Cr-Al disorder, and some A2 disorder.

To investigate the structure of CoFeCrAl on Si, we have used Rietveld analysis of a film ground into powder. FIG. 3.7 shows the room-temperature XRD pattern. The weak peaks in the pattern marked with star sign are from silicon impurity, where the silicon particles were scraped off from the substrate surface with the sample. The CoFeCrAl pattern contains the fundamental bcc peaks and the (100) super-lattice peak, which indicates that the films exhibit B2-type structural disorder. The lattice constant and density of B2-type polycrystalline CoFeCrAl film deduced from the Rietveld analysis of XRD pattern are 2.875 Å and 6.971 g/cm^3, respectively. SAED patterns conducted on this CoFeCrAl polycrystalline film on Si substrate is shown in FIG. 3.8. The rings pattern of SAED confirmed a B2-type structural disorder and a lattice constant of 2.87 Å was deduced from this pattern.

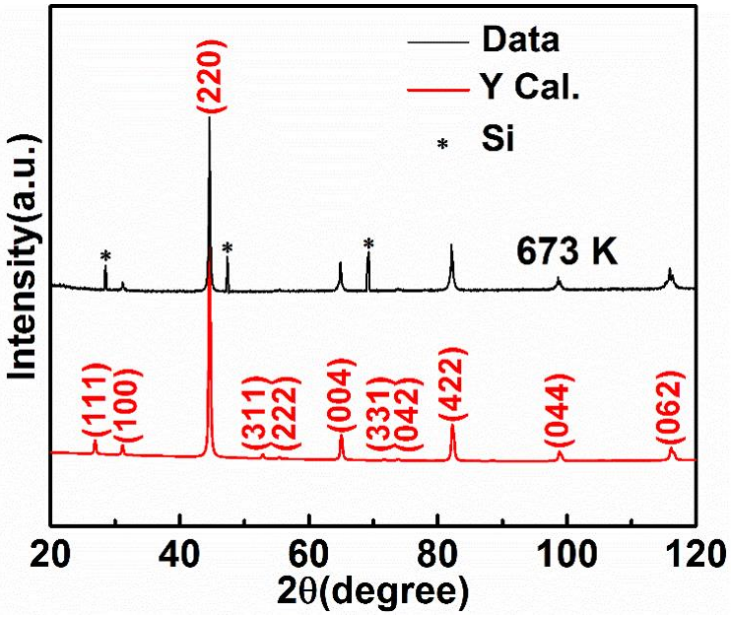

FIG. 3. 7 XRD pattern and Rietveld analysis of powder sample prepared by grinding the 1000-nm-thick film.

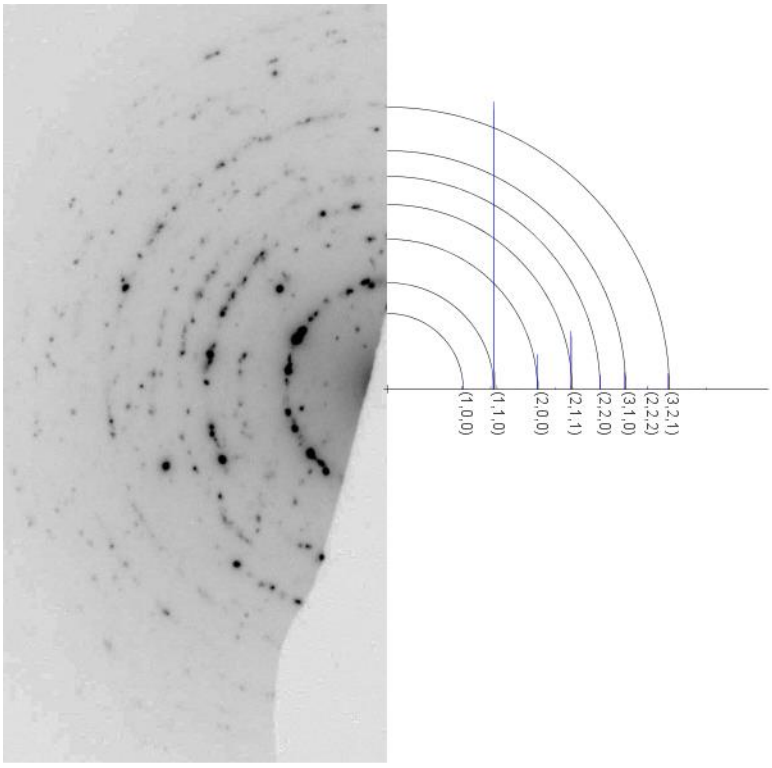

FIG. 3. 8 SAED pattern of CoFeCrAl polycrystalline film on Si substrate.

3.4 Magnetic Properties

The magnetization of the films of CoFeCrAl on MgO substrate is 2.0 ± 0.1 μB per formula unit, as expected for ferrimagnetic CoFeCrAl, and the films are magnetically soft, with coercivities of 50 Oe (in-plane) and 150 Oe (perpendicular) at 5 K, as shown in FIG. 3.9. The Curie temperature of the films is about 390 K, somewhat smaller than that of rapidly quenched bulk CoFeCrAl, 456 K.[22] Such processing-related Curie temperature variations, which reflect site occupancy and stoichiometry, are not unusual, as exemplified by a Curie-temperature difference of 170 K between bulk and sputter-deposited thin-film Mn2CoAl.[8]

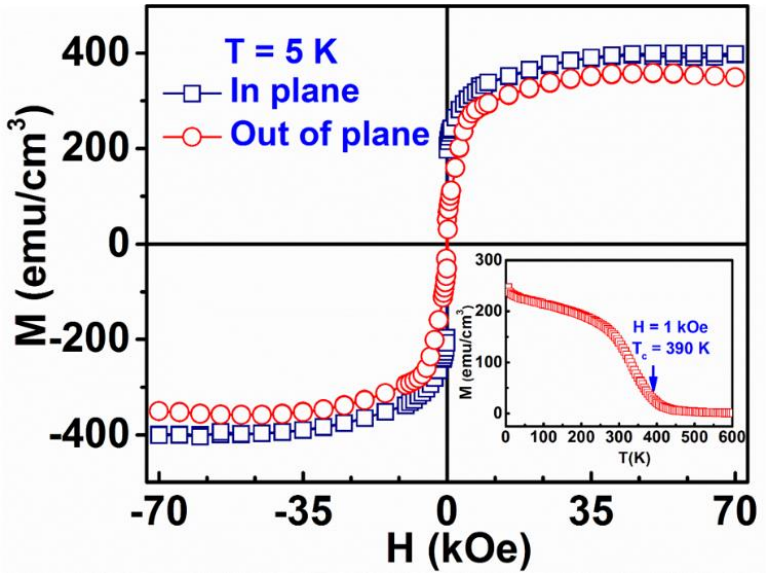

FIG. 3. 9 Magnetization of the epitaxial CoFeCrAl film at 5 K with the magnetic field applied parallel and perpendicular to the film plane. The inset shows temperature dependent magnetization M(T) of the epitaxial CoFeCrAl film measured at 1.0 kOe.

FIG. 3.10 (a) shows the isothermal magnetization curves *M*(*H*) of the 100-nm-thick CoFeCrAl polycrystalline film on Si substrate recorded at 5 K and 300 K. The films

are magnetically soft with coercivities being below 200 Oe. The saturation magnetizations M_s are 2.5 μB/f.u. at 5 K and 1.6 μB/f.u. at 300 K, respectively. The value of M_s measured at 5K is slightly higher than the value 2.0 μ_B/f.u. predicted by the Slater–Pauling curve and also calculated for CoFeCrAl compound with ferrimagnetic spin order (m_{co} = 0.94, m_{Fe} = −0.63, m_{cr} = 1.78 and m_{total} = 2.00 μB/f.u.).[13] The slightly higher value of M_s in our film is probably from excess cobalt as seen from the EDX analysis. The integral value of M_s is the characteristic feature of half-metallic magnets and has been observed in other half-metallic Heusler compounds, including the SGS compound Mn_2CoAl.[5] Figure 3. 10 (b) shows thermomagnetic curves $M(T)$ of the CoFeCrAl film measured at 1.0 kOe, where we see a gradual magnetic transition. Such slow magnetic transitions are found in ferrimagnetic materials due to a gradual reversal of magnetic moments in different magnetic sublattices.[30]

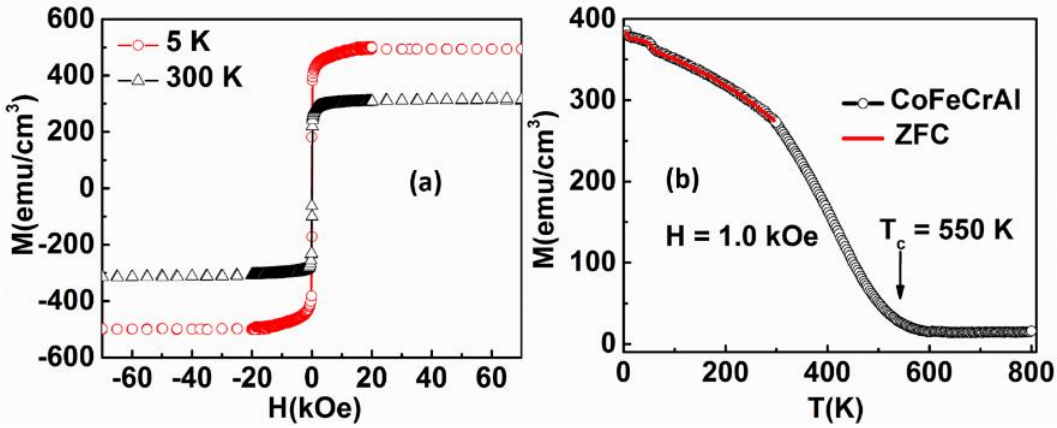

FIG. 3. 10 (a) Magnetization hysteresis loops of the synthesized film at 5 K and 300 K with the magnetic field applied out of the plane, respectively. (b) Temperature dependent magnetization M(T) of the 100-nm-thick film measured at 1.0 kOe.

3.5 Transport Properties

FIG. 3.11 shows the temperature dependence $\rho(T)$ of the longitudinal resistivity in zero magnetic field. The films are moderately conducting, with room-temperature (RT) resistivities of 150 μΩcm (MgO) and 210 μΩcm (Si). The respective residual resistivities are 187 μΩcm (MgO) and 268 μΩcm (Si). The value of 187 μΩcm for CoFeCrAl epitaxial film grown on MgO is substantially lower than those measured in more highly disordered bulk CoFeCrAl,[8] namely 810 μΩcm (RT) and 930 μΩcm (residual), and compare well with the room temperature resistivity of MBE-grown Mn_2CoAl films (280 μΩcm).[6] The order of magnitude of the CoFeCrAl resistivity is consistent with both SGS and dirty-metal resistivity, but the comparison of the two substrates suggests the CoFeCrAl film on Si substrate is highly disordered and falls into the dirty-metal regime, as shown in FIG. 3.2.

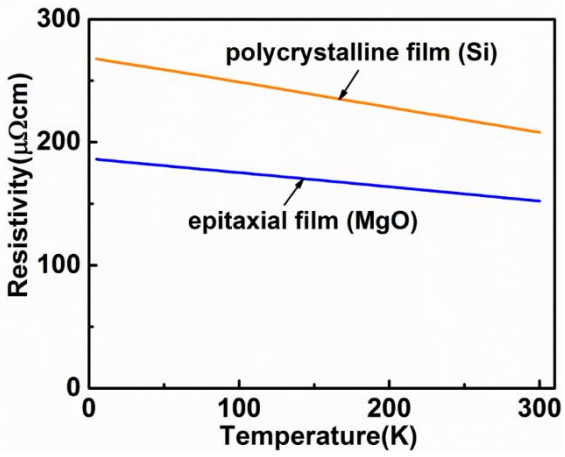

FIG. 3. 11 Temperature dependence of the longitudinal zero-field resistivity of CoFeCrAl on the two substrates.

Based on the above structural evidence, the films deposited on MgO are clearly the more ordered ones, both chemically and from the viewpoint of crystalline texture. In FIG. 3.2, they are therefore on the *left* of the Si films and structurally closer to an ideal SGS. Concerning transport, experiment (FIG. 3.11) shows that the resistivity of CoFeCrAl on MgO is *lower* than that of CoFeCrAl on Si. In terms of FIG. 3.2, the reduced resistivity is consistent with two scenarios, enclosed by the dashed box. While the film on Si lies on the dirty-metal branch of the curve, the MgO film may be a dirty metal or an SGS.

Note that the resistivity of the film decreases almost linearly with increasing temperature, but the temperature coefficients of the resistivity are very small, –0.12 μΩcm/K for epitaxial films (MgO) and –0.19 μΩcm/K for polycrystalline films (Si). By comparison, the temperature coefficients in bulk CoFeCrAl[10] and bulk Mn_2CoAl[5] are –0.50 μΩcm/K and –0.14 μΩcm/K, respectively. The $\rho(T)$ curves measured in a magnetic field of 70 kOe for films grown on both types of substrates are almost identical to the zero-field $\rho(T)$ curves, which indicates very small longitudinal magnetoresistance, that is,

$$MR = (\rho_{xx}^{7\,T} - \rho_{xx}^{0\,T})/\rho_{xx}^{0\,T} * 100\% \leq 0.5\%. \qquad [3.3]$$

This magnetoresistance is comparable to the magnetoresistance of 0.6% in thin-film Mn_2CoAl[5, 6, 8] and to that of 1.5%[17] in CoFeCrAl.

FIG. 3.12 shows the MR of the epitaxial CoFeCrAl film measured at various temperatures between 10 K and 300 K with magnetic field perpendicular to the film plane. The temperature dependence at high field (70 kOe) MR is shown as the inset of FIG. 3.12. As shown in FIG. 3.12, the MR curves of the epitaxial film are unsaturated up to 70 kOe. Such unusual linear behavior of MR has been found in other Heusler

compounds and explained as quantum magnetoresistance.[28] The negative MR can be attributed to the reduction of random spin-flip scattering process as the field aligns the magnetic moments, which is expected to increase as temperature decreases consistent with the plot in the inset of FIG. 3.12. At low temperatures, the increase in MR with temperature is logarithmic, which can be explained as caused by the presence of strong spin-orbit scattering.[31] The slope of the MR(H) curves changes abruptly near 10 kOe, which is more obvious for the low-temperature measurements. This is presumed to be due to strong spin-orbit scattering at the weak field but as field increases the magnetic scattering becomes dominant.

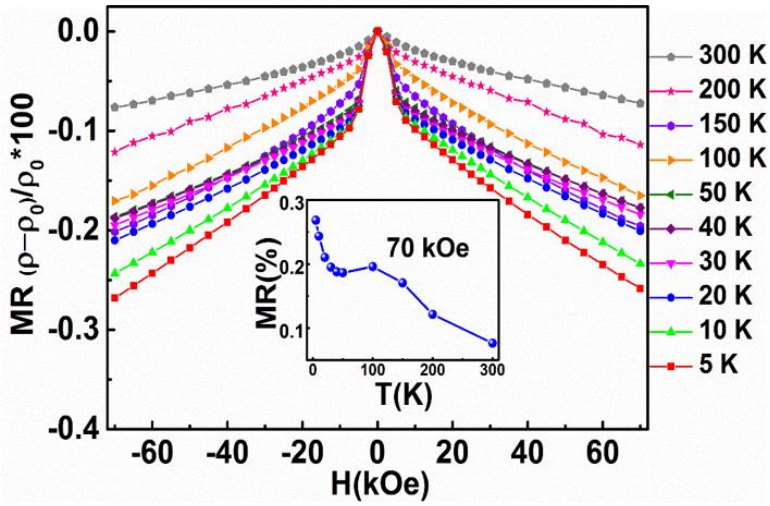

FIG. 3. 12 Magnetoresistivity (MR) of the epitaxial film measured at various temperatures with magnetic field perpendicular to the film plane, and the temperature dependence of the absolute value of MR.

FIG. 3.13 shows the MR of CoFeCrAl polycrystalline film on Si substrate measured with magnetic field perpendicular to the film plane and the variation of high-

field (70 kOe) MR with temperature is shown in the inset. The MR curves measured above 30 K are linear in the magnetic field up to 70 kOe, which are identical to that reported for both the bulk and film samples of another SGS compound Mn_2CoAl.[5, 8] However, the behavior is different for low temperature (< 40 K) measurements, where the MR first decreases with increasing field and then starts increasing linearly when the magnetic field exceeds a certain value. The turning points in the MR curves are 5 kOe, 10 kOe and 40 kOe for the curves measured at 30 K, 20 K and 10K, respectively, as shown in FIG. 3.13. We also note that MR is negative below 30 K and it is positive at and above 30 K. The negative MR is a consequence of the reduction of random spin-flip scattering process as the field aligns the magnetic moments. Bulk SGS materials have shown negative MR that transforms to positive at lower temperatures. However, as shown in the inset of FIG. 3.13, the MR shows a maximum around 50 K. The unusual temperature dependence of MR has also been observed in Mn_2CoAl.[6, 8] The negative value of MR indicates that the spin-dependent scattering is dominant at temperatures below 40 K. As shown in the Figure, this change leads to a W-shaped MR Curves, which may be caused by the spin-dependent scattering of conduction electrons.[32] Ferrimagnetic materials usually show negative MR which decreases with increasing temperature but the positive vale of MR in the high temperature regime may be attributed to the Lorentz force to the resistivity in the presence of a magnetic field.

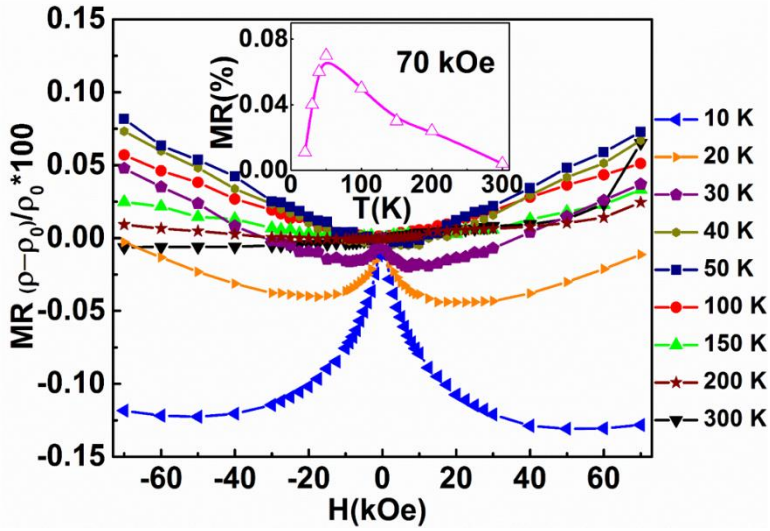

FIG. 3. 13 MR of polycrystalline film measured with magnetic field perpendicular to the film plane, and the inset shows the absolute MR value variation with temperature.

FIG. 3.14 shows the magnetic field dependence of Hall resistivities $\rho_{xy}(H)$ of epitaxial CoFeCrAl film measured between 5 K and 300 K. The $\rho_{xy}(H)$ curves are nonlinear at all temperatures and look identical in shape to the corresponding $M(H)$ curves. The ρ_{xy} can be expressed as $\rho_{xy}(H,T) = R_0 \cdot H + R_A \cdot M(H)$, where the first term in proportional to the external magnetic field (ordinary Hall resistivity) and the second term in proportional to the magnetization of the film (anomalous Hall resistivity). The coefficients R_0 and R_A in the expression are, respectively, the ordinary Hall coefficient and anomalous Hall coefficient. These coefficients can be determined by extrapolating the high-field portion of $\rho_{xy}(H)$ curve to H = 0, where the slope and intercept of the line are equal to R_0 and $R_A M(0)$, respectively, with M(0) being saturation magnetization.

The anomalous Hall coefficient R_A is related to the mechanism leading to anomalous Hall-effect. It follows a simple power-law dependence on longitudinal

resistivity ρ_{xx} of the form $R_A \propto (\rho_{xx})^m$ depending on the scattering mechanism, where m = 1 for skew-scattering and m = 2 for intrinsic plus side-jump scattering and can be expressed as $R_A = a\rho_{xx} + b\rho_{xx}^2$. The constants a and b contain information about the skew-scattering and intrinsic (Berry phase) plus side jump scattering mechanisms, respectively.[5] This means, experimentlly, we see $\rho_{xy}(0,T) \propto \rho_{xx}^2(T)$ if side jump plus intrinsic scattering is dominating AHE and $\rho_{xy}(0,T) \propto \rho_{xx}(T)$ if the skew-scattering is dominating AHE. As shown in the FIG. 3.14 inset, we have plotted $\rho_{xy}(0)$ at 10, 30, 50, 100, 200 and 300 K as a function of ρ_{xx}^2 at the corresponding temperatures and found a linear relationship. This indicates that the side-jump (plus intrinsic) mechanism is responsible for the observed anomalous Hall-effect in our epitaxial films.[33] We have also estimated the Hall conductivity using an expression $\sigma_{xy} = \frac{\rho_{xy}}{\rho_{xx}^2}$. The low temperature (10 K) σ_{xy} is 130 S/cm which is close to the value (121.8 S/cm) predicted for the B2-type disordered parent compound Co_2CrAl.[34]

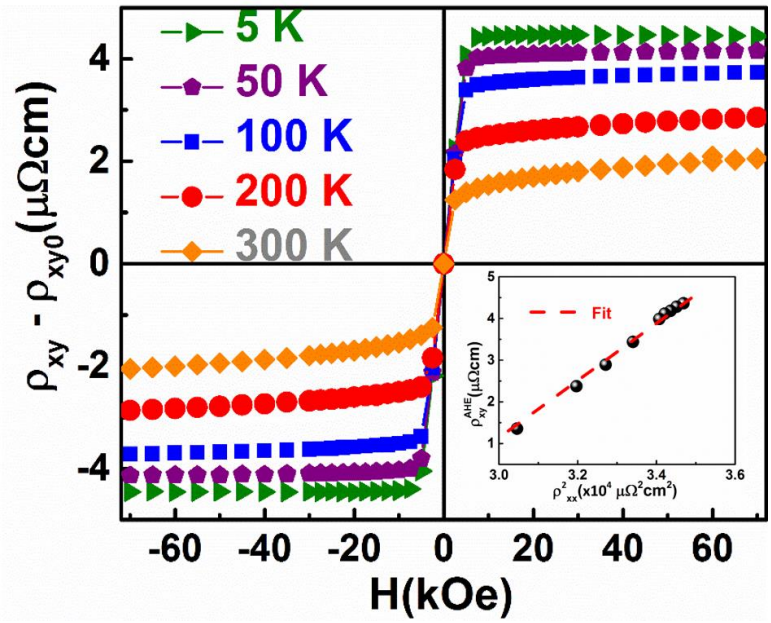

FIG. 3. 14 Magnetic field dependent Hall resistivities ρ_{xy} of the epitaxial CoFeCrAl film measured at selected temperatures. The inset shows anomalous Hall resistivity ρ_{xy}^{AHE} versus the squared longitudinal resistivity ρ_{xx} of the epitaxial film. The dashed red line is a linear fit.

FIG. 3.15 plots Hall-effect ρ_{xy} of polycrystalline CoFeCrAl film measured for various temperatures and selected 10 K, 30 K, 50 K, 100 K, 300 K as shown. The $\rho_{xy}(H)$ curves show the same hysteresis loops as that of epitaxial CoFeCrAl film. The lower inset shows the temperature dependence of anomalous Hall resistivity ρ_{xy}^{AHE} of polycrystalline CoFeCrAl film. It shows the same negative coefficient as that of epitaxial CoFeCrAl film.

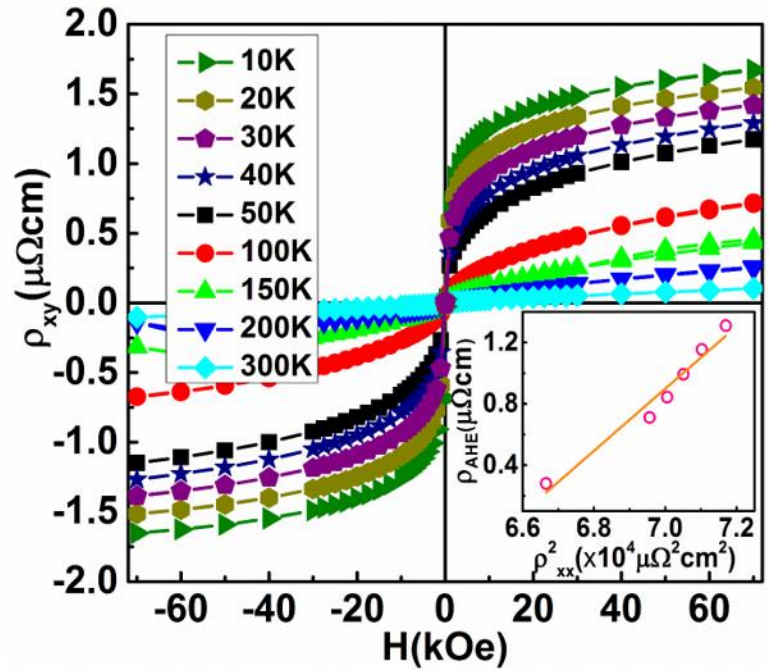

FIG. 3. 15 Magnetic field dependent Hall resistivities ρ_{xy} of the polycrystalline CoFeCrAl film measured at selected temperatures. The inset shows anomalous Hall resistivity ρ_{xy}^{AHE} versus the squared longitudinal resistivity ρ_{xx} of the epitaxial film. The orange line is a linear fit.

The Hall conductivity is given as $\sigma_{xy} = \frac{\rho_{xy}}{\rho_{xx}^2+\rho_{xy}^2}$, but in our case ρ_{xx} is two orders of magnitude higher than ρ_{xy} and can be approximated by $\sigma_{xy} = \frac{\rho_{xy}}{\rho_{xx}^2}$. We have calculated the values of σ_{xy} and plot the field dependence of Hall conductivity of epitaxial and polycrystalline films for different temperatures as shown in FIG. 3.16 (a) and (b), respectively. By extrapolating the high field portion of $\sigma_{xy}(H)$, we can obtain the anomalous Hall conductivity σ_{xy}^{AHE} for the corresponding temperature. It is obvious that the anomalous Hall conductivity σ_{xy}^{AHE} increases as the temperature decreases, which is the opposite trend to that of half-metallic Heusler compounds and metals[35, 36] but the

same as that of most semiconductors and reported SGS.[8, 37-39] For instance, the value of σ_{xy}^{AHE} of the epitaxial film at 5 K is 130 S/cm, while 23 S/cm for the polycrystalline film at 10 K, which is close to the value reported for the oriented Mn_2CoAl film (22 S/cm).[6]

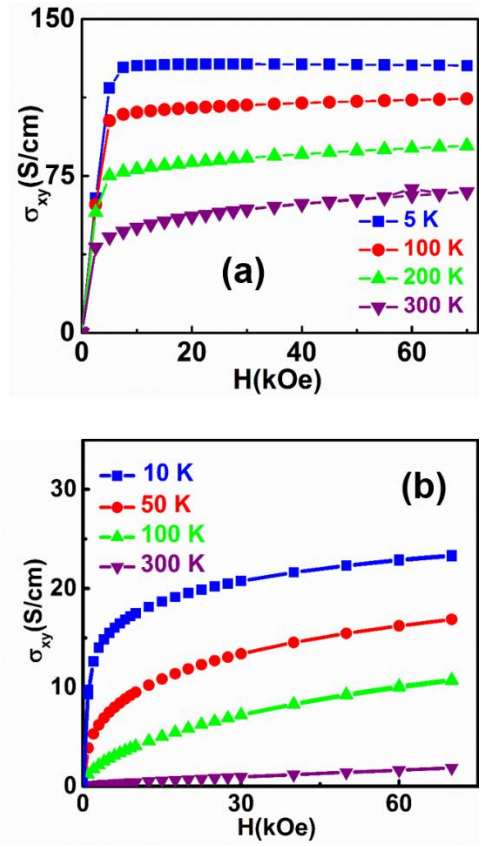

FIG. 3. 16 (a) Hall conductivity σ_{xy} of oriented CoFeCrAl film calculated for selected temperatures. (b) Hall conductivity σ_{xy} of polycrystalline CoFeCrAl film calculated for selected temperatures.

We have determined the carrier concentration *n* and mobility μ in our films using the single-band model, where $R_0 = 1/ne$ and $\mu = R_0(T)/\rho(T)$. FIG. 3.17 shows temperature dependence of carrier concentration of polycrystalline and epitaxial CoFeCrAl films, where *n* is almost constant up to 150 K but increases rapidly with

further increase in temperature. The rapid increase in *n*(T) above 150 K may be due to the onset of thermal excitations across the half-metallic band gap. As the temperature increases, the carrier mobility decreases approximately. FIG. 3.18 shows temperature dependence of mobility of polycrystalline and epitaxial CoFeCrAl films. The mobility remains almost constant until 150 K and then slightly decreases with further increase in temperature. Typical values of *n* and μ for oriented film at 5 K are 1.2 $\times 10^{18}$ cm^{-3} and 33 $cm^2/(V \cdot s)$, respectively, while typical values of *n* and μ for polycrystalline film at 10 K are 1.3×10^{18} cm^{-3} and 22 $cm^2/(V \cdot s)$, respectively, which are less than the values reported for oriented SGS Mn_2CoAl film (10^{20} cm^{-3})[8], bulk Fe_2VAl (10^{21} cm^{-3})[40] and Co-doped magnetic semiconductor ZnO film[38]. However, the value of *n* in our sample is greater than those of HgCdTe (10^{15} - 10^{17} cm^{-3})[41] and bulk Mn_2CoAl (10^{17} cm^{-3}).[42] Similar temperature independent behavior of *n* has been found in other SGS materials as well.[9]

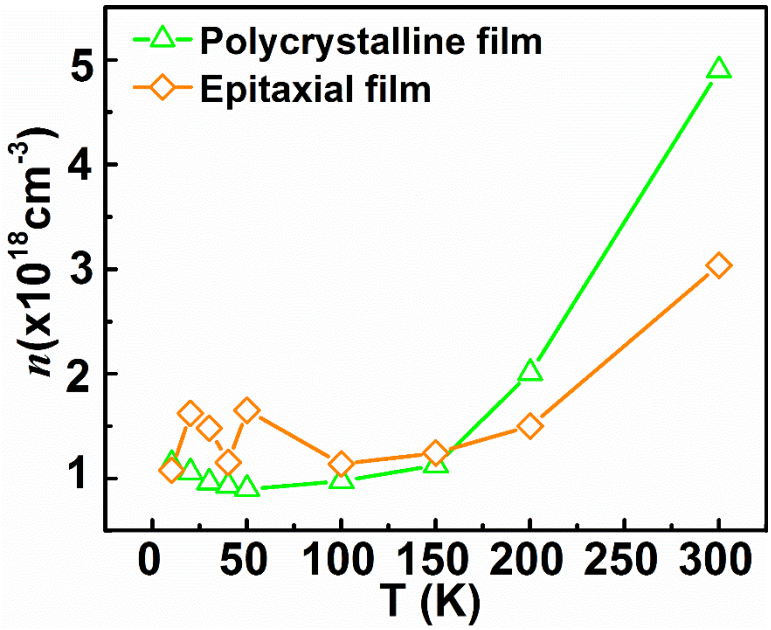

FIG. 3. 17 Temperature dependence of carrier concentration *n* of epitaxial and polycrystalline CoFeCrAl films.

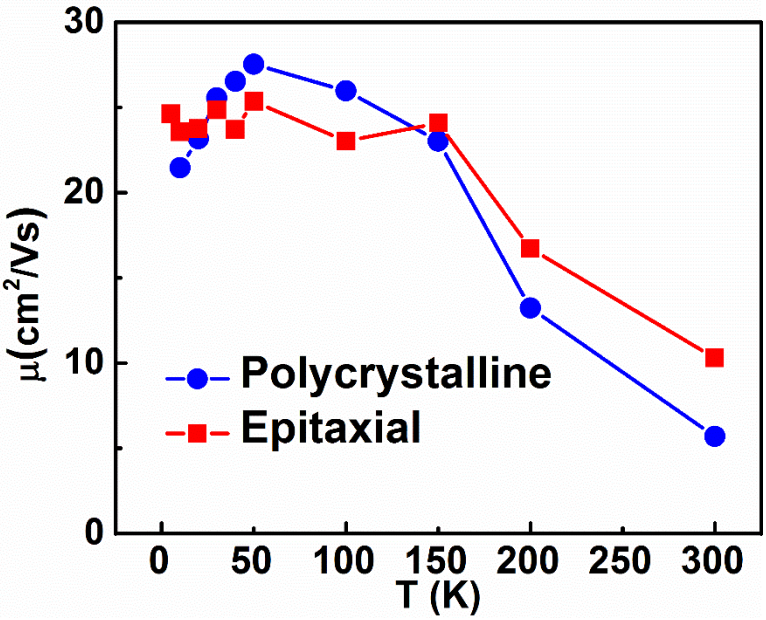

FIG. 3. 18 Temperature dependence of mobility μ of epitaxial and polycrystalline CoFeCrAl films.

3.6 Experimental Observations of Heusler Compound Spin Polarization

The degree of transport spin-polarization (P_T) was measured using PCAR technique where the conductance spectra were recorded at the interface between the sample and the superconducting Pb tip at 1.8 K.[43, 44] In this technique, a current is injected from normal metal into a singlet superconductor. For the electron to enter into the superconductor and proceed as a part of supercurrent, it must be paired with another electron of opposite spin leaving a hole in the interface which propagates away from the interface (Andreev reflection). In the case of a half-metal with no minority spin states at the Fermi level, there is no Andreev reflection and thus the conductance across the half-metal-superconductor interface is zero. Therefore, for magnetic materials, the Andreev reflection is limited by the minority spin states available at the Fermi level. Depending on the experiment, P_T is given as

$$P_{N_v} = \frac{\langle Nv\rangle\uparrow - \langle Nv\rangle\downarrow}{\langle Nv\rangle\uparrow + \langle Nv\rangle\downarrow} \; or \; P_{N_{v^2}} = \frac{\langle Nv^2\rangle\uparrow - \langle Nv^2\rangle\downarrow}{\langle Nv^2\rangle\uparrow + \langle Nv^2\rangle\downarrow} \qquad [3.4]$$

for the ballistic and diffusive regimes, respectively. Here, *v* and *N* are the fermi velocity and spin-projected density of states for majority (↑) and minority (↓) spins, respectively.[43-46] In our experiment, the value of P_T was extracted by analyzing the PCAR spectra using the modified Blonder-Tinkham-Klapwijk (BTK) model in the ballistic regime taking into account factors such as interfacial scattering (Z), inelastic scattering (Γ), temperature (*T*), superconducting gap (Δ), and extra resistance (r_E).[47, 48]

P_T of two CoFeCrAl samples with thicknesses 100 nm and 56.7 nm and surface protective Al layers of thickness 2 nm. The sharp tip of a few nanometers was made by mechanically polishing a superconducting Pb wire (transition temperature 7.2 K) of the diameter of 0.030 inches. Both the sample and the tip were enclosed in a vacuum jacket with 10 milliTorr of exchange-gas pressure and first cooled to 4.2 K and then to 1.8 by pumping liquid helium. Point contacts were established at the desired temperature using a differential screw mechanism.

More than 10 point contacts were measured for each sample. FIG. 3.19 (a-d) shows some representative PCAR spectra, where the open circles are the experimental data and the solid curves are the best fit to the modified BTK model. All the contacts have contact resistance between 150 Ω and 300 Ω. From Sharvin's formula, the contact size can be estimated to be a few nm, much smaller than the mean free path of the sample, which is above 1 μm from the Drude model using above resistivity and carrier concentration. So all the contacts are in the ballistic regime and any diffusive effect, if present, is attributed to the Z factor in the analysis.[48] All the spectra show a double-peak structure which is the hallmark of Andreev reflection. In Andreev reflection

spectroscopy, the peak value usually indicates the superconducting gap. In our case, the gap value of the Pb is about 1.33 meV at 1.8 K, but the peak value is larger than 5 mV, as shown in FIG. 3.19. This is due to the large resistivity of the CoFeCrAl sample, which adds an extra resistance in series with the point contact.[48] We note that the thin sample has a larger r_E than that of the thick sample due to its larger resistivity as shown in FIG. 3.19 (a) and (b). At $V = 0$, the conductance is suppressed to less than 1, indicating a P_T of larger than 50 %. All the recorded data can be well described by the modified BTK model if the effect of r_E is included.

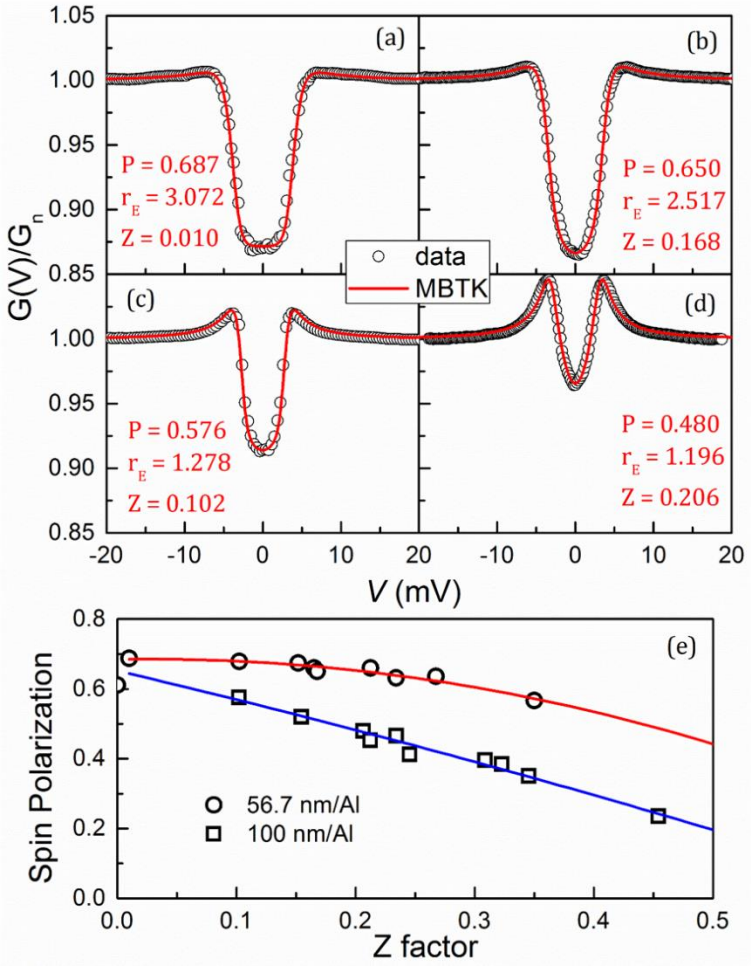

FIG. 3. 19 Representative normalized differential conductance curves of the epitaxial CoFeCrAl film with thickness 56.7 nm (a, b) and thickness 100 nm (c, d) obtained at 1.8 K. The open circles denote the experimental data and the solid lines are the fit to the data using modified BTK model. The Z dependence of P_T with a quadratic fit to the data for both samples are shown in Figure (e).

FIG. 3.19 (e) shows the *Z* dependence of transport spin-polarization for both the samples taking the extrapolation of the least-squares fit the case of the transparent interface ($Z = 0$) to obtain the limiting values of P_T. As shown in the Figure, the P_T values

for both the samples decrease as Z increases which is due to spin-flip scattering at the interface. Although the P_T for the thin-film sample is higher at higher Z factors, the limiting values of P_T at $Z = 0$ are almost the same for both the samples, $P_T = 0.652 \pm 0.034$ for the 100 nm and 0.685 ± 0.011 for the 56.7 nm sample. The discrepancy in the P_T values at large Z may be attributed to the difference in the oxidation level of the top Al protective layer, which causes different spin-flip scattering. We note that the 100 nm film was measured two weeks after the measurement of 67.5 nm sample. In fact, a Z factor smaller than 0.1 was not achieved experimentally for the thick sample.

The measured value of spin polarization (68%) in our CoFeCrAl films compares well with the values reported for other partially disordered Heusler compounds such as bulk CoFeCrAl (67%)[17], bulk CoFeMnGe (70%)[49] and thin film $Co_2Fe(Ga_{0.5}Ge_{0.5})$ (75%).[50] Hono *et al.* have investigated the effect of disorder on the spin polarization of half-metallic Co_2MnGe and found 35% for A2-type disordered and 56% for the cubic $L2_1$ ordered films[14] indicating that the degree of spin polarization is highly sensitive to the structural disorder. The P_T in our samples is much larger than the values measured in $L2_1$ ordered bulk and thin-film samples of Co_2MnGe and Co_2MnSi compounds.[14] Note that the BTK model sometimes underestimates the spin polarization due to spin mixing at the interface.[51]

3.7 Summary

In conclusion, we have investigated how the structural disorder affects the magnetic and transport behavior of CoFeCrAl thin films deposited on MgO and Si. Our

films exhibit nearly perfect epitaxy and a high degree of $L2_1$ Heusler order. All considered types of chemical disorder destroy the spin-gapless semiconductivity of Y-ordered CoFeCrAl, but B2 disorder and A2-type Cr-Fe disorder preserve the half-metallicity of the compound. The latter, a specific feature of CoFeCrAl, does not exist in related Heusler compounds such as $Co2(Fe_{1-x}Cr_x)Al$ and must be contrasted to A2-type Cr-Co disorder, which has a profound effect on the electronic structure and destroys half-metallicity.

Secondly, CoFeCrAl films deposited on MgO and Si with exhibit different degrees of structural order: the MgO substrate yields well-ordered epitaxial films, whereas the films deposited on Si are highly disordered and polycrystalline. The resistivity was measured as a function of temperature and the residual resistivity was analyzed as a function of the disorder. The films on Si have the higher residual resistivity, which indicates dirty-metal behavior, whereas the behavior of the films on MgO is consistent with both dirty-metal or spin-gapless semiconducting behavior. The saturation magnetization of the CoFeCrAl film approaches the theoretical value of 2.0 μB with high Curie temperature of 390 K for oriented film and 510 K for polycrystalline film, less than bulk value. The carrier concentration and mobility expectedly fall into the regime of semiconductors and is comparable to the reported values of other SGSs.

Based on our experiments (PCAR, X-ray line intensities, magnetization) we find that the spin polarization at the Fermi level is about 68%. Our findings are encouraging for spin-electronics applications, due to the robustness of the half-metallicity with respect to most types of chemical disorder and because the disorder enhances the resistivity without much reduction in Curie temperature.

3.8 Bibliography

1. Y. S. Dedkov, U. Rüdiger and G. Güntherodt, "Evidence for the half-metallic ferromagnetic state of Fe_3O_4 by spin-resolved photoelectron spectroscopy", Physical Review B **65**, 064417 (2002).

2. K. P. Kämper, W. Schmitt, G. Güntherodt, R. J. Gambino and R. Ruf, "CrO_2 a new half-metallic ferromagnet?", Physical Review Letters **59**, 2788-2791 (1987).

3. X. L. Wang, "Proposal for a new class of materials: Spin-gapless semiconductors", Physical Review Letters **100**, 156404 (2008).

4. X. Wang, G. Peleckis, C. Zhang, H. Kimura and S. Dou, "Colossal electroresistance and giant magnetoresistance in doped $PbPdO_2$ thin films", Advanced Materials **21**, 2196-2199 (2009).

5. S. Ouardi, G. H. Fecher, C. Felser and J. Kübler, "Realization of spin-gapless semiconductors: The heusler compound Mn_2CoAl", Physical Review Letters **110**, 100401 (2013).

6. M. E. Jamer, B. A. Assaf, T. Devakul and D. Heiman, "Magnetic and transport properties of Mn_2CoAl oriented films", Applied Physics Letters **103**, 142403 (2013).

7. G. Z. Xu, E. K. Liu, Y. Du, G. J. Li, G. D. Liu, W. H. Wang and G. H. Wu, "A new spin-gapless semiconductors family: Quaternary Heusler compounds", EPL (Europhysics Letters) **102**, 17007 (2013).

8. G. Z. Xu, Y. Du, X. M. Zhang, H. G. Zhang, E. K. Liu, W. H. Wang and G. H. Wu, "Magneto-transport properties of oriented Mn_2CoAl films sputtered on thermally oxidized Si substrates", Applied Physics Letters **104**, 242408 (2014).

9. L. Bainsla, A. I. Mallick, M. M. Raja, A. K. Nigam, B. S. D. C. S. Varaprasad, Y. K. Takahashi, A. Alam, K. G. Suresh and K. Hono, "Spin-gapless semiconducting behavior in equiatomic quaternary CoFeMnSi Heusler compound", Physical Review B **91**, 104408 (2015).

10. P. Kharel, W. Zhang, R. Skomski, S. Valloppilly, Y. Huh, R. Fuglsby, S. Gilbert and D. J. Sellmyer, "Magnetism, electron transport and effect of disorder in CoFeCrAl", Journal of Physics D: Applied Physics **48**, 245002 (2015).

11. P. Lukashev, P. Kharel, S. Gilbert, B. Staten, N. Hurley, R. Fuglsby, Y. Huh, S. Valloppilly, W. Zhang, K. Yang, R. Skomski and D. J. Sellmyer, "Investigation of spin-gapless semiconductivity and half-metallicity in Ti_2MnAl-based compounds", Applied Physics Letters **108**, 141901 (2016).

12. S. Skaftouros, K. Özdoğan, E. Şaşıoğlu and I. Galanakis, "Search for spin-gapless semiconductors: The case of inverse Heusler compounds", Applied Physics Letters **102**, 022402 (2013).

13. K. Özdoğan, E. Şaşıoğlu and I. Galanakis, "Slater-Pauling behavior in LiMgPdSn-type multifunctional quaternary Heusler materials: Half-metallicity, spin-gapless and magnetic semiconductors", Journal of Applied Physics **113**, 193903 (2013).

14. A. Rajanikanth, Y. K. Takahashi and K. Hono, "Spin polarization of Co_2MnGe and Co_2MnSi thin films with A2 and $L2_1$ structures", Journal of Applied Physics **101**, 023901 (2007).

15. H. Liu, Y. Honda, T. Taira, K. Matsuda, M. Arita, T. Uemura and M. Yamamoto, "Giant tunneling magnetoresistance in epitaxial $Co_2MnSi/MgO/Co_2MnSi$ magnetic

tunnel junctions by half-metallicity of Co_2MnSi and coherent tunneling", Applied Physics Letters **101**, 132418 (2012).

16. R. Choudhary, P. Kharel, S. R. Valloppilly, Y. Jin, A. O'Connell, Y. Huh, S. Gilbert, A. Kashyap, D. J. Sellmyer and R. Skomski, "Structural disorder and magnetism in the spin-gapless semiconductor CoFeCrAl", AIP Advances **6**, 056304 (2016).

17. L. Bainsla, A. I. Mallick, A. A. Coelho, A. K. Nigam, B. S. D. C. S. Varaprasad, Y. K. Takahashi, A. Alam, K. G. Suresh and K. Hono, "High spin polarization and spin splitting in equiatomic quaternary CoFeCrAl Heusler compound", Journal of Magnetism and Magnetic Materials **394**, 82-86 (2015).

18. Z. Gercsi and K. Hono, "Ab initio predictions for the effect of disorder and quarternary compounding on the half-metallic properties of selected Co_2Fe-based Heusler compounds", Journal of Physics: Condensed Matter **19**, 326216 (2007).

19. K. Kobayashi, R. Y. Umetsu, R. Kainuma, K. Ishida, T. Oyamada, A. Fujita and K. Fukamichi, "Phase separation and magnetic properties of half-metal-type $Co_2Cr_{1-x}Fe_xAl$ compounds", Applied Physics Letters **85**, 4684-4686 (2004).

20. S. V. Karthik, A. Rajanikanth, Y. K. Takahashi, T. Okhubo and K. Hono, "Spin polarization of quaternary $Co_2Cr_{1-x}Fe_xAl$ Heusler compounds", Applied Physics Letters **89**, 052505 (2006).

21. Y. Takamura, R. Nakane and S. Sugahara, "Analysis of $L2_1$-ordering in full-Heusler Co_2FeSi compound thin films formed by rapid thermal annealing", Journal of Applied Physics **105**, 07B109 (2009).

22. Y. Miura, K. Nagao and M. Shirai, "Atomic disorder effects on half-metallicity of the full-Heusler compounds $Co_2Cr_{1-x}Fe_xAl$ A first-principles study", Physical Review B **69**, 144413 (2004).

23. J. H. Mooij, "Electrical conduction in concentrated disordered transition metal compounds", Physica Status Solidi (a) **17**, 521-530 (1973).

24. C. Nölscher, P. Müller, H. Adrian, M. Lehmann and G. Saemann-Ischenko, "Hydrogenated and irradiated $A_{15}Nb_3Sn$ layers — Preparation, Rutherford scattering analysis, resistivity and superconductivity", Zeitschrift für Physik B Condensed Matter **41**, 291-299 (1981).

25. T. L. Alford, K. S. Gadre, H. C. Kim and S. C. Deevi, "Abnormal electrical resistivity in γ-TiAl thin films deposited by magnetron sputtering", Applied Physics Letters **83**, 455-457 (2003).

26. R. Hight, C. Plough and D. J. Sellmyer, "Temperature-dependent resistivity of highly disordered Ni-Cr-Al compounds", Physical Review B **29**, 5920-5921 (1984).

27. P. B. Allen, in *Conceptual Foundations of Material Properties:A standard model for calculation of ground- and excited-state properties*, edited by M. L. C. a. S. G. Louie (Elsevier, 2006), Vol. Amsterdam, pp. 165-218.

28. A. A. Abrikosov, "Quantum magnetoresistance", Physical Review B **58**, 2788-2794 (1998).

29. X. L. Wang, S. X. Dou and C. Zhang, "Zero-gap materials for future spintronics, electronics and optics", NPG Asia Mater. **2**, 31-38 (2010).

30. J. S. Smart and J. H. Van Vleck, "Effective field theories of magnetism", Physics Today **19**, 77-78 (1966).

31. S. Hikami, A. I. Larkin and Y. Nagaoka, "Spin-Orbit Interaction and Magnetoresistance in the Two Dimensional Random System", Progress of Theoretical Physics **63**, 707-710 (1980).

32. Y. Du, G. Z. Xu, X. M. Zhang, Z. Y. Liu, S. Y. Yu, E. K. Liu, W. H. Wang and G. H. Wu, "Crossover of magnetoresistance in the zero-gap half-metallic Heusler compound Fe $_2$CoSi", EPL (Europhysics Letters) **103**, 37011 (2013).

33. E. Vilanova Vidal, H. Schneider and G. Jakob, "Influence of disorder on anomalous Hall-effect for Heusler compounds", Physical Review B **83**, 174410 (2011).

34. J. Kudrnovský, V. Drchal and I. Turek, "Anomalous Hall-effect in stoichiometric Heusler compounds with native disorder: A first-principles study", Physical Review B **88**, 014422 (2013).

35. S. Sangiao, L. Morellon, G. Simon, J. M. De Teresa, J. A. Pardo, J. Arbiol and M. R. Ibarra, "Anomalous Hall-effect in Fe (001) epitaxial thin films over a wide range in conductivity", Physical Review B **79**, 014431 (2009).

36. M. Obaida, K. Westerholt and H. Zabel, "Magnetotransport properties of Cu_2MnAl, Co_2MnGe, and Co_2MnSi Heusler compound thin films: From nanocrystalline disordered state to long-range-ordered crystalline state", Physical Review B **84**, 184416 (2011).

37. D. Chiba, A. Werpachowska, M. Endo, Y. Nishitani, F. Matsukura, T. Dietl and H. Ohno, "Anomalous Hall-effect in Field-Effect Structures of (Ga,Mn)As", Physical Review Letters **104**, 106601 (2010).

38. Q. Xu, L. Hartmann, H. Schmidt, H. Hochmuth, M. Lorenz, R. Schmidt-Grund, C. Sturm, D. Spemann, M. Grundmann and Y. Liu, "Magnetoresistance and anomalous Hall-effect in magnetic ZnO films", Journal of Applied Physics **101**, 063918 (2007).

39. R. Ramaneti, J. C. Lodder and R. Jansen, "Anomalous Hall-effect in anatase Co:TiO_2 ferromagnetic semiconductor", Applied Physics Letters **91**, 012502 (2007).

40. V. I. Okulov, V. E. Arkhipov, T. E. Govorkova, A. V. Korolev, K. A. Okulova, E. I. Shreder, V. V. Marchenkov and H. W. Weber, "Experimental validation of the anomalies in the electron density of states in semiconductor iron-vanadium-aluminum compounds", Low Temperature Physics **33**, 692-698 (2007).

41. T. I. M, "Electron Spectrum of Gapless Semiconductors ", Springer Series in Solid-State Sciences ed K von Klitzing vol **116**, (1996).

42. S. Ouardi, G. H. Fecher, C. Felser and J. Kübler, "Realization of Spin-gapless Semiconductors: The Heusler Compound ${\mathrm{Mn}}_{2}\mathrm{CoAl}$", Physical Review Letters **110**, 100401 (2013).

43. R. J. Soulen, J. M. Byers, M. S. Osofsky, B. Nadgorny, T. Ambrose, S. F. Cheng, P. R. Broussard, C. T. Tanaka, J. Nowak, J. S. Moodera, A. Barry and J. M. D. Coey, "Measuring the Spin Polarization of a Metal with a Superconducting Point Contact", Science **282**, 85-88 (1998).

44. S. K. Upadhyay, A. Palanisami, R. N. Louie and R. A. Buhrman, "Probing Ferromagnets with Andreev Reflection", Physical Review Letters **81**, 3247-3250 (1998).

45. I. I. Mazin, "How to Define and Calculate the Degree of Spin Polarization in Ferromagnets", Physical Review Letters **83**, 1427-1430 (1999).

46. P. Kharel, P. Thapa, P. Lukashev, R. F. Sabirianov, E. Y. Tsymbal, D. J. Sellmyer and B. Nadgorny, "Transport spin polarization of high Curie temperature MnBi films", Physical Review B **83**, 024415 (2011).

47. G. E. Blonder, M. Tinkham and T. M. Klapwijk, "Transition from metallic to tunneling regimes in superconducting microconstrictions: Excess current, charge imbalance, and supercurrent conversion", Physical Review B **25**, 4515-4532 (1982).

48. T. Y. Chen, S. X. Huang and C. L. Chien, "Pronounced effects of additional resistance in Andreev reflection spectroscopy", Physical Review B **81**, 214444 (2010).

49. L. Bainsla, K. G. Suresh, A. K. Nigam, M. Manivel Raja, B. S. D. C. S. Varaprasad, Y. K. Takahashi and K. Hono, "High spin polarization in CoFeMnGe equiatomic quaternary Heusler compound", Journal of Applied Physics **116**, 203902 (2014).

50. B. S. D. C. S. Varaprasad, A. Srinivasan, Y. K. Takahashi, M. Hayashi, A. Rajanikanth and K. Hono, "Spin polarization and Gilbert damping of $Co_2Fe(Ga_xGe_{1-x})$ Heusler compounds", Acta Mater. **60**, 6257-6265 (2012).

51. T. Löfwander, R. Grein and M. Eschrig, "Is CrO_2 Fully Spin Polarized? Analysis of Andreev Spectra and Excess Current", Physical Review Letters **105**, 207001 (2010).

Table of Contents

Chapter 4. Structural, Magnetic and Electron-Transport Properties of Epitaxial Inverse Tetragonal Mn_2PtSn Films

This chapter discusses the epitaxial thin films of Mn_2PtSn grown on a MgO (001) substrate by magnetron co-sputtering of the constituents. Structural, magnetic and transport properties were investigated. The structure of epitaxial Mn_2PtSn film is inverse tetragonal with lattice constants a = 0.4488 nm, and b = 0.6148 nm (space group I-4m2, No. 119). Lattice constants have a very small mismatch with MgO, which makes it promising for coherent electron-tunneling phenomena. Measured saturation magnetization is 3.2 μ_B/f.u., less than that calculated from density of states. The magnetization measurements revealed an in-plane anisotropy energy of 10 Merg/cm^3. The magnetoresistance ratio is 1.0 % with a magnetic field applied out of the plane.

Many of the results presented in this chapter are adapted from the manuscript:

Y. Jin, P. Kharel, S. Valloppilly, T. Y. Chen and D. J. Sellmyer, "Structural, Magnetic and Electron-Transport Properties of Epitaxial Inverse Tetragonal Mn_2PtSn Films". (to be submitted)

I performed the synthesis and structural, magnetic and transport characterization of the Mn_2PtSn Films. S. R. Valloppilly helped with XRD measurement. P. Kharel assisted in revising the manuscript. All co-authors contributed to the final manuscript.

4.1 Introduction

Ferromagnetic half-metallic Heusler compounds are very promising materials for spintronic application as a spin aligner, spin injector, etc., due to their very high degree of spin polarization at the Fermi level.[1] For example, among the most recent examples are

half-metallic Co_2MnSi,[2] spin-gapless semiconducting Mn_2CoAl,[3, 4] and giant intrinsic exchange bias in the $Mn_{3-x}Pt_xGa$ compounds.[5] As a branch of the family of Heusler compounds, ferromagnetic Mn-based tetragonal compounds such as Mn_2YZ (Y = transition metals, Z = Al, Ga, and Sn) are special and have been actively investigated due to a high magnetic anisotropy constant, above-room-temperature Curie temperatures and potential applications including permanent magnets, high-density recording, multiferroic shape memory compounds, topological insulators, etc.[6-16] For instance, Mn_2RhSn crystallizes in the inverse tetragonal Heusler structure and the epitaxial thin film sputtered onto MgO substrates exhibited a complex noncollinear magnetic behavior and a moderately low anisotropy energy K_u = 0.89 Merg/cm^3 than calculated K_u of 500 Merg/m^3.[17, 18] Epitaxially grown tetragonal Mn_3Ga films exhibit a spin polarization of up to 58%, together with uniaxial anisotropy (K_u = 8.9 Merg/cm^3) and low magnetization.[19] Winterlik *et al*. calculated magnetocrystalline anisotropy energy of Mn_2-based inverse tetragonal Heusler compounds and found the magnetocrystalline anisotropy K_u is tunable by element composition adjustment, such as $Mn_xCo_{3-x}Ga$, $Mn_xFe_{3-x}Ga$, $Mn_xNi_{3-x}Ga$, Mn_2YSn (Y = Pt, Rh, Ir). Among them, Mn_2PtSn in the inverse-tetragonal crystal structure has been predicted to have a ferromagnetic spin structure (T_c = 374 K) with high magnetocrystalline anisotropy (50 Merg/cm^3).[20] The calculated electronic band structures are similar to those of half-metals, where the transport spin polarization at the Fermi level is about 91%.[21] It is ideal for high density magnetoresistive random access memory (MRAM) with in-plane magnetic tunnel junctions (MTJs) and spin-transfer-torque magnetic random access memories (STT-MRAMs).[6-8] The measured high-field magnetization and anisotropy constant for bulk Mn_2PtSn are 405 emu/cm^3 and 2.6

Merg/cm^3, respectively.[22, 23] Since practical spintronic devices require high-quality thin films, it is of vital importance to obtain single crystalline epitaxial thin films of Mn_2PtSn with desired structure and magnetic anisotropy constant and to have a complete understanding of the magnetic and electron-transport properties performance in thin films.

In this chapter, an experimental investigation on the epitaxial films of Mn_2PtSn prepared by magnetron sputtering technique on atomically flat MgO substrates is presented. Mn_2PtSn crystallizes in the inverse tetragonal Heusler structure. It exhibits a lattice mismatch of about 3.6 % with MgO (the lattice parameters are given in structural analysis session). A small lattice mismatch is an important condition for the successful manufacturing of thin films and tunnel junctions by epitaxial growth.

4.2 Experimental Details

All samples of Mn_2PtSn films presented in this Chapter were deposited on atomically flat C-cut MgO using magnetron sputtering system with a base pressure of about 3×10^{-8} Torr. Mn, Pt, and Sn targets were used for film deposition under optimized conditions: Ar pressure of 2×10^{-3} Torr, the substrate temperature at 773 K for MgO, DC power of 52.5 W for Mn target, and RF power of 10.0 W and 26.4 W for Pt and Sn targets, respectively. The crystal structure of the films and the epitaxy relationship of Mn_2PtSn/MgO (001) were investigated by in-plane and out-of-plane x-ray diffraction (XRD) using a Rigaku SmartLab Diffractometer with Cu Kα radiation (wavelength of about 1.5406 Å) and a Bruker-AXS D8 Discover Diffractometer as well as a FEI Tecnai Osiris (Scanning) Transmission Electron Microscope (TEM). The elemental compositions of the samples were determined using energy-dispersive x-ray spectroscopy

(EDX) in a FEI Nova NanoSEM450. The magnetic and electron-transport properties were measured using a Quantum Design superconducting quantum interference device (SQUID) magnetometer and physical property measurement system (PPMS).

4.3 Structural Properties

We first investigate the structural properties. FIG. 4.1 (a) shows the out-of-plane XRD pattern of the 90-nm-thick Mn_2PtSn film deposited on a Si (100) substrate. The prominent peaks in the pattern other than the peak around 69° were indexed with the inverse tetragonal structure, which indicates the film is a polycrystalline film. FIG. 4.1 (b) shows the out of plane XRD pattern of Mn_2PtSn on a C-cut MgO (001) substrate. The two prominent peaks in the pattern other than that around 44° from MgO substrate are from the (110) and (220) planes of Mn_2PtSn, indicating that the films are grown with a high degree of orientation relationship with the cube axes of MgO.

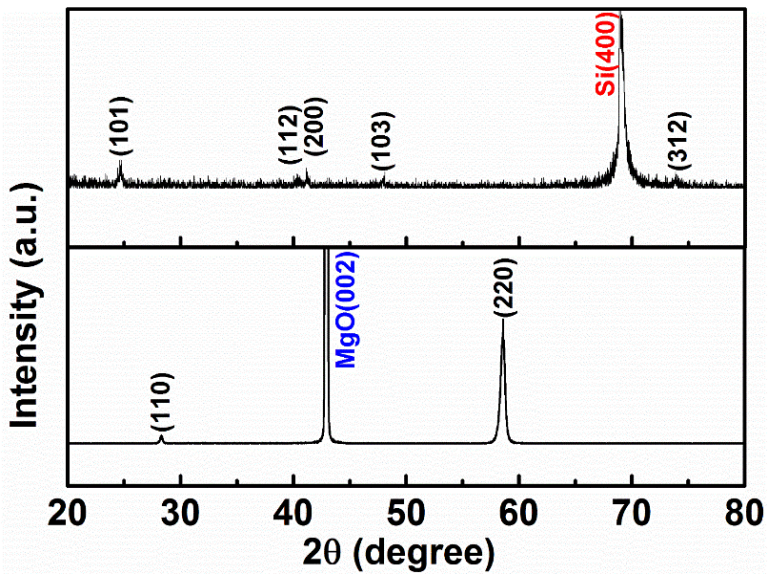

FIG. 4. 1 Out of plane XRD pattern of epitaxial Mn_2PtSn film on (a) Si (100) substrate, and (b) MgO (001) substrate.

Nevertheless, to establish the single crystalline properties and structure of the film, pole Figures, capillary diffraction and in-plane grazing incidence diffraction experiments were carried out. FIG. 4.2 shows the pole-Figure plots for the [111] planes relative to the (100) plane of MgO, respectively. These plots confirm the high degree of epitaxial crystallinity of the film deposited on MgO and establish the orientation relationship between the crystallographic axes in the film plane. The pole-plot intensities have maxima at 45°, and exhibit 4-fold symmetry, providing clear evidence that the Mn_2PtSn films grown on MgO are single-crystalline with the cubic crystal structure. Moreover, the azimuthal angles mean that MgO [100] and Mn_2PtSn [111] are parallel and that Mn_2PtSn [001] is rotated by 36° away from MgO [100]. The lattice parameters of Mn_2PtSn, a = 0.4488 nm, and b = 0.6148 nm indicate significant lattice mismatch between the ordered Mn_2PtSn film and the MgO substrate (a = 0.421 nm). This situation is similar to the epitaxial growth of Fe film on MgO, where the rotation of the over layer unit cell by 45° favors epitaxial growth.[23] However, it is different with the Mn_2RhSn film on MgO (001), which shows that [001] is out of plane and parallel to MgO [001].[17]

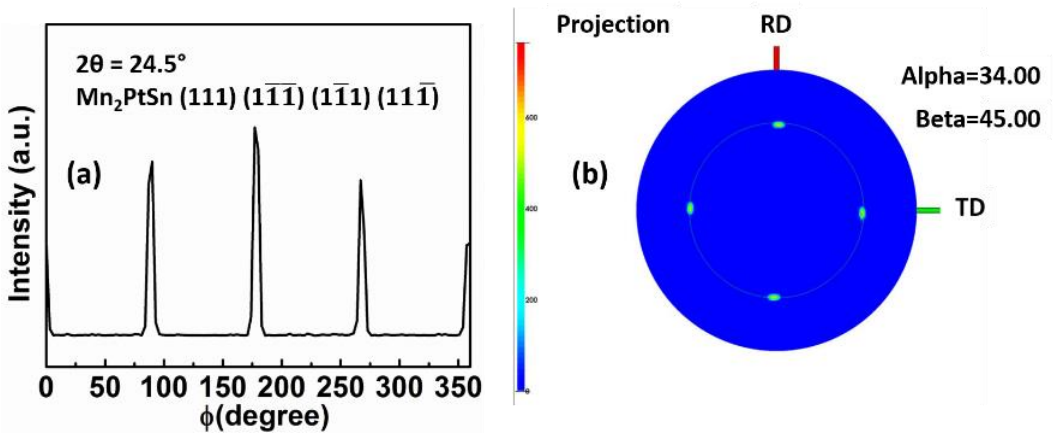

FIG. 4. 2 Pole-Figure plots of Mn_2PtSn films deposited on MgO (001): (a) ϕ scan for (111) diffraction (2θ = 24.5°), and (b) The [111] pole-Figure shows the epitaxy and four-fold in-plane symmetry of the films.

FIG. 4.3 shows intensity profiles extracted for (112) and (020) peaks with an appropriate tilt of the sample (χ = 45°), with respect to the surface normal. In this kind of measurement, a certain set of (112) and (020) planes is selected, which means d_{112} and d_{020} are selected by fixing the detector (2θ) and incident beam (θ) angle. Diffraction will only occur if the normal **N** to the selected (112) and (020) planes is parallel to the diffraction vector. Therefore, the sample has to be tilted to χ = 45° for (112) and (020) planes, and the intensity at each point in the obtained pattern (FIG. 4.3) is proportional to the number of grains in the film that have their normal to the selected (112) and (020) planes. For a random orientation of the grains in the thin film, the pattern will be featureless and show a polycrystalline ring. No preferred orientation for the normal to the (112) and (020) planes is observed. For an epitaxial thin film, only one grain orientation will be present in the film and the Figure is characterized by a small and strong spot. As

shown in FIG. 4.3, two strong neighboring spots at the peak positions of 40° and 41° indicate an epitaxial growth of Mn_2PtSn film and the peaks positions are consistent with the peak positions of (112) and (020) planes of the simulated pattern of inverse tetragonal structure Mn_2PtSn (space group I-4m2, no 119).

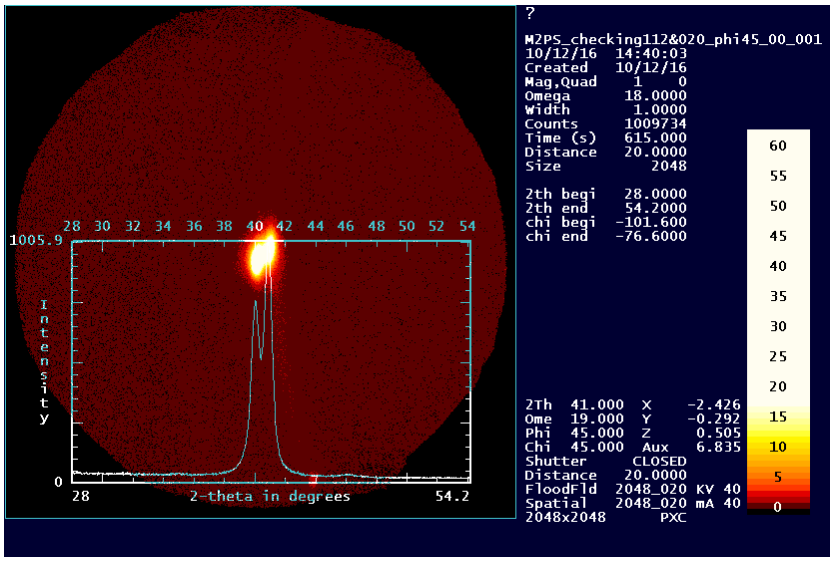

FIG. 4. 3 Intensity profiles extracted for (112) and (020) peaks with an appropriate tilt of the sample (χ = 45°), with respect to the surface normal.

In order to confirm the epitaxial growth of Mn_2PtSn film on MgO and the structural properties analyzed by XRD, we conducted a TEM analysis. As shown in FIG. 4.4, the TEM image shows that the thickness of Mn_2PtSn film is about 90 nm and Al cap layer is about 5 nm, which are very close to the calculated thickness based on the deposition rate calibrated by the AJA system.

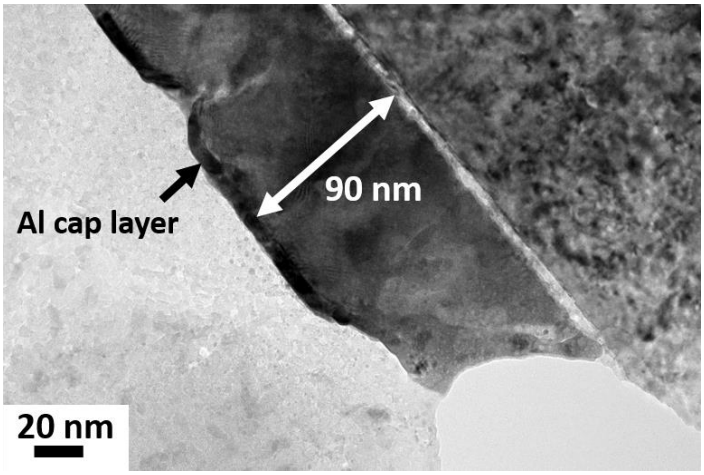

FIG. 4.4 TEM image of both Mn_2PtSn film and MgO substrate.

FIG. 4.5 shows the SAED pattern of both Mn_2PtSn film and MgO substrate, and a corresponding index of Mn_2PtSn [111] axis (red color) and MgO [001] axis (blue color). The lattice constants *a* and *b* were determined to be 0.4488 nm and 0.6148 nm, respectively, by measuring the separation d_{hkl} (*h*, *k*, *l* are Miller indices) between parallel reflection planes d_{111} and d_{002} from the SAED patterns. This finding is consistent with XRD results. In addition, we found that MgO [100] and Mn_2PtSn [111] are parallel and that Mn_2PtSn [001] is rotated by 36° away from MgO [100]. The lattice parameters of Mn_2PtSn, a = 0.4488 nm, and b = 0.6148 nm indicate significant lattice mismatch between the ordered Mn_2PtSn film and the MgO substrate (a = 0.421 nm). In fact, the lattice spacing d_{100} of MgO is comparable to d_{111} of Mn_2PtSn, with a strain of about 3.6 %.

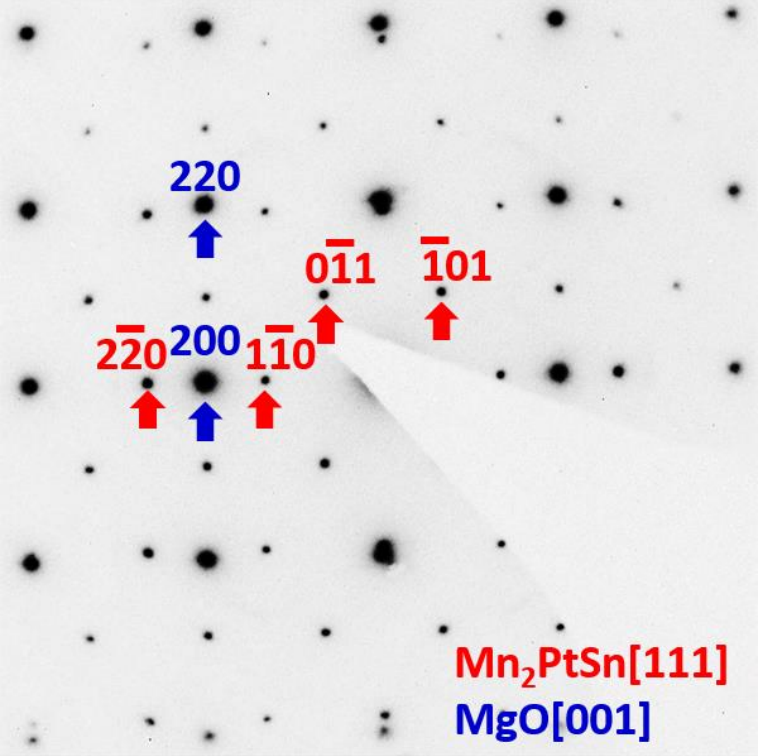

FIG. 4. 5 SAED pattern of both Mn_2PtSn film and MgO substrate, and corresponding index of Mn_2PtSn [111] axis (red color) and MgO [001] axis (blue color).

FIG. 4.6 shows unit cell of the inverse-tetragonal structure of Mn_2PtSn with space group I-4m2, No 119. Wyckoff positions are Mn1, (0, 1/2, 1/4), Mn2, (0, 0, 1/2), Pt, (0,1/2, 3/4), Sn, (0, 0, 0). High-resolution TEM observation of the interface between Mn_2PtSn film [111] and MgO substrate [001] is shown in FIG. 4.7 (a), which reveals the epitaxial growth of Mn_2PtSn film onto MgO (001). FIG. 4.7 (b) shows the unit cell of inverse tetragonal Mn_2PtSn with [111] axis normal to paper. The pink plane is (111) plane with 3 Sn atoms in the plane of the unit cell. Besides, the HRTEM image in FIG. 4.7 (a) clearly shows the atomic columns of MgO (001) plane and Mn_2PtSn (111) plane as indicated by the colored balls. The composition of the films was investigated to be $Mn_{47.5}Pt_{25.2}Sn_{27.3}$ using energy-dispersive x-ray spectroscopy (EDX) in TEM.

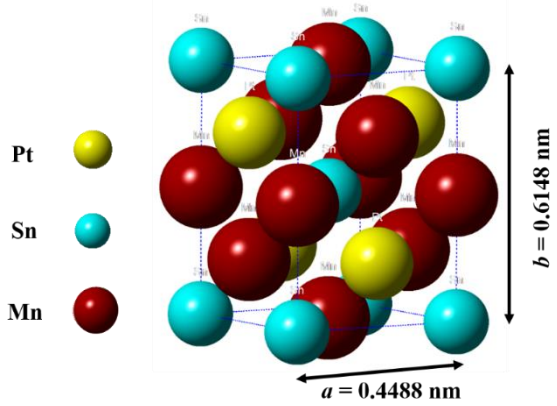

FIG. 4. 6 Unit cell of the inverse-tetragonal structure of Mn_2PtSn.

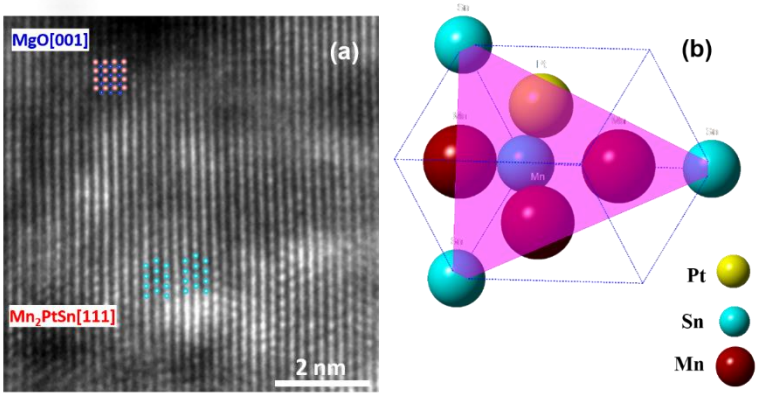

FIG. 4. 7 (a) High-resolution TEM image of the interface between Mn_2PtSn film [111] and MgO substrate [001]. (b) The unit cell of inverse tetragonal Mn_2PtSn with [111] axis normal to paper. The color plane (pink) is (111) plane with 3 Sn atoms in the plane of the unit cell.

4.4 Magnetic Properties

FIG. 4.8 (a) shows isothermal magnetization curves M(H) of an epitaxial Mn_2PtSn film recorded at 5 K and 300 K with the magnetic field applied in the film plane and isothermal magnetization curves M(H) with a magnetic field applied out of the plane in (b). The films have in-plane anisotropy with coercivities being around 4 kOe at 5 K and 1

kOe at 300 K with a magnetic field applied in the film plane. For the magnetic field applied out of the film plane, the coercivities are around 100 Oe at 5 K and 50 Oe at 300 K. The saturation magnetization M_s (800 emu/cm^3) is 3.2 μ_B / f. u., which is lower than the value (4.0 μ_B / f. u.) predicted by the Slater-Pauling curve for the half-metallic phase of Mn_2PtSn compound.[21] At 5 K, the anisotropic field (H_a) is around 20 kOe from FIG. 4.8 (a) and (b). $J_s = 4\pi M_s$ = 10 kOe. The anisotropy field H_a is defined as the field needed to saturate the magnetization of a uniaxial crystal in a hard direction,

$$E = K_u sin^2\theta - M_s H cos(\pi/2 - \theta).^{24, 25} \qquad [4.1]$$

Minimizing E, $\partial E/\partial\theta = 0$ and setting $\theta = \pi/2$,

$$H_a = 2K_u/M_s. \qquad [4.2]$$

Since at 5 K, J_s = 10 kOe, H_a is around 20 kOe. The derived K_u is about 10 Merg/cm^3 at 5 K for Mn_2PtSn film, which is lower than the theoretical calculation of effective anisotropy constant 50 Merg/cm^3.[20] The reduction of in-plane anisotropy of Mn_2PtSn film from 5 K to 300 K are due to temperature increase results in harm to anisotropy constant. The rapid decrease of in-plane anisotropy at room temperature attributed to Curie temperature being slightly above room temperature as shown in FIG. 4.9 (b). FIG. 4.9 (a) shows thermomagnetic curve M(T) of the epitaxial Mn_2PtSn film measured at 1.0 kOe, where the magnetization gradually decreases. As compared to the magnetic properties of bulk Mn_2PtSn, epitaxial Mn_2PtSn films on MgO has been realized a large in-plane anisotropy due to the epitaxial growth of Mn_2PtSn films.

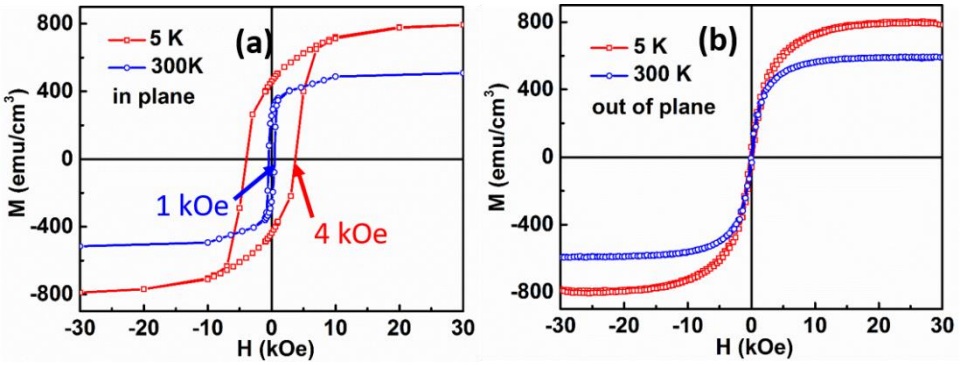

FIG. 4. 8 Field dependence of magnetization M(H) loops of epitaxial Mn_2PtSn films at 5 K and 300 K with a magnetic field applied in the plane (a), and out of the plane (b).

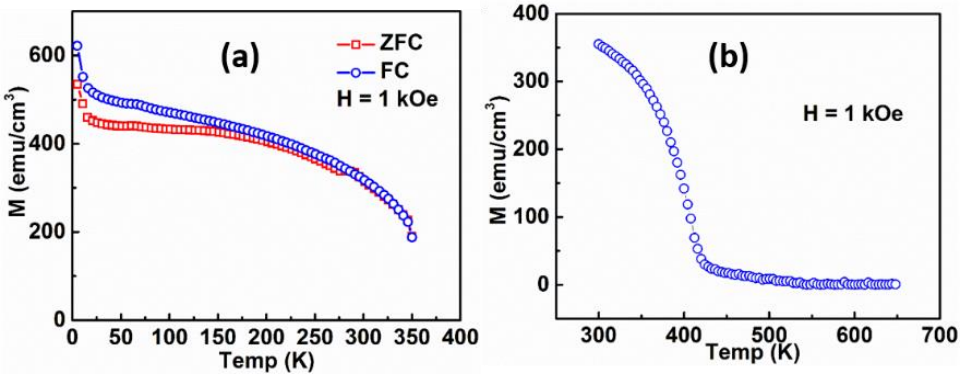

FIG. 4. 9 (a) Low, and (b) high temperature dependence of magnetization of epitaxial Mn_2PtSn films with magnetic field H = 1 kOe applied out of the plane.

4.5 Transport Properties

FIG. 4.10 shows temperature dependence of the zero-field longitudinal resistivity ρ_{xx} of epitaxial films, where ρ_{xx} has an approximately linear increase with increasing temperature up to 300 K, showing a metallic behavior. The residual resistivity ρ_0 of 250 μΩcm is caused by defects in the ideal crystal lattice. However, the temperature

dependence of the zero-field longitudinal resistivity ρ_{xx} obeys a power law T^3 below 50 K, which is experimentally found in other half-metallic ferromagnets[26, 27]. Moreover, the formula $\rho = \rho_0 + AT^2 e^{-\Delta/T}$ may fit the temperature-dependent resistivity of half-metallic ferromagnets as well, where ρ_0 is the residual resistivity and Δ is the critical temperature switching from half-metal to normal metal.[28] The second quadratic magnonic term related to electron-magnon scattering is expected to be exponentially suppressed due to the gapped spin-flip scattering. The parameter Δ is a measure of the strength of the magnon scattering process. A fitting parameter Δ of 50 K is obtained. The observed exponential suppression of spin-flip scattering confirms clear HMF behavior. However, the unexpectedly small extracted value of Δ = 50 K implies that perfect spin polarization of the electrons at the Fermi level is present only for $T < \Delta$. Besides, considering the phononic contribution, the temperature-dependent resistivity of Mn_2PtSn may be fitted by the Bloch-Gruneisen formula to evaluate the phononic contribution of the scattering process.[29] This fitting may be done once the Debye temperature is obtained by specific heat measurement.

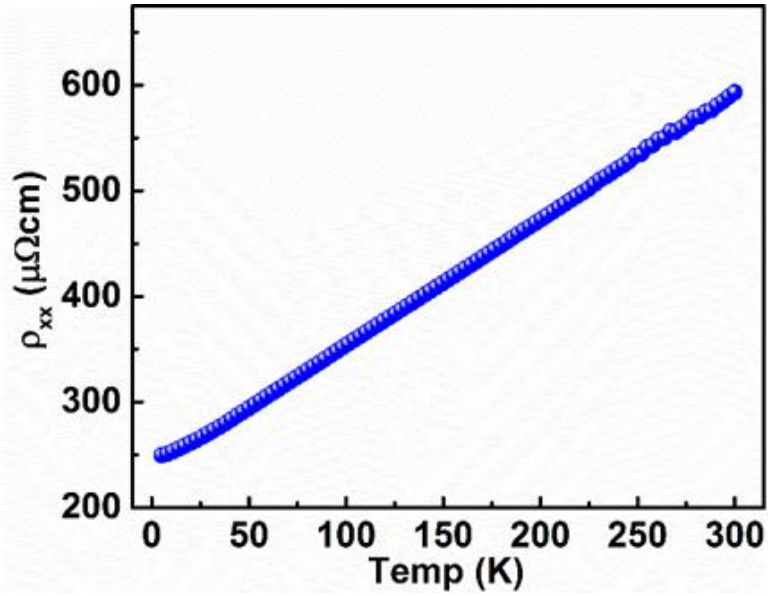

FIG. 4. 10 Longitudinal resistivity of Mn_2PtSn film as a function of temperature with a zero magnetic field.

FIG. 4.11 shows the magnetic field dependence of Hall resistivities $\rho_{xy}(H)$ of Mn_2PtSn films measured at 5 K, 10 K, 30 K, and 300 K. The $\rho_{xy}(H)$ curves are nonlinear at all temperatures and look similar in shape to the corresponding $M(H)$ curves. The ρ_{xy} can be expressed as $\rho_{xy}(H,T) = R_0 \cdot H + R_A \cdot M(H)$, where the first term depends on the external magnetic field (ordinary Hall resistivity) and the second term depends on the magnetization of the film (anomalous Hall resistivity).[30, 31] The coefficients R_0 and R_A in the expression are, respectively, the ordinary Hall coefficient and anomalous Hall coefficient. These coefficients can be determined by extrapolating the high-field portion of $\rho_{xy}(H)$ curve to H = 0, where the slope and intercept of the line are equal to R_0 and R_A M(0), respectively, with M(0) being saturation magnetization. As mentioned in other chapters, the anomalous Hall coefficient R_A follows a simple power law on longitudinal

resistivity ρ_{xx} of the form $R_A \propto (\rho_{xx})^m$ depending on the scattering mechanism, where m = 1 for skew-scattering and m = 2 for intrinsic plus side jump scattering and can be expressed as $R_A = a\rho_{xx} + b\rho_{xx}^2$. The constants a and b contain information about the skew-scattering and intrinsic (Berry phase) plus side jump scattering mechanisms.[31] As shown in the FIG. 4.12, we have plotted $\rho_{xy}(0)$ at various temperature as a function of ρ_{xx}^2 at the corresponding temperatures and found a linear relationship for both the films. This indicates that the side-jump (plus intrinsic) mechanism is responsible for the observed anomalous Hall-effect in epitaxial Mn_2PtSn films.

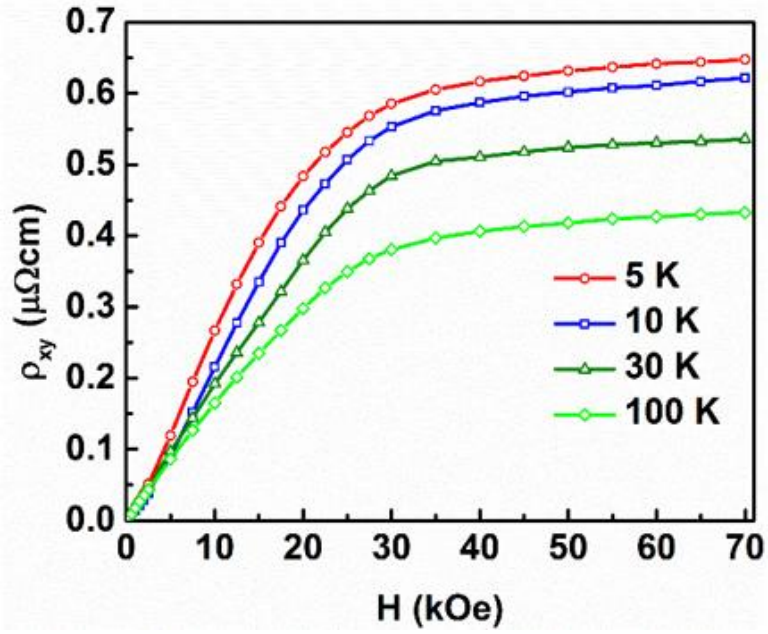

FIG. 4. 11 Hall-effect of Mn_2PtSn film measured at various temperatures with a magnetic field applied out of the plane.

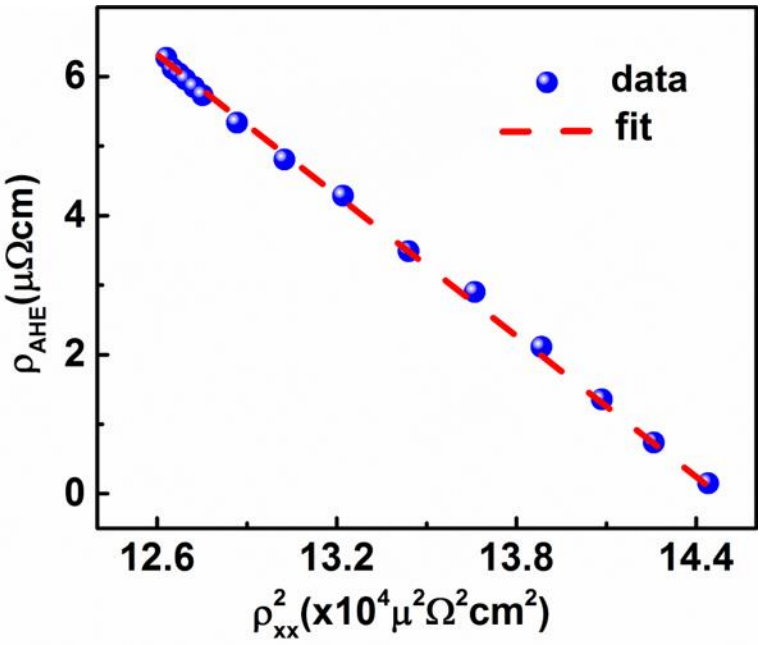

FIG. 4. 12 Anomalous Hall-effect coefficients at various temperature as a function of ρ_{xx}^2 at the corresponding temperatures and a linear fit (red dash line).

FIG. 4.13 shows the magneto-resistivity (MR) as a function of the magnetic field of Mn_2PtSn films measured at various temperatures 5 K, 10 K, 30 K, and 300 K with magnetic field perpendicular to the film plane. The MR was derived from the resistivity (ρ_{xx}) with and without a magnetic field as

$$MR = (\rho_{xx}^{7\,T} - \rho_{xx}^{0\,T})/\rho_{xx}^{0\,T} * 100\% \leq 0.5\%. \qquad [4.3]$$

The MR values of the epitaxial film are below 1.0 % and saturated up to 70 kOe. MR exhibits the conventional behavior as in most ferromagnets. The slope of the MR(H) curves changes abruptly near 30 kOe, which is more obvious for the low-temperature measurements. This is presumed to be due to strong spin-orbit scattering at the weak field but as field increases the magnetic scattering becomes dominant. In the low magnetic

field below 25 kOe, the resistance changes rapidly and the MR curve is nonlinear. In high field of magnetic saturation (≥ 25 kOe), the changes in rate of resistance become slow and exhibit a linear trend and approaching saturation. The negative MR can be attributed to the reduction of random spin-flip scattering process as the field aligns the magnetic moments, which is expected to increase as temperature decreases. Similar MR behavior has been reported for both the bulk and thin-film samples of another SGS compound Mn_2CoAl,[3, 4] the MR of which is positive at low temperatures and changes to negative with increasing temperature, and Fe_2CoSi.[32]

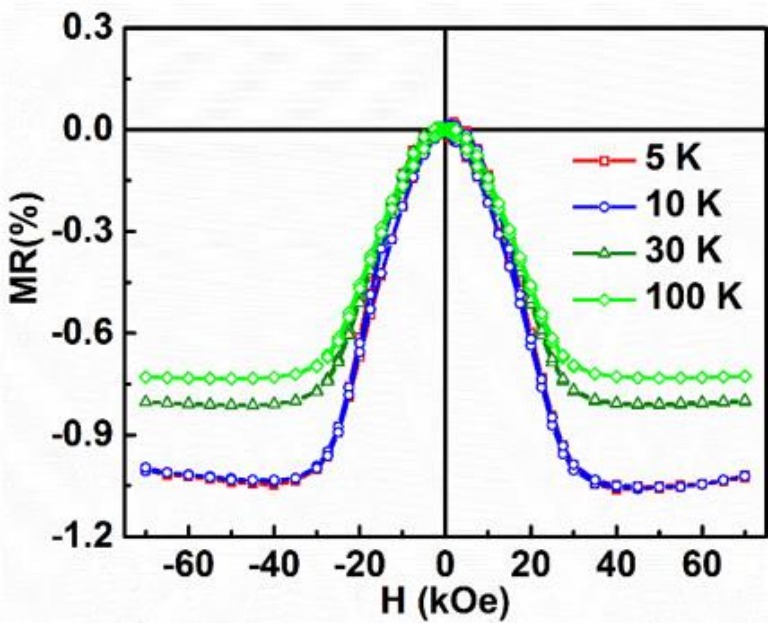

FIG. 4. 13 Field dependence of magneto-resistivity (MR) of Mn_2PtSn film for various temperatures with a magnetic field applied out of the plane.

4.6 Summary

In summary, the structural, magnetic and electron transport properties of thin films of a Heusler compound Mn_2PtSn have been investigated. Structural analysis shows the

structure of epitaxial Mn_2PtSn film is inverse tetragonal with lattice constants a = 0.4488 nm, and b = 0.6148 nm (space group I-4m2, No. 119). Lattice constants have a very small mismatch with MgO, which makes it promising for coherent electron tunneling phenomena. Measured saturation magnetization is 3.2 μ_B/f.u. is less than that calculated from the density of states. The magnetization measurements revealed an in-plane anisotropy energy of 10 Merg/cm^3. The magnetoresistance ratio is 1.0 % with a magnetic field applied out of the plane. Curie temperature is around 410 K, which is higher than room temperature allowing for high-temperature spintronics application. Longitudinal resistivity shows a linear and positive TCR, confirmed the metallic behavior. Hall-effect measurements indicate the side-jump mechanism contributes to the electron transport. Such half-metallic magnetic films with the advantages of strong in-plane magnetocrystalline anisotropy and proper thickness might be used in spin valves or magnetic tunnel junctions as high-performance magnetic memory elements.

4.7 Bibliography

1. Y. Sakuraba and K. Takanashi, in *Heusler Compounds: Properties, Growth, Applications*, edited by C. Felser and A. Hirohata (Springer International Publishing, Cham, 2016), pp. 389-400.

2. L. Ritchie, G. Xiao, Y. Ji, T. Y. Chen, C. L. Chien, M. Zhang, J. Chen, Z. Liu, G. Wu and X. X. Zhang, "Magnetic, structural, and transport properties of the Heusler compounds Co_2MnSi and NiMnSb", Physical Review B **68**, 104430 (2003).

3. S. Ouardi, G. H. Fecher, C. Felser and J. Kübler, "Realization of spin-gapless semiconductors: The heusler compound Mn_2CoAl", Physical Review Letters **110**, 100401 (2013).

4. G. Z. Xu, Y. Du, X. M. Zhang, H. G. Zhang, E. K. Liu, W. H. Wang and G. H. Wu, "Magneto-transport properties of oriented Mn_2CoAl films sputtered on thermally oxidized Si substrates", Applied Physics Letters **104**, 242408 (2014).

5. A. Nayak, M. Nicklas, S. Chadov, C. Shekhar, Y. Skourski, J. Winterlik and C. Felser, "Large zero-field cooled exchange-bias in bulk Mn_2PtGa", Physical review letters **110**, 127204 (2013).

6. A. D. Kent, B. Özyilmaz and E. del Barco, "Spin-transfer-induced precessional magnetization reversal", Applied Physics Letters **84**, 3897-3899 (2004).

7. K. J. Lee, O. Redon and B. Dieny, "Analytical investigation of spin-transfer dynamics using a perpendicular-to-plane polarizer", Applied Physics Letters **86**, 022505 (2005).

8. S. Mangin, D. Ravelosona, J. A. Katine, M. J. Carey, B. D. Terris and E. E. Fullerton, "Current-induced magnetization reversal in nanopillars with perpendicular anisotropy", Nature Materials **5**, 210-215 (2006).

9. C. Chappert, A. Fert and F. N. Van Dau, "The emergence of spin electronics in data storage", Nature Materials **6**, 813-823 (2007).

10. A. Hirohata, J. Sagar, L. R. Fleet and S. S. P. Parkin, in *Heusler Compounds: Properties, Growth, Applications*, edited by C. Felser and A. Hirohata (Springer International Publishing, Cham, 2016), pp. 219-248.

11. C. Felser, L. Wollmann, S. Chadov, G. H. Fecher and S. S. P. Parkin, in *Heusler Compounds: Properties, Growth, Applications*, edited by C. Felser and A. Hirohata (Springer International Publishing, Cham, 2016), pp. 37-48.

12. C. Felser, G. H. Fecher and B. Balke, "Spintronik: eine Herausforderung für Materialwissenschaften und Festkörperchemie", Angewandte Chemie **119**, 680-713 (2007).

13. R. Kainuma, Y. Imano, W. Ito, Y. Sutou, H. Morito, S. Okamoto, O. Kitakami, K. Oikawa, A. Fujita, T. Kanomata and K. Ishida, "Magnetic-field-induced shape recovery by reverse phase transformation", Nature **439**, 957-960 (2006).

14. T. Krenke, E. Duman, M. Acet, E. F. Wassermann, X. Moya, L. Manosa and A. Planes, "Inverse magnetocaloric effect in ferromagnetic Ni-Mn-Sn compounds", Nat Mater **4**, 450-454 (2005).

15. I. Takeuchi, O. O. Famodu, J. C. Read, M. A. Aronova, K. S. Chang, C. Craciunescu, S. E. Lofland, M. Wuttig, F. C. Wellstood, L. Knauss and A. Orozco,

"Identification of novel compositions of ferromagnetic shape-memory compounds using composition spreads", Nature Materials **2**, 180-184 (2003).

16. S. Chadov, X. Qi, J. Kübler, G. H. Fecher, C. Felser and S. C. Zhang, "Tunable multifunctional topological insulators in ternary Heusler compounds", Nature Materials **9**, 541-545 (2010).

17. M. Olga, K. Albrecht, O. Siham, K. Yukio, K. Takahide, C. Shekhar, K. Julie, V. B. Carlos, S. Rolf, S. Roshnee, U. Shigenori, I. Eiji, M. Shigemi, C. Stanislav, E. Daniel, H. F. Gerhard and F. Claudia, "Structural, electronic, and magnetic properties of perpendicularly magnetised Mn_2RhSn thin films", Journal of Physics D: Applied Physics **48**, 164008 (2015).

18. O. Meshcheriakova, S. Chadov, A. K. Nayak, U. K. Rößler, J. Kübler, G. André, A. A. Tsirlin, J. Kiss, S. Hausdorf, A. Kalache, W. Schnelle, M. Nicklas and C. Felser, "Large Noncollinearity and Spin Reorientation in the Novel Mn2RhSn Heusler Magnet", Physical Review Letters **113**, 087203 (2014).

19. H. Kurt, K. Rode, M. Venkatesan, P. Stamenov and J. M. D. Coey, "High spin polarization in epitaxial films of ferrimagnetic Mn_3Ga", Physical Review B **83**, 020405 (2011).

20. J. Winterlik, S. Chadov, A. Gupta, V. Alijani, T. Gasi, K. Filsinger, B. Balke, G. H. Fecher, C. A. Jenkins, F. Casper, J. Kübler, G.-D. Liu, L. Gao, S. S. P. Parkin and C. Felser, "Design scheme of new tetragonal heusler compounds for spin-transfer torque applications and its experimental realization", Advanced Materials **24**, 6283-6287 (2012).

21. J. Kübler and C. Felser, "Berry curvature and the anomalous Hall-effect in Heusler compounds", Physical Review B **85**, 012405 (2012).

22. Y. Huh, P. Kharel, A. Nelson, V. R. Shah, J. Pereiro, P. Manchanda, A. Kashyap, R. Skomski and D. J. Sellmyer, "Effect of Co substitution on the magnetic and electron-transport properties of Mn_2PtSn", Journal of Physics: Condensed Matter **27**, 076002 (2015).

23. A. Nelson, Y. Huh, P. Kharel, V. R. Shah, R. Skomski and D. J. Sellmyer, "Structural, magnetic, and electron transport properties of $Mn_{3-x}Pt_xSn$ (x = 0, 0.5, 1) nanomaterials", Journal of Applied Physics **115**, 17A923 (2014).

24. R. Skomski, "Simple Models of Magnetism" 1st edition ed. (Oxford University Press, 2008).

25. J. M. D. Coey, "Magnetism and Magnetic Materials" 1 edition ed. (Cambridge University Press, Trinity College, Dublin, 2010).

26. K. K. a. O. N., "", J. Phys. Soc. Jpn. **33**, (1972).

27. F. N., "", J. Phys. Soc. Jpn. **69**, (2000).

28. S. M. Watts, S. Wirth, S. von Molnár, A. Barry and J. M. D. Coey, "Evidence for two-band magnetotransport in half-metallic chromium dioxide", Physical Review B **61**, 9621-9628 (2000).

29. D. Bombor, C. G. F. Blum, O. Volkonskiy, S. Rodan, S. Wurmehl, C. Hess and B. Büchner, "Half-metallic ferromagnetism with unexpectedly small spin splitting in the heusler compound Co_2FeSi", Physical Review Letters **110**, 066601 (2013).

30. Y. Tian, L. Ye and X. Jin, "Proper scaling of the Anomalous Hall-effect", Physical Review Letters **103**, 087206 (2009).

31. N. Nagaosa, J. Sinova, S. Onoda, A. H. MacDonald and N. P. Ong, "Anomalous Hall-effect", Reviews of Modern Physics **82**, 1539-1592 (2010).

32. Y. Du, G. Z. Xu, X. M. Zhang, Z. Y. Liu, S. Y. Yu, E. K. Liu, W. H. Wang and G. H. Wu, "Crossover of magnetoresistance in the zero-gap half-metallic Heusler compound Fe $_2$CoSi", EPL (Europhysics Letters) **103**, 37011 (2013).

Table of Contents

Chapter 5. Structural and Magnetic Properties of Heusler CoFeCrX (X = Si, Ge) Compounds.

This chapter discusses the structural, electronic, and magnetic properties of CoFeCrX (X = Si, Ge) Heusler compounds. Experimentally, the compounds were synthesized in the cubic $L2_1$ structures with small disorder. The cubic phase of CoFeCrSi was found to be highly stable against heat treatment, but CoFeCrGe discomposed into other phases when the temperature reached 402 ^{o}C (675 K). A new tetragonal CoFe-rich structure with lattice parameters a = 0.76 nm, c = 0.284 nm, was found embedded in the matrix of the Cr_3Ge phase, but there is no special orientation between the two phases. Both CoFeCrSi and CoFeCrGe compounds showed ferrimagnetic spin order at room temperature, and have Curie temperatures significantly above room temperature. The measured T_C for CoFeCrSi is 790 K but that of CoFeCrGe could not be measured due to its dissociation into other phases at 675 K. The saturation magnetizations of CoFeCrSi and CoFeCrGe are 2.82 μ_B/f.u. and 2.78 μ_B/f.u., respectively, which are close to the theoretically predicted value of 3 μ_B/f.u. for their half-metallic phases. These materials have the potential for spintronic device applications, as they exhibit half-metallic electronic structures with large band gaps, and Curie temperatures significantly above room temperature.

Many of the results presented in this chapter are adapted from the publication and manuscript:

Y. Jin, P. Kharel, P. Lukashev, S. Valloppilly, B. Staten, J. Herran, I. Tutic, M. Mitrakumar, B. Bhusal, A. Connell, K. Yang, Y. Huh, R. Skomski and D. J. Sellmyer,

"Magnetism and electronic structure of CoFeCrX (X = Si, Ge) Heusler alloys". Journal of Applied Physics **120**, 053903 (2016).

Y. Jin, X. Li, D. J. Sellmyer, "A new tetragonal phase in CoFeCrGe Heusler alloy" (to be submitted to Materials Characterization).

I performed the synthesis and characterization of the samples. S. R. Valloppilly, X. Li, P. Kharel assisted with XRD measurements, TEM measurement and revising the manuscripts, respectively. P. Lukashev performed the first-principle calculation, R. Skomski helped with discussion and revising the manuscript. All co-authors contributed to the final manuscripts.

5.1 Introduction

Magnetic materials that conduct electrons of only one spin orientation have a great potential in spintronic devices. These materials include half-metallic ferro-, ferri-, and antiferromagnets.[1-7] Since the electronic band structure of half-metals is metallic for one spin channel and insulating for the opposite spin channel, they are in principle capable of producing 100% spin-polarized current. For practical device applications, these materials need to show robust half-metallicity at room temperature, which is possible in ferro- or ferrimagnetic materials having high Curie temperature, ideally far above room temperature.[8] Another factor responsible for the robustness of the half-metallic property is the size of the band gap because materials having small band gap are likely to lose their half-metallic properties if their crystal lattice is slightly strained in thin films.[9] Recent theoretical and experimental studies have indicated that several Heusler compounds with cubic or tetragonal crystal structures, especially, Mn- and Co-based

materials, have shown half-metallic band structures with promise for spintronic applications, e.g., in spin transfer torque (STT)-based memories.[10-14]

Heusler compounds include a wide range of interesting materials such as half-metallic magnets, high perpendicular-magnetic-anisotropy materials, shape-memory compounds, spin-gapless semiconductors, skyrmions, topological insulators, and magnetocaloric.[15-18] The completely ordered full Heusler compounds (X_2YZ; X and Y are transition-metal elements, and Z are main-group elements) crystallize in the cubic $L2_1$ structure (prototype Cu_2MnAl). However, many of the synthesized Heusler compounds are found to crystallize either with partially disordered B2-type (half of the Y and Z atoms interchange their positions) or fully disordered A2-type (X, Y, and Z atoms are randomly distributed at all available lattice sites) phases losing their half-metallic properties.[19, 20] Further, the ordered quaternary Heusler compounds XX′YZ, where X′ is also a transition-metal element, crystallize in Y structure (prototype LiMgPdSn).[21] Recent studies have shown that several of these quaternary Heusler compounds exhibit either half-metallic or spin-gapless semiconducting properties.[16, 22]

In this chapter, we focus on experimental and theoretical investigations of two quaternary compounds CoFeCrSi and CoFeCrGe. Our interest in these compounds stems from a recent theoretical prediction that both of these materials have relatively large half-metallic band gaps and high Curie temperatures significantly above room temperature.[9] Here, we present our experimental investigation of the structural and magnetic properties of CoFeCrSi and CoFeCrGe compounds and compare the experimental data with results of the first-principle calculations. We found that CoFeCrSi compound exhibits very high Curie temperature (T_C = 790 K) but CoFeCrGe decomposed into other phases near 675

K. The compositions and structures of the crystalline phases in the annealed samples were systematically characterized by transmission-electron microscopy (TEM), energy-dispersive X-ray spectroscopy (EDS), selected-area electron diffraction (SAED), and high-resolution electron image (HREM) experiments. The structural properties of the new tetragonal CoFe-rich phase will be discussed.

5.2 Experimental Details

CoFeCrSi and CoFeCrGe compounds in the form of ribbons were prepared using arc melting, rapid quenching, and annealing. To investigate the effect of heat treatment on the structural and magnetic properties, the samples were annealed in a vacuum (10^{-7} Torr) at various temperatures for 4 hours between 300 ºC and 600 ºC. The crystal structures of the samples were investigated using powder XRD in Rigaku Miniflex and PANalytical Empyrean diffractometers with copper Kα radiation. Magnetic properties were investigated with a Quantum Design VersaLab magnetometer and Physical Properties Measurement system (PPMS). The phase distribution (elemental compositions) of various grains in the samples was investigated using an FEI Tecnai Osiris TEM. TEM specimens were prepared by grinding the ribbons into fine powders in ethanol solution and then dropped onto a Cu grid with C film. TEM experiments were carried out on a FEI Tecnai Osiris (scanning) transmission electron microscope, which operates at 200 kV and is equipped with a double-tilt holder. The EDS data were collected with the ChemiSTEM system on the Osiris microscope and analyzed with Bruker's ESPRIT software. The experimental SAED patterns were analyzed using LANDYNE software.[23, 24]

5.3 XRD Structural Analysis

The room temperature XRD patterns of the powder samples prepared from ribbons of CoFeCrSi annealed at 450 ^{o}C for 4 hours and the simulated patterns and the difference curves obtained from Rietveld analysis are shown in FIG. 5.1. The XRD pattern in FIG. 5.1 agrees well with the patterns simulated for the cubic $L2_1$ structures of the corresponding compounds. The lattice constants *a* obtained from the refinement of the XRD patterns of the cubic CoFeCrSi is 5.69 Å. The room temperature XRD pattern of the powder sample prepared from ribbons of CoFeCrGe annealed at 300 ^{o}C for 4 hours and the simulated patterns and the difference curves obtained from Rietveld analysis are shown in FIG. 5.2. The XRD pattern in FIG. 5.2 agrees well with the patterns simulated for the cubic $L2_1$ structures of the corresponding compounds. The lattice constants *a* obtained from the refinement of the XRD patterns of the cubic CoFeCrGe is 5.78 Å. Both CoFeCrSi and CoFeCrGe have mainly the ordered $L2_1$ structures, but a small amount of Cr/Si or Cr/Ge site exchange similar to a partial B2-type disorder has been found by XRD simulations. It is worth noting that the presence of (111) and (002) reflections are the signatures for the $L2_1$ structural ordering that distinguishes itself from the B2-type. In a fully ordered $L2_1$ structure, a strong scattering contrast between Si and the transition metal elements and a weak scattering contrast between Ge and the transition metals can be clearly distinguished from the strong and weak intensities of both (111) and (002) Bragg reflections in the simulations. This can be seen in the XRD patterns simulated for CoFeCrSi and CoFeCrGe as shown in FIGs. 5.1 and 5.2, respectively. However, a partial B2-type disorder in CoFeCrSi was determined by modeling the intensities in the Rietveld analysis. It has been estimated that about 17% of Cr and Si exchange their positions in

the Cubic CoFeCrSi. In the low temperature (300 ^{o}C) annealed CoFeCrGe sample, the simulated pattern with the $L2_1$ order matches very closely with the experimental data making it difficult to determine the B2-type disorder.

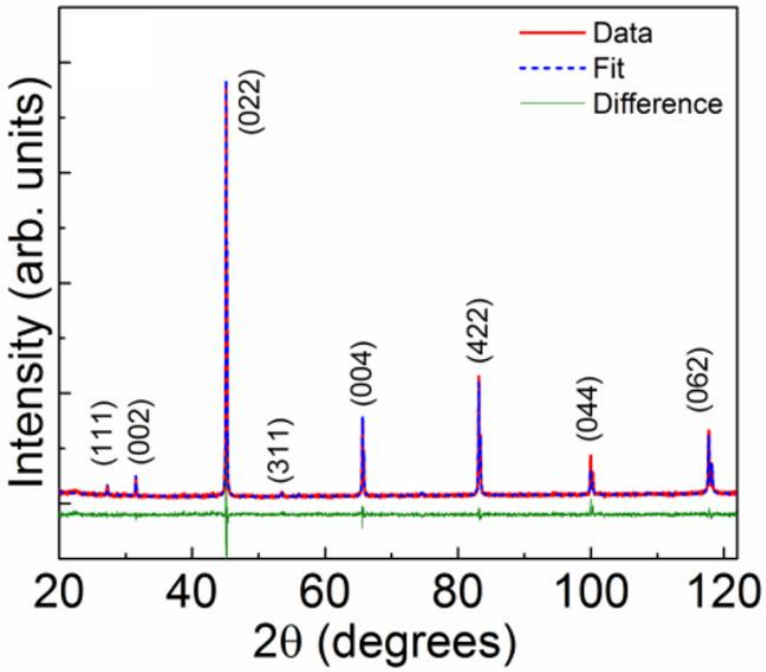

FIG. 5. 1 Room temperature powder XRD pattern of CoFeCrSi ribbon annealed at 450 ^{o}C for 4 hours.

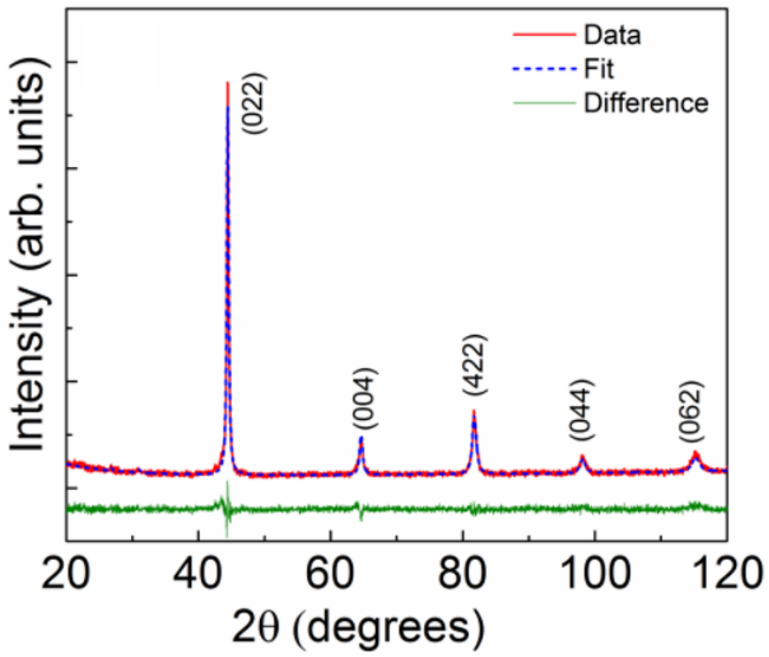

FIG. 5. 2 Room temperature powder XRD pattern of CoFeCrGe ribbons annealed at 300 ^{o}C for 4 hours.

The room temperature XRD pattern of the powder sample prepared from ribbons of CoFeCrGe annealed at 500 ^{o}C for 4 hours and the simulated patterns and the difference curves obtained from Rietveld analysis are shown in FIG. 5.3. The XRD pattern of CoFeCrGe annealed at 500 ^{o}C contains several additional peaks which cannot be indexed with its cubic $L2_1$ structure. However, all of these peaks can be fully indexed if the sample is assumed to contain two additional compounds with structures similar to those of Co_2FeGe and Cr_3Ge. This indicates that CoFeCrGe disintegrates into other compounds if annealed at 500 ^{o}C. The phase identification of these compounds as obtained from the Rietveld analysis are Co-rich $(Co, Fe, Cr)_2FeGe$ and Cr-rich $(Cr, FeCo)_3Ge$. The primary compound Co-rich $(Co, Fe, Cr)_2FeGe$ is the mixture of an ordered $L2_1$ structure with a =

0.571 nm and a B2 structure with a = 0.286 nm. The secondary phase is the Cr-rich (Cr, Fe, Co)$_3$Ge phase with a = 0.46127 nm.

This result is also supported by our TEM analysis, where some grains with an elemental composition close to $(Cr_{0.87}Fe_{0.08}Co_{0.05})_3Ge$ were found. High-temperature XRD studies of the 300 ^oC-annealed CoFeCrGe ribbons suggests that some of these peaks started appearing when the temperature reached about 450 ^oC.

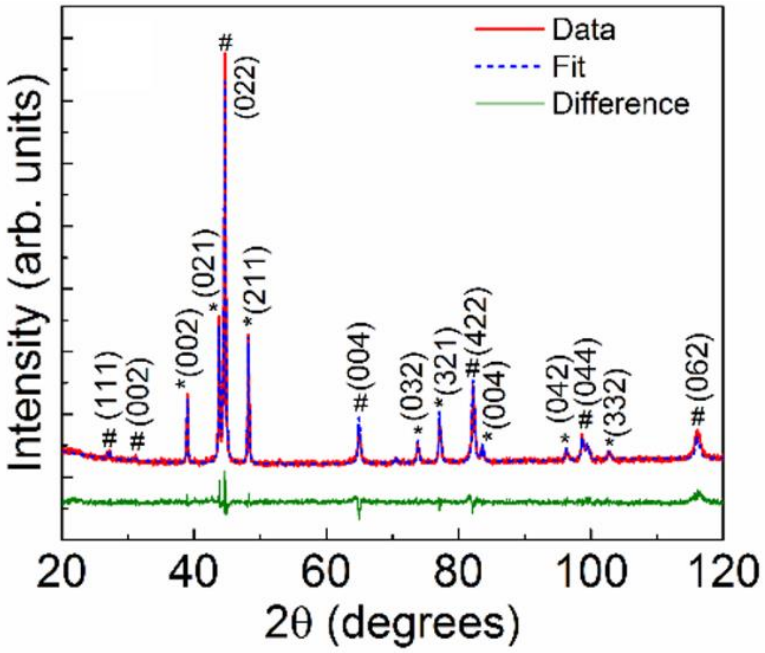

FIG. 5. 3 Room temperature powder XRD pattern of CoFeCrGe ribbons annealed at 500 ^oC for 4 hours. The # and * symbols correspond to the Co-rich (Co, Fe, Cr)$_2$FeGe and Cr-rich (Cr, Fe, Co)$_3$Ge phases, respectively.

5.4 Magnetic Properties

FIG. 5.4 shows (a) thermomagnetic curves M(T) measured at H = 1 kOe, (b) isothermal field dependence of magnetization M(H) measured at 5 K of CoFeCrSi ribbon annealed at 450 ^oC for 4 hours. As shown in FIG. 5.4 (a), the M(T) curve of CoFeCrSi is

smooth and exhibits only one magnetic transition at its Curie temperature (T_C = 790 K). The isothermal magnetization curves measured at 5 K are shown in FIG. 5.4 (b). The CoFeCrSi compound shows soft magnetic behaviors where the hysteresis loops are saturated at small magnetic fields with coercivities being smaller than 20 Oe. The saturation magnetization for single phase CoFeCrSi is 567 emu/cm^3 (2.82 μ_B/f.u.). The experimental value of M_s is close to the theoretical value of 3.0 μ_B/f. u. obtained from first-principle calculations.[25]

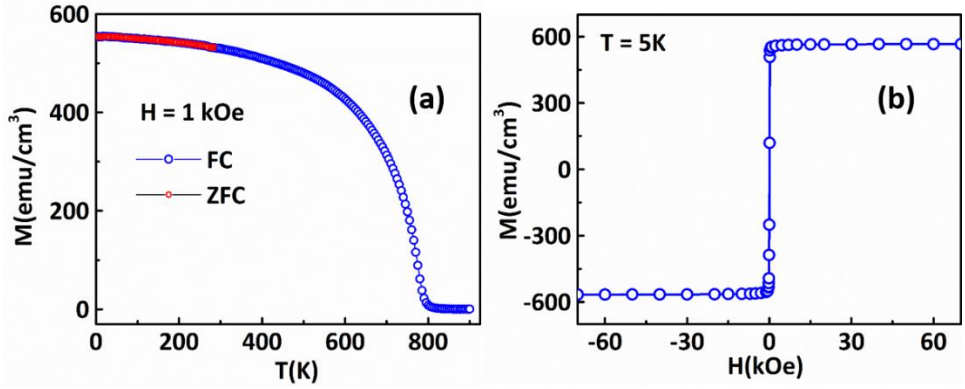

FIG. 5. 4 (a) Thermomagnetic curves M(T) measured at H = 1 kOe, (b) isothermal field dependence of magnetization M(H) measured at 5 K of CoFeCrSi ribbon annealed at 450 ^{o}C for 4 hours.

FIG. 5.5 shows: (a) thermomagnetic curves M(T) measured at H = 1 kOe, (b) isothermal field dependence of magnetization M(H) measured at 5 K of CoFeCrGe ribbons annealed at 300 ^{o}C for 4 hours, (c) enlarged isothermal M(H) loop of (b). The magnetization of the 300 ^{o}C-annealed CoFeCrGe shows two transitions in its M(T) curve: one near 675 K and the other near 870 K; the former corresponds to the temperature at which CoFeCrGe dissociates into Co-rich (Co, Fe, Cr)$_2$FeGe and Cr-rich (Cr, Fe, Co)$_3$Ge phases and the second corresponds to the Curie temperature of the Co-rich (Co, Fe,

$Cr)_2FeGe$ compound. As shown in FIG. 5.5 (a), the transition at 675 K is irreversible since the M(T) curve does not trace back on itself upon cooling the sample from 900 K to room temperature. The saturation magnetization for single phase CoFeCrGe is 535 emu/cm^3 (2.78 μ_B/f.u.).

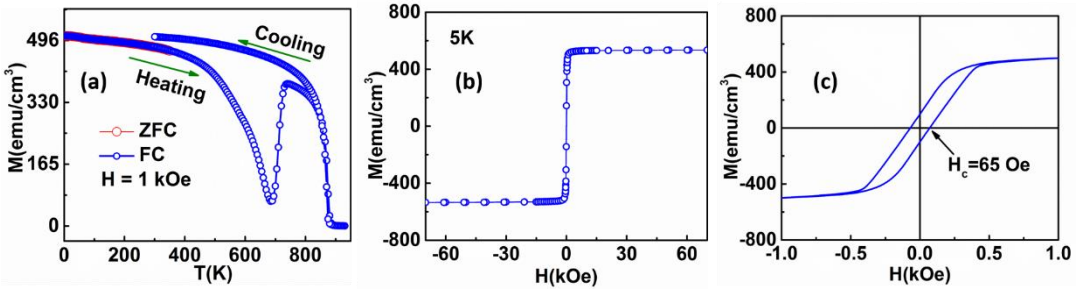

FIG. 5. 5 (a) Thermomagnetic curves M(T) measured at H = 1 kOe, (b) isothermal field dependence of magnetization M(H) measured at 5 K of CoFeCrGe ribbons annealed at 300 ^oC for 4 hours, (c) enlarged isothermal M(H) loop of (b).

FIG. 5.6 (a) Thermomagnetic curves M(T) measured at H = 1 kOe, (b) isothermal field dependence of magnetization M(H) measured at 5 K of CoFeCrGe ribbons annealed at 500 ^oC for 4 hours. (c) enlarged isothermal M(H) loop of (b). As shown in FIG. 5.6 (a), the M(T) curve is smooth with the T_C of about 790 K. Based on the XRD data, we also prepared several Co-rich $(Co, Fe, Cr)_2FeGe$ compounds and investigated the structural and magnetic properties. We found that an compound with atomic composition $(Co_{0.75}Fe_{0.125}Cr_{0.125})_2FeGe$ has a cubic crystal structure similar to that of Co-rich $(Co, Fe, Cr)_2FeGe$ phase determined by XRD with a Curie temperature of about 880 K, very close to the Curie temperature (870 K) of the 500 ^oC-annealed CoFeCrGe. This suggests that

one of the compounds formed by the dissociation of CoFeCrGe due to high-temperature (500 ^{o}C) annealing may have an elemental composition close to $(Co_{0.75}Fe_{0.125}Cr_{0.125})_2FeGe$. The contribution to the magnetization of the 500 ^{o}C-annealed sample from the Cr-rich $(Cr, Fe, Co)_3Ge$ phase is expected to be negligible as Cr_3Ge is reported to be paramagnetic.[26] Further, there is no irreversibility between the thermomagnetic curves of field-cooled (FC) and zero-field-cooled (ZFC) measurements indicating that the samples are free from disordered spin structures. The isothermal magnetization curves measured at 5 K are shown in FIG. 5.6 (b). It shows soft magnetic behaviors where the hysteresis loop is saturated at small magnetic fields with coercivities being around 130 Oe, as shown in an enlarged loop in FIG 5.6 (c). The saturation magnetization is 672 emu/cm^3.

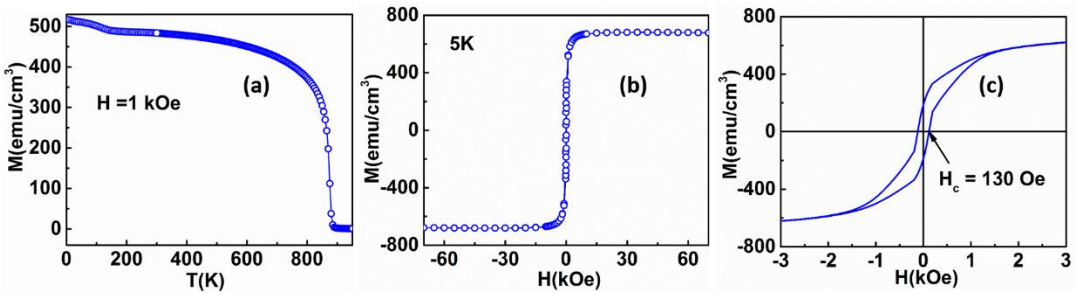

FIG. 5. 6 (a) Thermomagnetic curves M(T) measured at H = 1 kOe, (b) isothermal field dependence of magnetization M(H) measured at 5 K of CoFeCrGe ribbons annealed at 500 ^{o}C for 4 hours. (c) enlarged isothermal M(H) loop of (b).

CoFeCrSi and CoFeCrGe compounds annealed at 300 ^{o}C show soft magnetic behaviors, where the hysteresis loops are saturated at small magnetic fields with

coercivities smaller than 20 Oe. These experimental values of M_s are close to our theoretical value of 3 μ_B/f. u. obtained from the first-principle calculations.[25] The saturation magnetization of the 500 ^{o}C-annealed CoFeCrGe is larger than that of the single-phase compound. Besides, the M(H) loop in FIG. 5.6 (c) shows an increase of coercivity from 65 Oe to 130 Oe and exchange-coupling trend. The difference of the isothermal magnetic curves M(H) measured at 5K in the 300 °C-annealed and the 500 °C-annealed ribbons cannot be explained due to the secondary phase since the (Cr, Fe, Co)$_3$Ge is a cubic phase and the total content of Fe and Co is about 10 % atomic percentage, therefore the Cr-rich (Cr, Fe, Co)$_3$Ge phase is expected to be the same or less as the mixture of the $L2_1$ structure and the B2 structure. It is suggested that another magnetic intermetallic phase may exist in the 500 °C-annealed ribbons which causes the change of the magnetic hysteresis loops. The rather weak peaks in the XRD diagram of the 500 °C-annealed ribbons could be observed when the XRD diagram is enlarged, the extra peaks cannot be indexed by the mixture of $L2_1$ and B2 or the secondary Cr-rich phases. This is an additional hint that the possible existence of the unknown intermetallic phase in the 500 °C-annealed ribbons. This led to an invession of the sample of CoFeCrGe annealed at 500 °C by TEM.

5.5 TEM Study of CoFeCrGe Annealed at 500 °C.

FIG. 5.7 shows the TEM images of the primary compound in the as-spun, 300 °C-annealed and 500 °C-annealed samples, respectively. The grain size increased from about 10 nm in the as-spun samples to several hundred nm in the 300 °C-annealed samples and decreases to about 5 nm in the 500 °C-annealed samples. The experimental SAED pattern

and simulation based the B2 structure are given in FIG. 5.8 ~ 5.10 for phase identification. The different grain sizes in the as-spun and 500 °C-annealed samples also are reflected in the rings of isolated diffraction spots in FIG. 5.8 and the continuous rings in FIG. 5.10. EDS analysis confirmed that the equiatomic CoFeCrGe for all the grains in the as-spun and the 300 °C-annealed samples. However, there exist three types of grains in the 500 °C-annealed samples. The main component is very fine grains whose stoichiometry was confirmed to be $Co_{26}Fe_{26.5}Cr_{23.5}Ge_{24}$, near the equiatomic Heusler compound. The volume was estimated to be about 48% by counting statistically the grains in several TEM samples. The results on the other two components are given below.

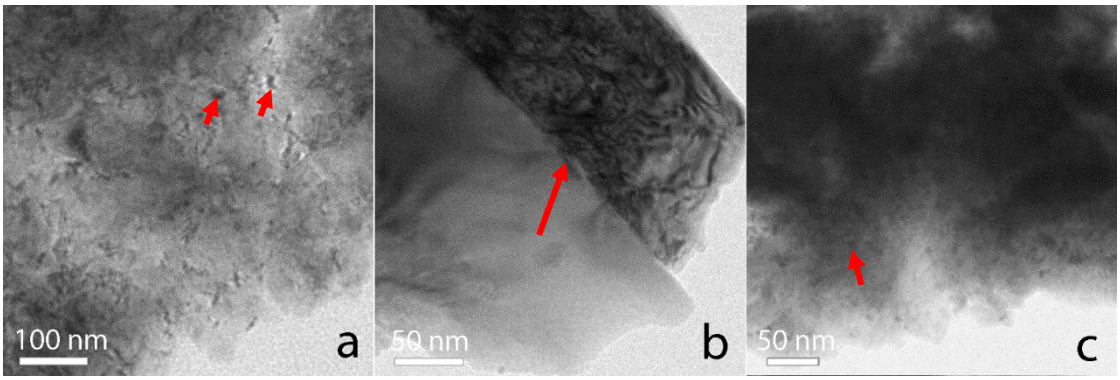

FIG. 5. 7 TEM images of (a), the as-spun, (b), 300 °C-anneal and (c), 500 °C-anneal CoFeCrGe ribbons.

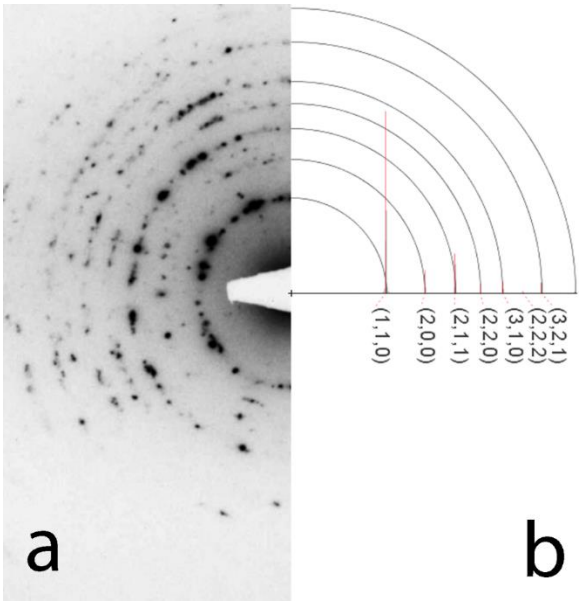

FIG. 5. 8 SAED pattern of the main phase in as-spun CoFeCrGe ribbons.

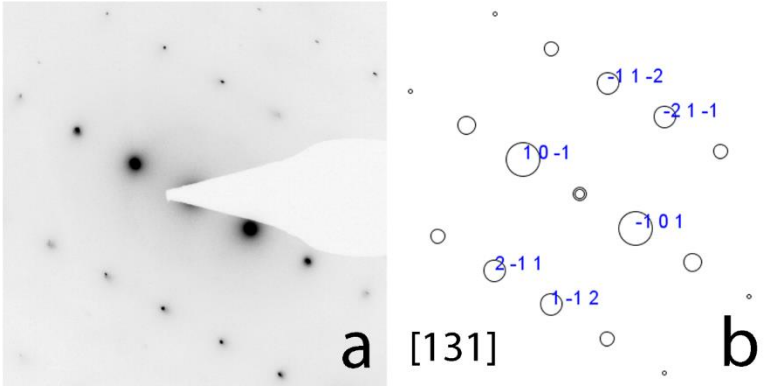

FIG. 5. 9 SAED pattern of the main phase in 300°C-annealed CoFeCrGe ribbons.

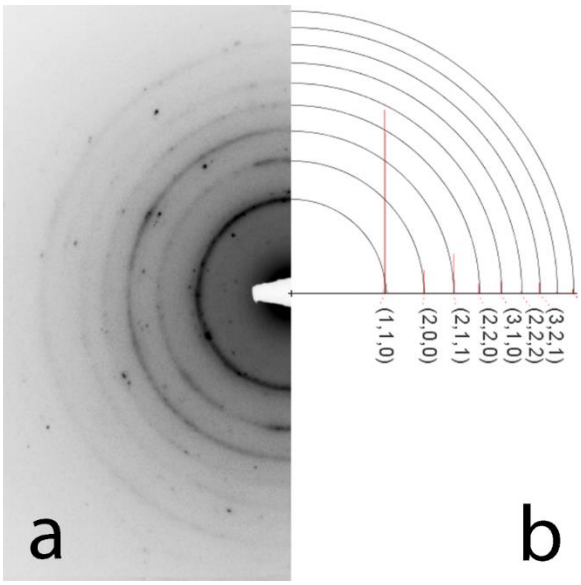

FIG. 5. 10 SAED pattern of the main phase in 500°C-annealed CoFeCrGe ribbons.

The second type of compound with grain size about serveral hundred nm up to 1~2 μm and a stoichiometry composition near $Co_{3.8}Fe_{6.4}Cr_{68.5}Ge_{21.3}$ was observed in the 500 °C-annealed samples. The volume was estimated to be about 34 % by counting statistically the grains in several TEM samples. FIG. 5.11 shows the TEM image of the Cr-rich $(Cr,Fe,Co)_3Ge$ phase; the central grain displaying darker contrast due to the grain was aligned along or near one of the main zone-axes. FIG. 5.12 shows the SAED patterns of the tetragonal phase $Co_{3.8}Fe_{6.4}Cr_{68.5}Ge_{21.3,}$ (a) [100], (b) [111] and (c) [121] zone axis. The results of the SAED analysis are in agreement with the results of the previous XRD analysis.

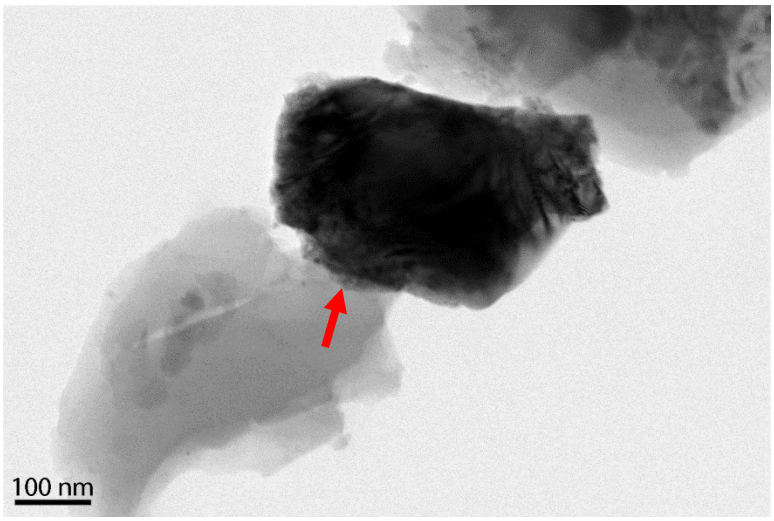

FIG. 5. 11 TEM image of the secondary phase in 500°C-annealed CoGeCrGe ribbons.

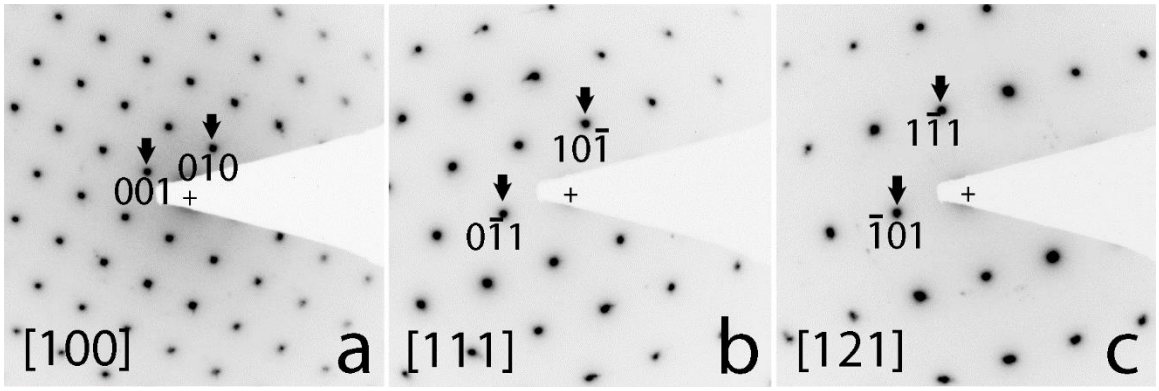

FIG. 5. 12 SAED patterns of the secondary phase in 500°C-annealed CoGeCrGe ribbons.

Although two compounds in the 500°C-annealed CoFeCrGe samples were revealed in the previous XRD analysis, a third type of compound with grain size about 2~3 hundred nm and an average composition of $Co_{53.4}Fe_{30.4}Cr_{8.6}Ge_{7.6}$ over 10 sample grains was observed together with the Cr-rich $(Cr, Fe, Co)_3Ge$ phase in the 500 °C-annealed samples. The volume was estimated to be less than 18% by counting statistically the grains in several TEM samples. The compound has been identified as a

new tetragonal phase in the present SAED study. FIG. 5.13 shows the TEM image of the new tetragonal phase in an irregular shape half embedded in the Cr-rich $(Cr,Fe,Co)_3Ge$ grain. The darker contrast due to the grain was aligned along or near one of the main zone-axes.

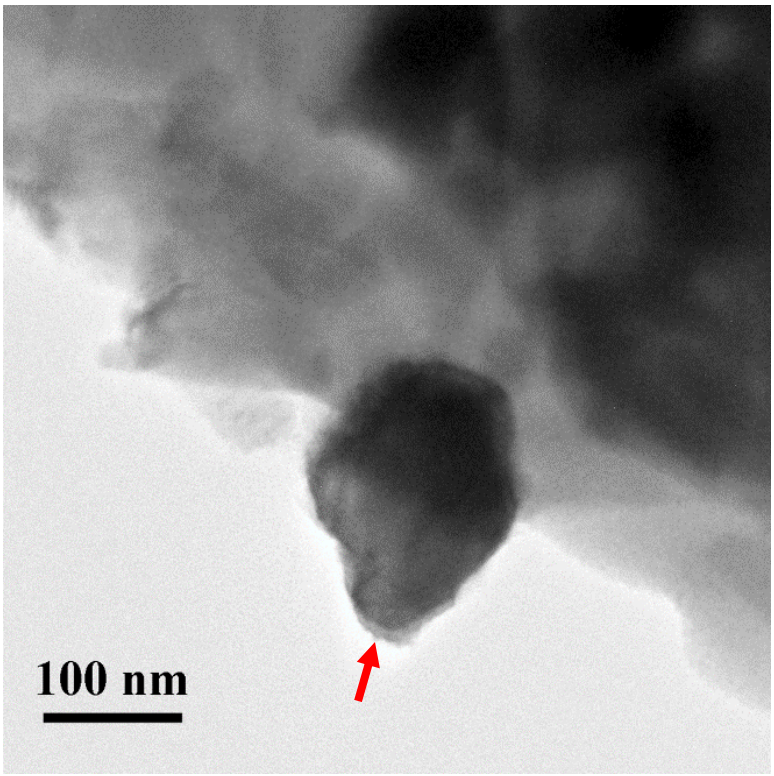

FIG. 5. 13 TEM image of the new tetragonal phase in 500°C-annealed CoGeCrGe ribbons.

FIG. 5.14 shows the SAED patterns obtained from multiple experiments and rearranged together from the [001] to the [010] zone axes with the help of the SPICA[24] software. It is noted that the patterns along the [100] and [010] axes are identical, so only the pattern along the [100] zone axis is given. The experimental tilt angles away from the [001] zone axis are listed inside each SAED patterns. The lattice type and parameter were determined by means of the reciprocal lattice reconstruction from a series of tilt SAED

patterns, as shown in FIG. 5.15 (a), which is a snapshot of the UCRD software.[23] The SAED patterns in FIG. 5.14 (a ~ e) share a common axis, the reflections perpendicular the common axis in each SAED patterns were used to build the reciprocal lattice. A tetragonal lattice with a = 0.76 nm, c = 0.284 nm was obtained. The calculated tilt angles are listed near the experimental data and the zone axes for each SAED pattern are labeled in FIG. 5.14. FIG. 5.15 (b) shows the distribution of the corresponding zone axes in a stereogram.

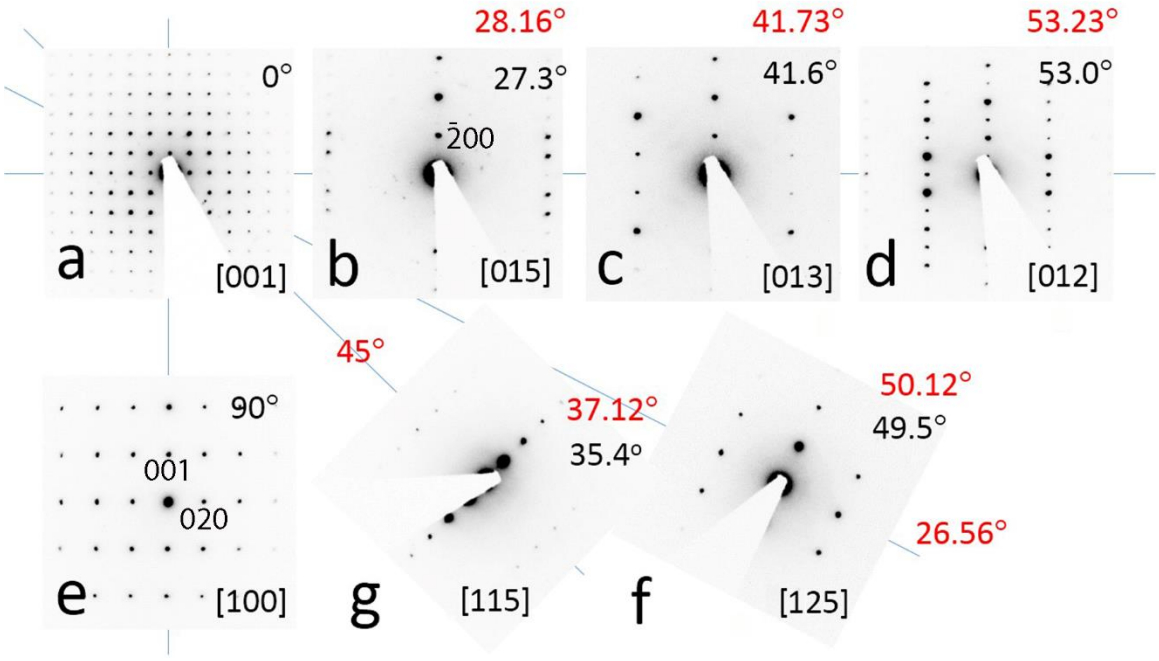

FIG. 5. 14 SAED patterns of the new tetragonal phase in 500°C-annealed CoGeCrGe ribbons.

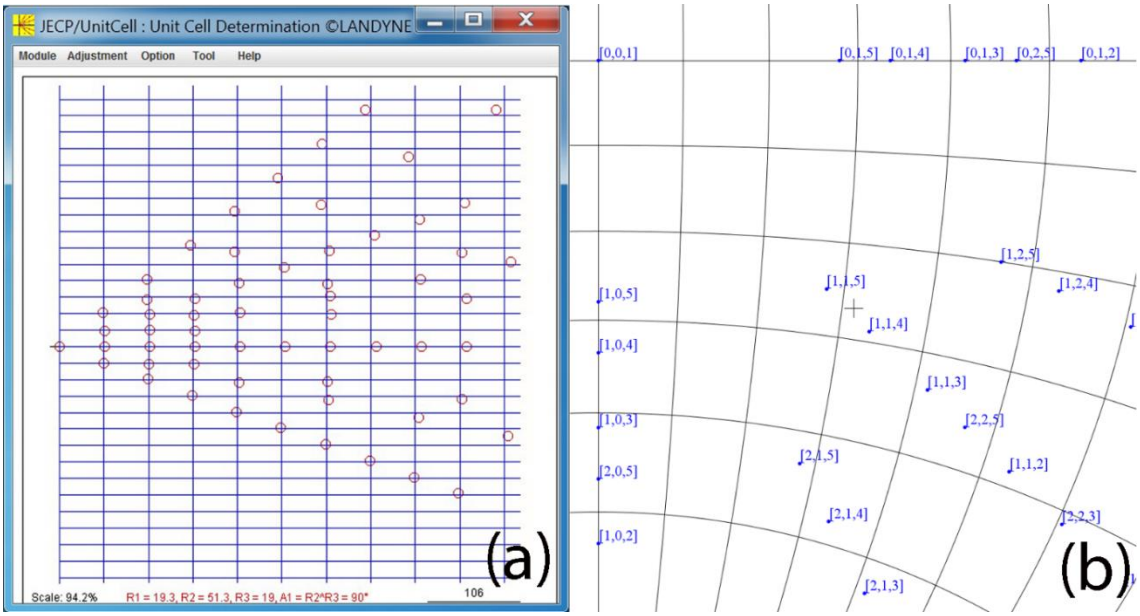

FIG. 5. 15 Lattice reconstruction of the new tetragonal phase in 500°C-annealed CoGeCrGe ribbons.

It is clear that the extinction happens for the reflections of (h00) and (0k0) when h, k is odd. The extinct reflection may appear, e.g. in [001] SAED pattern, due to strong dynamic multiple scattering. FIG. 5.16 shows the SAED pattern of the [001] zone axis in the relatively thin area and processed pattern. The space group is $P42_12$ (90) according to the lattice type and the extinction rule. FIG. 5.17 shows an HREM image of the new tetragonal phase along the [001] zone axis. A unit cell is marked as the square in the HREM image. The features of the image can be described as circles at each of the square corners. However, the sample was so thick that the circles only appear along the edge of the grain.

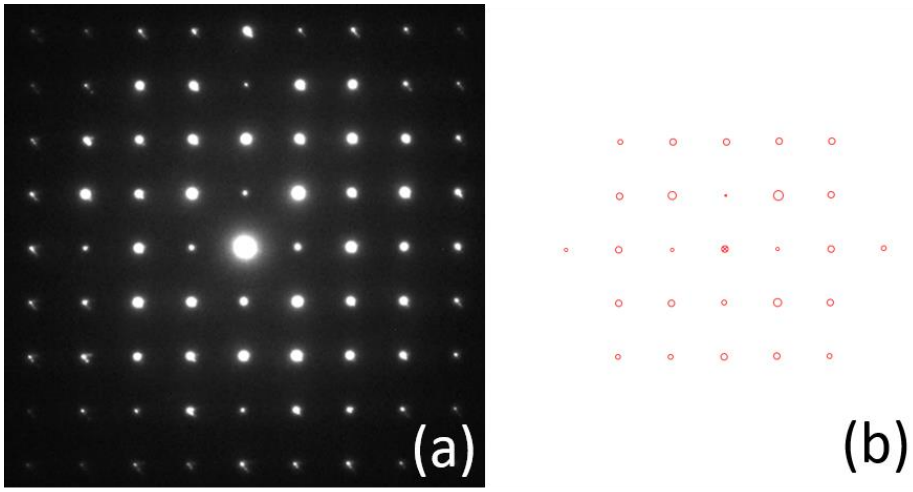

FIG. 5. 16 SAED pattern of the new tetragonal phase along [001] zone axis and the processed intensity.

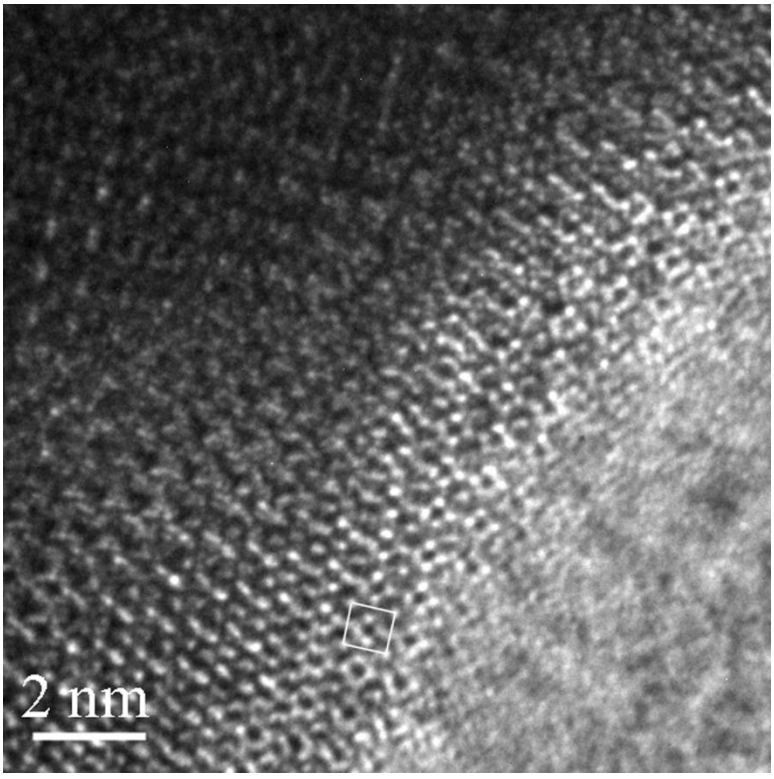

FIG. 5. 17 HREM of the new tetragonal phase along [001] zone axis.

The new tetragonal phase is always embeded in the matrix of the Cr-rich cubic phase. The grains of the tetragonal phase were observed mostly in irregular shapes as shown in FIG. 5.13, but a grain in a nearly rectangular shape was also observed. FIG. 5.18 shows (a) the TEM image of the new tetragonal phase and (b) a schematic drawing for the interpretation of the facets of the grain. The darker contrast due to the grain was aligned along or near one of the main zone-axes.

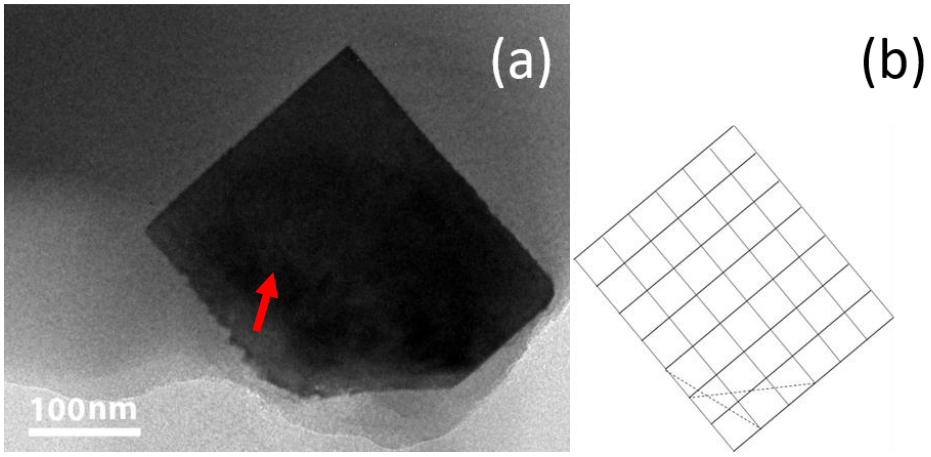

FIG. 5. 18 (a) the TEM image of the new tetragonal phase and (b) a schematic drawing for the interpretation of the facets of the grain.

The lattice parameters of the two phases do not allow a perfect lattice matching in any form, which indicates that there may be no fixed orientation relationship between them. SAED experiment confirms this idea. FIG. 5.19 shows (a) a SAED pattern along the [110] axis from the new tetragonal phase and (b) an SAED pattern along the [001] zone axis from the adjacent matrix of the Cr-rich cubic phase. There is a tilt angle of 6.8° between the two SAED patterns along their nearest main zone axes.

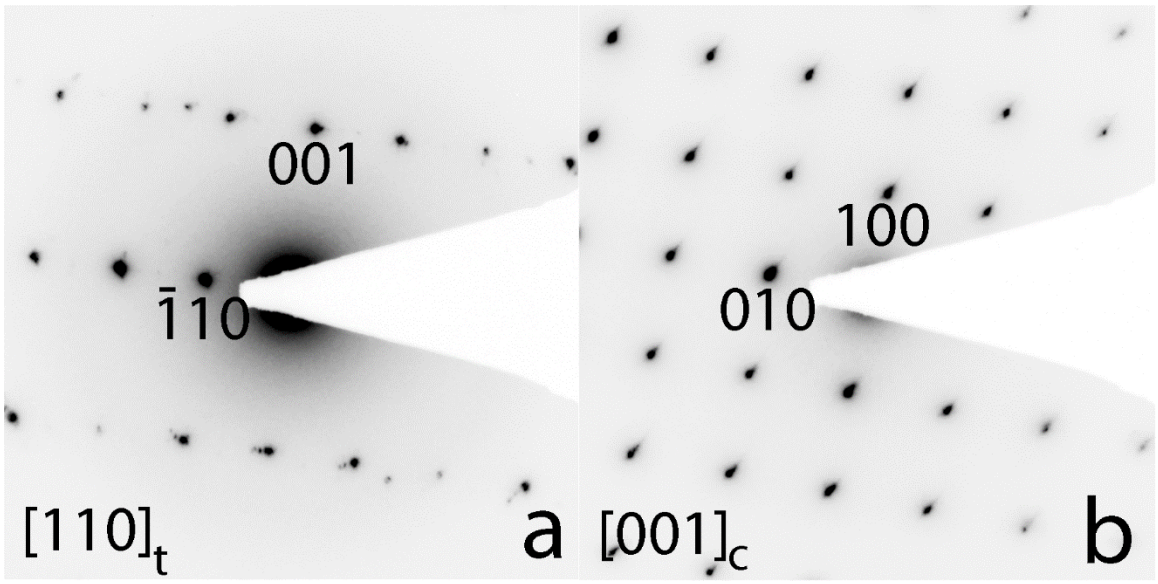

FIG. 5. 19 The orientation relationship of the new tetragonal phase and the Cr-rich cubic phase in SAED patterns, (a) along the [110] zone axis of the new tetragonal phase, (b) along the [100] zone axis of the Cr-rich cubic phase. Tilting angle from (0,0) to (0.83, 6.60), i.e. 6.8 degree.

5.6 Summary

In summary, an experimental investigation of the structural and magnetic properties of CoFeCrSi and CoFeCrGe Heusler compounds has been carried out. The experimental results showed that both CoFeCrSi and CoFeCrGe compounds crystallize in cubic $L2_1$ structures with a small site disorder. Although the first-principle calculation predicted a possibility of tetragonal phase transition in CoFeCrGe, the tetragonal phase could not be stabilized experimentally. Instead, the cubic CoFeCrGe disintegrated into other phases near 402 ^{o}C (675 K). Both CoFeCrSi and CoFeCrGe compounds showed ferrimagnetic spin order with saturation magnetizations of 2.82 μ_B/f.u. and 2.78 μ_B/f.u., respectively, which are close to the theoretically predicted values of 3 μ_B/f.u. for their half-metallic phases. The

CoFeCrSi compound exhibited very high Curie temperature (T_C = 790 K) but the T_C of CoFeCrGe could not be measured due to its dissociation into other compounds. The predicted large band gaps and Curie temperatures much above room temperature make these materials promising for room-temperature spintronic and magnetic applications. These results are expected to stimulate further research on the thin films of these materials. A TEM study of the CoFeCrGe compound annealed at 500 °C shows it is composed of three alloys with average compositions of $Co_{26}Fe_{26.5}Cr_{23.5}Ge_{24}$, $Co_{3.8}Fe_{6.4}Cr_{68.5}Ge_{21.3}$ and $Co_{53.4}Fe_{30.4}Cr_{8.6}Ge_{7.6}$, listed in a sequence of volume percentage from major to minor. The primary alloy is composed of a mixture the $L2_1$ type structure with a = 0.571 nm and the B2 type structure with a = 0.286 nm. The secondary alloy has a cubic structure with a = 0.46127 nm in a prototype of Cr_3Ge. The tertiary one is a new tetragonal structure with lattice parameters a = 0.76 nm, c = 0.284 nm, which were determined using tilt-series electron diffraction technique in this work. The tertiary (Co,Fe)-rich phase was found to embedded in the matrix of the secondary Cr-rich phase, but there is no special orientation between the two phases. The difference in the magnetic hysteresis loops of the samples annealed at 300 °C and 500 °C may be interpreted as the appearance of the new tetragonal crystalline phase.

5.7 Bibliography

1. R. A. de Groot, F. M. Mueller, P. G. v. Engen and K. H. J. Buschow, "New class of materials: Half-metallic ferromagnets", Physical Review Letters **50**, 2024-2027 (1983).

2. M. Jean-Baptiste, "From epitaxial growth of ferrite thin films to spin-polarized tunnelling", Journal of Physics D: Applied Physics **46**, 143001 (2013).

3. M. I. Katsnelson, V. Y. Irkhin, L. Chioncel, A. I. Lichtenstein and R. A. de Groot, "Half-metallic ferromagnets: From band structure to many-body effects", Reviews of Modern Physics **80**, 315-378 (2008).

4. R. J. Soulen, J. M. Byers, M. S. Osofsky, B. Nadgorny, T. Ambrose, S. F. Cheng, P. R. Broussard, C. T. Tanaka, J. Nowak, J. S. Moodera, A. Barry and J. M. D. Coey, "Measuring the spin polarization of a metal with a superconducting point contact", Science **282**, 85-88 (1998).

5. X. Li, X. Wu, Z. Li and J. Yang, "Proposal of a general scheme to obtain room-temperature spin polarization in asymmetric antiferromagnetic semiconductors", Physical Review B **92**, 125202 (2015).

6. A. Nelson, Y. Huh, P. Kharel, V. R. Shah, R. Skomski and D. J. Sellmyer, "Structural, magnetic, and electron transport properties of $Mn_{3-x}Pt_xSn$ (x = 0, 0.5, 1) nanomaterials", Journal of Applied Physics **115**, 17A923 (2014).

7. P. Lukashev, P. Kharel, S. Gilbert, B. Staten, N. Hurley, R. Fuglsby, Y. Huh, S. Valloppilly, W. Zhang, K. Yang, R. Skomski and D. J. Sellmyer, "Investigation of spin-gapless semiconductivity and half-metallicity in Ti_2MnAl-based compounds", Applied Physics Letters **108**, 141901 (2016).

8. H. Atsufumi and T. Koki, "Future perspectives for spintronic devices", Journal of Physics D: Applied Physics **47**, 193001 (2014).

9. G. Y. Gao, L. Hu, K. L. Yao, B. Luo and N. Liu, "Large half-metallic gaps in the quaternary Heusler compounds CoFeCrZ (Z = Al, Si, Ga, Ge): A first-principles study", Journal of Compounds and Compounds **551**, 539-543 (2013).

10. M. Jourdan, J. Minár, J. Braun, A. Kronenberg, S. Chadov, B. Balke, A. Gloskovskii, M. Kolbe, H. J. Elmers, G. Schönhense, H. Ebert, C. Felser and M. Kläui, "Direct observation of half-metallicity in the Heusler compound Co_2MnSi", Nature Communications **5**, (2014).

11. C. Felser and B. Hillebrands, "New materials with high spin polarization: half-metallic Heusler compounds", Journal of Physics D-Applied Physics **40**, 3 (2007).

12. H. Kurt, K. Rode, M. Venkatesan, P. Stamenov and J. M. D. Coey, "High spin polarization in epitaxial films of ferrimagnetic Mn_3Ga", Physical Review B **83**, 020405 (2011).

13. Y. Miura, M. Shirai and K. Nagao, "Ab initio study on stability of half-metallic Co-based full-Heusler compounds", Journal of Applied Physics **99**, 08J112 (2006).

14. Y. Huh, P. Kharel, V. R. Shah, E. Krage, R. Skomski, J. E. Shield and D. J. Sellmyer, "Magnetic and Structural Properties of Rapidly Quenched Tetragonal $Mn_{3-x}Ga$ Nanostructures", IEEE Transactions on Magnetics **49**, 3277-3280 (2013).

15. C. Felser, G. H. Fecher and B. Balke, "Spintronik: eine Herausforderung für Materialwissenschaften und Festkörperchemie", Angewandte Chemie **119**, 680-713 (2007).

16. P. Kharel, W. Zhang, R. Skomski, S. Valloppilly, Y. Huh, R. Fuglsby, S. Gilbert and D. J. Sellmyer, "Magnetism, electron transport and effect of disorder in CoFeCrAl", Journal of Physics D: Applied Physics **48**, 245002 (2015).

17. S. Ouardi, G. H. Fecher, C. Felser and J. Kübler, "Realization of spin-gapless semiconductors: The heusler compound Mn_2CoAl", Physical Review Letters **110**, 100401 (2013).

18. M. Franz, "Topological insulators: Starting a new family", Nat Mater **9**, 536-537 (2010).

19. P. Kharel, Y. Huh, N. Al-Aqtash, V. R. Shah, R. F. Sabirianov, R. Skomski and D. J. Sellmyer, "Structural and magnetic transitions in cubic Mn_3Ga", Journal of Physics: Condensed Matter **26**, 126001 (2014).

20. Z. Gercsi and K. Hono, "Ab initio predictions for the effect of disorder and quarternary compounding on the half-metallic properties of selected Co_2Fe-based Heusler compounds", Journal of Physics: Condensed Matter **19**, 326216 (2007).

21. T. Graf, C. Felser and S. S. P. Parkin, "Simple rules for the understanding of Heusler compounds", Progress in Solid State Chemistry **39**, 1-50 (2011).

22. K. Özdoğan, E. Şaşıoğlu and I. Galanakis, "Slater-Pauling behavior in LiMgPdSn-type multifunctional quaternary Heusler materials: Half-metallicity, spin-gapless and magnetic semiconductors", Journal of Applied Physics **113**, 193903 (2013).

23. X. Li, "SPICA: stereographic projection for interactive crystallographic analysis", Journal of Applied Crystallography **49**, 1818-1826 (2016).

24. X. Li, "TEM Study of the Cobalt-Rich Hf-Co Intermetallic Compounds", Microscopy and Microanalysis **22**, 1700-1701 (2016).

25. Y. Jin, P. Kharel, P. Lukashev, S. Valloppilly, B. Staten, J. Herran, I. Tutic, M. Mitrakumar, B. Bhusal, apos, A. Connell, K. Yang, Y. Huh, R. Skomski and D. J. Sellmyer, "Magnetism and electronic structure of CoFeCrX (X = Si, Ge) Heusler compounds", Journal of Applied Physics **120**, 053903 (2016).

26. T. Sato, A. Jono, E. Ohta and M. Sakata, "Electrical resistivity and magnetic susceptibility in the amorphous Cr_xGe_{1-x} compound system", Physical Review B **38**, 11741-11750 (1988).

Table of Contents

Chapter 6. Summary and Outlook

6.1 Summary

This thesis is devoted to experimental studies of the structural and magnetic properties, spin polarization, magnetoresistance and anomalous Hall-effect of calculated spin-gapless semiconductor CoFeCrAl, half-metallic CoFeCrX (X = Si, Ge) and inverse tetragonal Mn_2PtSn. These Heusler compounds present an interesting class of ferromagnetic materials for spintronic applications since they are predicted to be spin-gapless semiconductors and half-metallic properties with 100 % spin polarization at Fermi level. In this thesis, the basic physical principles, the magnetoresistance, and Hall-effect phenomena and the fabrication and characterization techniques utilized were presented. The structural, magnetic properties, spin polarization and electron transport properties of the fabricated elements were studied.

Chapter 3 presents how the structural disorder affects the magnetic and transport behavior of CoFeCrAl thin films deposited on MgO. CoFeCrAl thin films deposited on MgO exhibit nearly perfect epitaxy and a high degree of $L2_1$ Heusler order. All considered types of chemical disorder destroy the spin-gapless semiconductivity of Y-ordered CoFeCrAl, but B2 disorder and A2-type Cr-Fe disorder conserve the half-metallicity of the compound. CoFeCrAl films onto MgO and Si with exhibiting different degrees of structural order: the MgO substrate yields well-ordered epitaxial films, whereas the films deposited on Si are highly disordered and polycrystalline. The resistivity was measured as a function of temperature and the residual resistivity was analyzed as a function of the disorder. The films on Si have the higher residual resistivity, which indicates dirty-metal behavior, whereas the behavior of the films on MgO is

consistent with both dirty-metal and spin-gapless semiconducting behavior. The spin polarization at the Fermi level is higher than 68% and probably exceeds 90%. It is encouraging for spin electronics applications, due to the robustness of the half-metallicity with respect to most types of chemical disorder and because the disorder enhances the resistivity without much reduction in Curie temperature.

In Chapter 4, the structural, magnetic and electron transport properties of epitaxial thin films of an inverse tetragonal Mn_2PtSn Heusler compound have been investigated. Structural analysis shows the structure of epitaxial Mn_2PtSn film is inverse tetragonal with lattice constants a = 0.4488 nm, and b = 0.6148 nm (space group I-4m2, No 119). Lattice constants have a very small mismatch with MgO, which makes it promising for coherent electron-tunneling phenomena. Measured saturation magnetization is 3.2 μ_B/f.u., less than that of calculated from the density of states. The magnetization measurements revealed an in-plane anisotropy energy of 10 Merg/cm^3. The magnetoresistance ratio is 1.0 % with a magnetic field applied out of the plane. Transport measurement confirmed the metallic transport behavior and side-jump mechanism is dominant in carrier scattering. Due to the high spin polarization, such half-metallic magnetic films with the advantages of strong in-plane magnetocrystalline anisotropy and proper thickness could be used in spin valves or magnetic tunnel junctions as high-performance magnetic memory elements.

Experimental investigation of the structural and magnetic properties of CoFeCrSi and CoFeCrGe Heusler compounds have been presented in Chapter 5. The experimental results showed that both CoFeCrSi and CoFeCrGe compounds crystallize in cubic $L2_1$ structures with a small site disorder. Cubic CoFeCrGe disintegrated into additional

phases near 402 ºC (675 K). Both CoFeCrSi and CoFeCrGe compounds showed ferrimagnetic spin order with saturation magnetizations of 2.82 μ_B/f.u. and 2.78 μ_B/f.u., respectively, which are close to the theoretically predicted values of 3 μ_B/f.u. for their half-metallic phases. The CoFeCrSi compound exhibited very high Curie temperature (T_C = 790 K) but the T_C of CoFeCrGe could not be measured due to its dissociation into other compounds. The predicted large band gaps and Curie temperatures much above room temperature make these materials promising for room-temperature spintronic and magnetic applications. These results are expected to stimulate further research on the thin films of these materials. Secondly, a study of the CoFeCrGe compound annealed at 500 °C shows it is composed of three alloys with average compositions of $Co_{26}Fe_{26.5}Cr_{23.5}Ge_{24}$, $Co_{3.8}Fe_{6.4}Cr_{68.5}Ge_{21.3}$, and $Co_{53.4}Fe_{30.4}Cr_{8.6}Ge_{7.6}$, listed in a sequence of volume percentage from major to minor. The primary compound is composed of a mixture the $L2_1$ type structure with a = 0.571 nm and the B2 type structure with a = 0.286 nm. The secondary compound has a cubic structure with a = 0.46127 nm in a prototype of Cr_3Ge. The tertiary one is a new tetragonal structure with lattice parameters a = 0.76 nm, c = 0.284 nm, which were determined using tilt-series electron diffraction technique in this work. The tertiary (Co, Fe)-rich phase was found to embedded in the matrix of the secondary Cr-rich phase, but there is no special orientation between the two phases. The difference in the magnetic hysteresis loops of the samples annealed at 300 °C and 500 °C may be interpreted as the appearance of the new tetragonal crystalline phase.

6.2 Outlook

In general, the Heusler compounds investigated in this thesis are very promising for spin-electronics applications, due to the half-metallicity with above room temperature Curie temperature. CoFeCrAl is calculated to be spin-gapless semiconductor based on perfect ordered $L2_1$ structure with promising properties combined the half-metallicity and gapless semiconducting performances. Thin films deposited on MgO exhibit nearly perfect epitaxy and a high degree of $L2_1$ Heusler order, which gives a direction to synthesize the perfect ordered $L2_1$ structure of CoFeCrAl via tuning the fabrication parameters or utilizing a different substrate with lattice constant matching with CoFeCrAl. All considered types of chemical disorder destroy the spin-gapless semiconductivity of Y-ordered CoFeCrAl, but B2 disorder and A2-type Cr-Fe disorder conserve the half-metallicity of the compound. This indicates that spintronic devices of CoFeCrAl will have stable half-metallic properties due to the robustness of the half-metallicity with respect to most types of chemical disorder and because the disorder enhances the resistivity without much reduction in Curie temperature. Further experiments are needed to apply CoFeCrAl into MTJs or spin filters.

Inverse tetragonal Mn_2PtSn shows a high in-plane anisotropy energy and high Curie temperature, which can be used in spin valves or magnetic tunnel junctions as high-performance magnetic memory elements. For spintronic devices which need out of plane anisotropy, a suitable and different substrate is needed to stimulate the perpendicular growth of Mn_2PtSn according to its lattice constant.

The new (Co,Fe)-rich tetragonal phase $Co_{53.4}Fe_{30.4}Cr_{8.6}Ge_{7.6}$ with lattice parameters a = 0.76 nm, c = 0.284 nm was found to embedded in the matrix of the secondary Cr-rich phase if CoFeCrGe compound annealed at 500 °C. The coexistence of cubic and tetragonal Co-Fe-Cr-Ge phases indicates that the synthesis parameters including the heat treatment parameters need to be tuned to inhibit the cubic phase and promote the tetragonal phase. The present samples do not exhibit hard magnetic properties due to the amount of the new tetragonal phase is small. Element doping may also be a direction to develop the single tetragonal phase or increase the amount of this phase. If a single phase of tetragonal $Co_{53.4}Fe_{30.4}Cr_{8.6}Ge_{7.6}$ could be developed, it may improve the next generation rare-earth-free permanent magnets.